Creation of ultracold RbCs molecules

KOPPINGER, MICHAEL,PETER

Creation of ultracold RbCs molecules

Michael Peter Köppinger

Abstract

This thesis reports the investigation of the scattering properties of a mixture of Rb and Cs and the formation of ultracold Feshbach molecules. The production of Feshbach molecules is a crucial step towards the production of ultracold polar molecules, which is of significant interest for a wide range of potential applications.

We have investigated the scattering properties of a mixture of ^{85}Rb and ^{133}Cs in their lowest spin channel in a magnetic field range from 0 to 700 G. Furthermore, we explored the Feshbach spectrum of ^{85}Rb alone in both, the $(f = 2, m_f = -2)$ and $(2, +2)$ states up to a magnetic field of 1000 G. Additionally a Feshbach resonance in a $(2, +2) + (3, +3)$ spin mixture was experimentally confirmed.

We associated Cs_2 Feshbach molecules using a Feshbach resonance at 19.9 G. $2.1(1) \times 10^4$ molecules with a temperature of ~ 60 nK were produced from a sample of $3.28(2) \times 10^5$ Cs atoms with a PSD of 0.20(1). Due to a magnetic field gradient, the molecules 'bounce' at an avoided crossing between two states at 13.5 G. This gradient field was also used to produce multiple molecular clouds from one atomic sample. A combination of both techniques led to a 'collision' between two Cs_2 clouds.

Furthermore, we associated up to $\sim$ 5000 heteronuclear ^{87}RbCs Feshbach molecules using an interspecies resonance at 197.1 G. Confined in the dipole trap the molecules have a lifetime of 0.21(1) s. We have measured the magnetic moment of the molecules in different internal states in a magnetic field range from 181 to 185 G.

Molecular loss spectroscopy on electronically excited states was performed to identify candidates for the intermediate state of a STIRAP transfer of the molecules into their rovibrational ground state. Subsequently, the binding energy of the rovibrational ground state was measured to be 3811.574(1) cm^{-1}, using two-photon spectroscopy.

Creation of ultracold RbCs molecules

Michael Peter Köppinger

A thesis submitted in partial fulfilment
of the requirements for the degree of
Doctor of Philosophy

Department of Physics
Durham University

June 20, 2014

Contents

List of Figures

List of Tables

Declaration

I confirm that no part of the material offered has previously been submitted by myself for a degree in this or any other University. Where material has been generated through joint work, the work of others has been indicated.

Michael Peter Köppinger
Durham, June 20, 2014

Acknowledgements

The last four years were an exciting and instructive time for me. I have seen so many new places and met so many people, that I first have to apologise to those I have forgotten in this list. A PhD in this field is definitely not a one-persons job and I am really grateful to everyone who contributed to this work and helped me during my time in Durham. I would like to thank

- My supervisor Simon Cornish, who gave me the opportunity to work on this exciting experiment. His guidance as well as his dedication towards physics and his knowledge in this particular field of research were essential for the successful completion of this work. I very much appreciated the discussions and the open door to his office whenever a problem needed to be discussed. Beside the four years of physics I enjoyed the Cornish-group trips to various places very much.

- Ifan Hughes, my co-supervisor, for his support and advice in all aspects of my life as a PhD student. Ifan always shared his enthusiasm of physics and was always up for a lough inside and outside the walls of the university. The deeply philosophical pub discussions will be missed.

- My examiners, Lucia Hackermüller and Charles Adams, who made it possible to realise my tight schedule and gave me the chance to present what I have learned (and what not), working with ultracold atoms in the last five years.

- The fellow co-workers on the RbCs experiment: HungWen Cho, Danny McCarron and Dan Jenkin, who took on a lot of the painful work, so that the experiment was in this great condition when I joined the group. They taught me to run the machine and the Simon Cornish way of doing things. I am sure the experiment is in good hands now, with Peter Molony, Phil Gregory and the postdocs Bo Lu and Zhonghua Ji pushing the experiment to new limits.

- A close collaboration with theorists is indispensable for the work presented in this thesis. Jeremy Hutson and his group were always there to help and tried to explain their work such that even an experimentalist was able to understand it (although it didn't always work). Here

special thanks goes to Caroline Blackley and Ruth Le Sueur, who calculated the scattering lengths and binding energies presented in this thesis.

- The rest of the Cornish division, working on the soliton experiment, Sylvi Händel, Anna Marchant, Tim Wiles, Manfred Yu, Ana Rakonjac and Steve Hopkins, who is now a member of the YbCs experiment with Kirsteen Butler, Stefan Kemp and Ruben Freytag. I had a great time working with all of you and hope you will carry on with the same team spirit that you always showed towards me.

- The entire AtMol group, which is learned to know as a fantastic group of motivated people and a team of enthusiastic supervisors.

- The Friday pub group for pulling me out of the lab in the end of the week.

- The people in the mechanical and electronic workshop and the finance office who always provide the best possible working circumstances.

- All the AtMol members who were also my housemates over the last four years, HungWen Cho, Anna Marchant, Liz Bridge and especially Ulrich Krohn, who also did a lot of proof reading and helped me a lot over the last four years.

- Special thanks go to my family, my parents, plus partners, who always give me the feeling that I can do and reach whatever I want to. They never tried to push me into any direction. This way it was possible to grow from a little boy, who liked to look at the pictures in Carl Sagan's book 'Cosmos', to an old boy, who still likes to look at the same pictures. And my two brothers, who are always there for me and are very successful in showing me that physics is not everything in life (other than Lego, sports...).

- Last but not least: Thank you Judith.

Chapter 1

Introduction

1.1 Cold atoms and molecules

The field of atomic physics changed fundamentally with the invention of the laser 50 years ago [1, 2]. The highly monochromatic light made possible much more precise spectroscopy of atoms and molecules. Subsequently the ability was developed to cool and trap atoms in the microkelvin regime using lasers, giving vastly increased control of quantum systems [3–9]. This led to the award of the 1997 Nobel Prize in Physics to S. Chu, C. Cohen-Tannoudji and W. D. Phillips [10–12].

Even lower temperatures are achievable through subsequent evaporative cooling [13], which can lead to the formation of a Bose-Einstein Condensate (BEC), first observed in 1995 [14–17]. The Nobel Prize in Physics 2001 was awarded to E. A. Cornell, W. Ketterle and C. E. Wieman [18, 19] for the realisation of atomic samples in this state of matter, where a macroscopic ensemble of bosons occupy the same quantum state at finite temperature. The existence of this phase transition from a thermal gas to BEC was predicted by S. N. Bose and A. Einstein [20, 21] in the 1920s. More recently it was possible to load ultracold atoms into an optical lattice potential [22, 23]. Here, a previously unknown level of control of the internal state of the atoms and decoupling from external influences is achieved.

All these advancements led to the question of whether it is possible to produce an ultracold sample of molecules. Specifically, the realisation of a sample of

polar molecules in an optical lattice potential would open the door to many experiments, including quantum simulation of condensed matter systems [24–27], quantum computation [28, 29], precision measurement [30–32] and controlled chemistry [33, 34]. Polar molecules possess a permanent electric dipole moment similar to Rydberg atoms [35] and hence exhibit an anisotropic, long range dipole-dipole interaction, compared to isotropic, short-range contact interactions in ultracold atomic samples [36].

Unfortunately, an easy adaption of the cooling techniques used for atoms is not possible for molecules. Laser cooling is only applicable to a small fraction of atomic species where a (nearly) closed transition between two states exists. Molecules generally have a much more complex level structure than atoms, including rotational and vibrational levels. Therefore, it is very difficult to find good transitions for cooling. Although laser cooling of certain molecules has become possible by selecting transitions with favourable Franck-Condon factors, where only a small number of states are populated after many scattering processes, and large progress has been made in this field over the last few years [37–39], this technique is still very complex and not well investigated yet.

Generally, there are two different ways to produce a cold sample of molecules [40]:

- *Direct cooling of molecules:* A sample of stable molecules is produced at a high temperature and subsequently cooled to low temperatures.
- *Association of ultracold atoms:* A sample of atoms is cooled to ultralow temperature before association techniques are applied to form molecules.

Direct cooling of molecules When the molecules are cooled directly, often a combination of different techniques for the production of a molecular beam, slowing and cooling is used. The starting point is usually a supersonic beam source or a buffer gas cooled molecular sample, where molecules are cooled by collisions with a cryogenic helium buffer gas [41–43]. Molecules from a buffer gas cooled source can be loaded directly into a static magnetic

trap [44] and sympathetically cooled [45]. Sisyphus cooling, a technique well known for atoms, has also been applied to electrically trapped molecules [46].

Many techniques have been developed to decelerate a beam of molecules to a velocity where they can be loaded into a trap. Changing electric [47–49] or magnetic [50–53] fields or a varying optical potential [54] can be used to remove kinetic energy from the molecules. Other experiments bring molecules to rest by changing the inertial system [55, 56] or using the energy released during a chemical reaction [57].

Although the techniques have the advantage of being generally applicable, the temperatures reached with these techniques are in a range between a few mK and several K. This leads to low phase-space density (PSD) samples and thus the molecules are not suitable to investigate ultracold quantum gases. Therefore, other techniques have to be used to produce a molecular sample with a temperature below one μK and a PSD close to unity.

Association of ultracold atoms In the second approach, atoms are cooled to ultralow temperatures using well-developed laser and evaporative cooling techniques. Subsequently, molecules are either formed via photoassociation [58] or magnetoassociation [59].

During the *photoassociation* process, two colliding atoms absorb a photon and form an electronically excited molecule. Due to the Franck-Condon principle, the photoassociation takes place at relatively large internuclear separations and generally, the excited molecules decay into two free atoms [60]. To increase the probability for decaying into stable ground state molecules, excited states with good Franck-Condon factors for transitions to the ground state at small internuclear separations have to be used. A sample of Cs_2 in a high vibrational excited level was formed this way in 1998 [61].

This technique was also used to produce a sample of cold ^{85}RbCs molecules [62, 63]. In these experiments, a relatively large fraction (7%) of the photoassociated molecules decayed into one long-lived level ($a^3\Sigma^+$, $\nu = 37$). These molecules were then transferred into the vibrational ground state using a laser-stimulated state transfer process. However, the molecules were in different rotational states, the temperature was $\sim$100 mK and the sample had a low PSD.

A single photoassociation step was sufficient to produce LiCs in the absolute rovibrational ground state [64], where the transition probability from the chosen vibrational level of the electronically excited state to the absolute ground state is large.

In another experiment, photoassociation was applied to ^{41}K and ^{87}Rb atoms [65]. After the molecules decayed into their electronic ground state, Stimulated Raman Adiabatic Passage (STIRAP) [66] was applied to transfer the molecules into their rovibrational ground state [67].

The second indirect way to produce ultracold molecules is the *magnetoassociation* of molecules from an atomic sample. Atoms are first cooled close to quantum degeneracy before sweeping the magnetic field across a Feshbach resonance. These resonances were first observed in 1998 in homonuclear samples [68, 69], and in 2004 in heteronuclear mixture experiments [70, 71]. Since then, Feshbach resonances were detected in numerous ultracold homo- and heteronuclear samples [72]. In 2003, the first homonuclear ultracold molecules were formed using this technique [73–79], before heteronuclear molecules were associated in mixtures of KRb [80], LiK [81, 82], ^{87}RbCs [83], NaK [84] and NaLi [85]. This development led to BECs of weakly bound molecules [86–88].

Feshbach molecules are in a very highly excited state and thus are only very weakly bound. Their binding energy is only in the range of a few MHz compared to, for example, the ∼110 THz binding energy of the ground state of ^{87}RbCs. The weakly bound molecules are not stable and have a negligible dipole moment [89], hence the molecules need to be transferred into their absolute ground state, which can be done using the STIRAP technique. Since magnetoassociation takes place at small internuclear separations, generally two transitions with good Franck-Condon factors exist, that can be used to transfer the Feshbach molecules via an electronically excited intermediate state into the absolute ground state. This was achieved in 2008 with Rb_2 [90], Cs_2 [91] and with a heteronuclear sample of KRb molecules [92]. Ground state KRb molecules are still the only ultracold sample of polar molecules with a high PSD at this time. Recently, it was possible to measure spin-exchange interactions in experiments using these molecules in an optical lattice [93].

Currently, many groups are working on experiments for the production of a polar molecular sample using a combination of magnetoassociation and STIRAP transfer to the absolute ground state using different combinations of atoms, suitable for laser cooling [85, 94–99].

In this thesis, our work towards the realisation of a polar sample of ground state ^{87}RbCs molecules using this combination of techniques is described.

1.2 Thesis overview

The thesis is structured as follows: In chapter 2, the basic background theory for understanding the results is described. It covers the description of scattering at low temperatures and the origin of Feshbach resonances, before a model for the STIRAP transfer is given and the potentials of the ^{87}RbCs molecule are described. In the following chapter, an overview of the experimental apparatus and the techniques used to produce an ultracold mixture of Rb and Cs are described. The optical system for the implementation of STIRAP is discussed in chapter 4. Here, an overview of the experimental requirements is given before optical cavities are described and the Pound-Drever-Hall (PDH) locking scheme is introduced. The following four chapters (5 to 8) represent the results part of this thesis. The investigation of scattering properties and search for Feshbach resonances in a mixture of ^{85}Rb and Cs (chapter 5) and ^{85}Rb alone (chapter 6) are presented. After this, the magnetoassociation of Cs_2 molecules and experiments utilising control of their internal state are presented in chapter 7. In the final results chapter, our work on ^{87}RbCs molecules is described. First, the magnetoassociation of the heteronuclear molecules is presented, before work on weakly bound molecules and spectroscopy on vibrational levels of an electronically excited state and the rovibrational ground state are shown. Finally, an outlook on future experiments, including STIRAP transfer to the absolute ground state of ^{87}RbCs molecules and experiments using ^{85}Rb rather than ^{87}Rb, is given in chapter 9.

1.3 Publications

The following publications resulted from the work presented in this thesis.

Bose-Einstein condensation of ^{87}Rb in a levitated crossed dipole trap
D.L. Jenkin, D.J. McCarron, M.P. Köppinger, H.W. Cho, S.A. Hopkins and S.L. Cornish
Eur. Phys. J. D ***65*** *11-18 (2011)*

A high phase-space density mixture of ^{87}Rb and ^{133}Cs: towards ultracold heteronuclear molecules
H.W. Cho, D.J. McCarron, D.L. Jenkin, M.P. Köppinger and S.L. Cornish
Eur. Phys. J. D ***65*** *125-131 (2011)*

Dual-species Bose-Einstein condensate of ^{87}Rb and ^{133}Cs
D.J. McCarron, H.W. Cho, D.L. Jenkin, M.P. Köppinger and S.L. Cornish
Phys. Rev. A ***84****, 011603 (2011)*

Feshbach spectroscopy of an ultracold mixture of ^{85}Rb and ^{133}Cs
H.W. Cho, D.J. McCarron, M.P. Köppinger, D.L. Jenkin, K.L. Butler, P.S. Julienne, C.L. Blackley, C.R. Le Sueur, J.M. Hutson and S.L. Cornish
Phys. Rev. A ***87****, 010703 (2013)*

Feshbach resonances in ultracold ^{85}Rb
C.L. Blackley, C.R. Le Sueur, J.M. Hutson, D.J. McCarron, M.P. Köppinger, H.W. Cho, D.L. Jenkin and S.L. Cornish
Phys. Rev. A ***87****, 033611 (2013)*

Production of optically trapped ^{87}RbCs Feshbach molecules
M.P. Köppinger, D.J. McCarron, D.L. Jenkin, P.K. Molony, H.W. Cho, C.L. Blackley, C.R. Le Sueur, J.M. Hutson and S.L. Cornish
Phys. Rev. A ***89****, 033604 (2014)*

Chapter 2

Background Theory

In this chapter, the basic theory necessary to understand the results and motivation of this work is described. First, an overview of the properties of polar molecules is presented before a short description of ultracold scattering and Feshbach resonances is given. After this, a simple outline of the STIRAP process is given as a motivation for the optical setup described in chapter 4. Only a brief introduction is given here and more details can be found in several review papers [17, 40, 59, 66].

2.1 Dipole moments and heteronuclear molecules

In the introduction, it was pointed out that ultracold polar molecules open the door to many novel experiments. Their characteristic property is the long-range, anisotropic dipole-dipole interaction, which contrasts the isotropic contact interactions usually taking place in ultracold atomic samples [100]. Particles can have both, magnetic and electric dipole moments (μ and d respectively). The maximum energy due to dipole-dipole interactions, when all dipoles point in the same direction, is [36]

$$V_{\mathrm{dd}} = \frac{C_{\mathrm{dd}}}{4\pi} \frac{1 - 3\cos^2\theta}{r^3}, \tag{2.1}$$

where C_{dd} is the coupling constant equal to d^2/ϵ_0 for an electric dipole d and

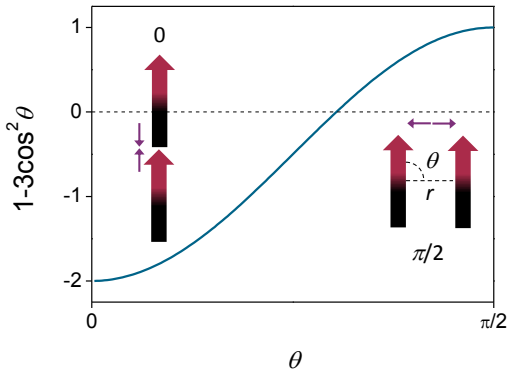

Figure 2.1: Angular dependency of dipole-dipole interactions according to equation 2.1. The separation between the dipoles is r and the angle between the internuclear axis and the direction of the dipoles is θ. The interactions are repulsive for particles sitting side by side and attractive with twice the strength for dipoles in a 'head-to-tail' orientation. The interactions vanish for $\theta \simeq 54.7°$

$\mu_0\mu^2$ for a magnetic dipole μ and ϵ_0 is the permittivity of vacuum and μ_0 the permeability of vacuum. Here, r is the distance between the particles and θ is the angle between the axis connecting the two particles and the direction of the polarisation. From this equation, the long range behaviour $(1/r^3)$ and the anisotropic character $(1 - 3\cos^2\theta)$ are apparent. The latter factor varies from -2 to 1 as the angle θ varies from 0 to $\pi/2$ (see figure 2.1), thus the interactions can be repulsive or attractive. The interactions vanish for the angle $\theta = \arccos(1/\sqrt{3}) \simeq 54.7°$.

The coupling in the electric case is typically larger than in the magnetic case. The electric dipole moment is of the order of $d \sim q_e a_0$, with the electron charge q_e and the Bohr radius a_0, whereas the magnetic dipole moment is of the order of μ_B. This leads to a ratio between the strength of the magnetic over the electric dipole moment of the order of $\frac{\mu_0\mu^2}{d^2/\epsilon_0} \sim 10^{-4}$.

The absolute strength of dipole-dipole interactions can be expressed by the dipolar length [36]

$$a_{dd} = \frac{C_{dd} m}{12\pi\hbar^2}, \tag{2.2}$$

where m is the mass of the particles. This makes it possible to compare the interaction strength due to dipole-dipole interactions in an ultracold sample

to the one from short-range interactions as described by the s-wave scattering length a. The ratio between them is

$$\epsilon_{\mathrm{dd}} = \frac{a_{\mathrm{dd}}}{a}. \tag{2.3}$$

The definition for the dipolar length is such that a homogeneous condensate is unstable against 3D collapse when $\epsilon_{\mathrm{dd}} \geq 1$.

To produce a polar system using molecules, a heteronuclear molecule with a permanent dipole moment has to be chosen. When an indirect cooling method is applied, the constituent atoms need to be suitable for laser cooling. This narrows the choice of species. The relevant properties of some suitable molecules are presented in table 2.1 together with the properties of selected atoms. The molecules have to be in the absolute ground state since the dipole moment is proportional to r^{-7} [101] and is vanishingly small for higher rovibrational states. Finally, an external electric field has to be applied to orient the molecules. The dipole interactions can be tuned by the strength of the electric field (see figure 9.3).

Table 2.1 shows the beneficial properties of RbCs. The molecule is stable against atom exchange reactions of the form $2\mathrm{RbCs} \rightarrow \mathrm{Rb_2} + \mathrm{Cs_2}$ since this reaction is endothermic [102]. Furthermore, a relatively small electric field gradient is required to induce a relatively large electric dipole moment. The rotational constant of the ground state $B_{\mathrm{rot}} = 1.66 \times 10^{-2}\,\mathrm{cm}^{-1}$ is relatively small and the critical electric field (E_{crit}), at which the molecules possess 1/3 of their maximum dipole moment, is $E_{\mathrm{crit}} = B_{\mathrm{rot}}/d$ [103].

2.2 Feshbach resonances / basic scattering theory

Ultracold atoms interact through collisions, which can be divided into two types. Elastic collisions make evaporative and sympathetic cooling possible and lead to thermalisation of an atomic sample, while inelastic collisions lead to heating and trap loss. During an experiment both types of collisions are always present and must be kept in a high elastic to inelastic collision

Species	Dipole moment	a_{dd} (a_0)	E_{crit} (kV/cm)	Stable
^{87}Rb	$0.5\,\mu_B$	0.2		
^{133}Cs	$0.75\,\mu_B$	0.6		
^{52}Cr	$6\,\mu_B$	15		
^{168}Er	$7\,\mu_B$	49		
^{164}Dy	$10\,\mu_B$	133		
KRb	0.62 D	4.5×10^3	3.7	No
RbCs	1.24 D	3.2×10^4	0.8	Yes
KCs	1.91 D	5.9×10^4	1.0	Yes
LiCs	5.53 D	4.0×10^5	2.1	No

Table 2.1: Dipole moment and dipolar length for various atoms and molecules in their rovibrational ground state. For molecules, the critical electric field E_{crit} is also given at which the molecules possess 1/3 of their maximum dipole moment. The last column states if the molecule is chemically stable. (Data taken from [72, 102–107]).

ratio, such that cooling is possible without large losses, i.e. efficient. Only then can a degenerate sample be produced. The interactions between ultracold particles can be described by a single parameter, the *s*-wave scattering length. The scattering length changes with magnetic field due to Feshbach resonances, which makes it possible to control the interactions in an ultracold atomic sample.

2.2.1 Basic scattering theory

Here we consider scattering between two particles in the positions $\vec{r}_1$ and $\vec{r}_2$ with masses m_1 and m_2 [108]. The interaction potential between the two particles is $V(\vec{r}_1, \vec{r}_2)$. Since the scattering problem is reduced to an effective single-particle process, the reduced mass $m_{\mathrm{r}} = \frac{m_1 m_2}{m_1+m_2}$ and the scattering potential described by $V(\vec{r}) = V(\vec{r}_1 - \vec{r}_2)$ is used. The relative velocity of the two particles is $\vec{v}$ and the relative momentum is $\vec{p} = m_{\mathrm{r}}\vec{v}$. From this follows the relative wave vector $\vec{k} = \vec{p}/\hbar$ with $k = |\vec{k}|$.

To describe the relative motion of two atoms, the Hamiltonian

$$H = \frac{\vec{p}}{2m_{\mathrm{r}}} + V(\vec{r}) \tag{2.4}$$

is used. The incident particle is described by a wave packet consisting of a superposition of plane waves $\Psi(\vec{r}) = e^{i\vec{k}\cdot\vec{r}}$, which leads to solutions of the form

$$\Psi_{\vec{k}}(\vec{r}) = e^{i\vec{k}\cdot\vec{r}} + f_k(\theta,\phi)\frac{e^{i\vec{k}\cdot\vec{r}}}{r}. \tag{2.5}$$

In this expression, the incident wave is split after the collision into the unperturbed part $e^{-i\vec{k}\cdot\vec{r}}$ and a scattered spherical wave $f_k(\theta,\phi)\frac{e^{i\vec{k}\cdot\vec{r}}}{r}$. $f_k(\theta,\phi)$ is the scattering amplitude depending on the relative wave vector and the angles θ and ϕ. To calculate the value of $f_k(\theta,\phi)$, the three dimensional Schrödinger equation has to be solved, which is complicated except for special cases. To circumvent this problem, the fact is used that the interaction potential is spherically symmetric $V(\vec{r}) = V(r)$, which means that the scattering amplitude only depends on θ. This makes it possible to expand the incident and scattered wave functions and write them in a set of spherical harmonic functions. Since θ is the only variable, the Legendre polynomials $P_l(\cos\theta)$ can be used. Therefore, the scattering amplitude depends on the angular momentum quantum number l and can now be written as

$$\begin{aligned} f(k,\theta) &= \frac{1}{2ik}\sum_l (2l+1)\left(e^{2i\delta_l(k)} - 1\right) P_l(\cos\theta) \\ &= \frac{1}{k}\sum_l (2l+1)\, e^{2i\delta_l(k)} \sin\delta_l(k) P_l(\cos\theta), \end{aligned} \tag{2.6}$$

where δ_l is the phase shift between the specific case and the free particle case, where $(V(r) = 0)$, for each outgoing partial wave $l = 0, 1, 2, \ldots$.

The differential scattering cross section

$$\frac{d\sigma}{d\Omega} = |f(\vec{k})|^2 \tag{2.7}$$

is the number of particles scattered per unit time into the solid angle Ω.

Integrating equation (2.7) over all angles gives the total scattering cross-section

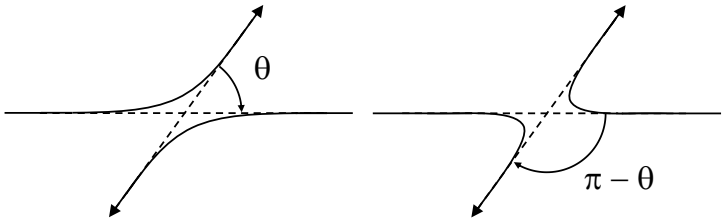

Figure 2.2: The two scenarios are identical in the case of scattering of indistinguishable particles.

$$\sigma = \frac{4\pi}{k^2} \sum_l (2l+1) \sin^2 \delta_l(k). \tag{2.8}$$

So far, only distinguishable particles were considered in this discussion. This means that it is possible to distinguish the two cases presented in figure 2.2. Their corresponding scattering amplitudes are $f(k,\theta)$ and $f(k,\pi-\theta)$. The particles involved in atomic and molecular collisions however are often not distinguishable and the two cases cannot be discriminated. This means that the wave functions must be (anti-)symmetric for bosons (fermions) and their scattering wave functions have the form $\Psi(\vec{r}_1,\vec{r}_2) = \epsilon \cdot \Psi(\vec{r}_2,\vec{r}_1)$ with $\epsilon = +1(-1)$ for bosons (fermions). Equation (2.5) can now be rewritten as

$$\Psi_{\vec{k}}(\vec{r}) = e^{i\vec{k}\vec{r}} + \epsilon e^{-i\vec{k}\vec{r}} + \Big(f(k,\theta) + \epsilon f(k,\pi-\theta)\Big)\frac{e^{ikr}}{r}, \tag{2.9}$$

and the differential cross section now is

$$\frac{d\sigma}{d\Omega} = |f(k,\theta) + \epsilon f(k,\pi-\theta)|^2, \tag{2.10}$$

with θ ranging between 0 and $\pi/2$. The Legendre polynomials possess a parity of $(-1)^l$ which leads to cancellation of all odd (even) partial wave contributions for bosons (fermions). The contribution of even partial waves is doubled for bosons and odd partial waves have no effect. The scattering cross section for bosons is

$$\sigma = \frac{8\pi}{k^2} \sum_{l\,\text{even}} (2l+1) \sin^2 \delta_l(k), \tag{2.11}$$

and for fermions the sum over all odd partial waves has to be taken. This

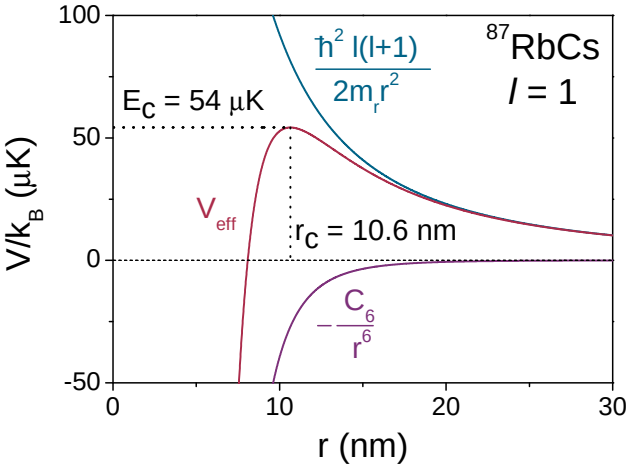

Figure 2.3: The effective potential V_{eff} building the centrifugal barrier according to equation (2.12). Here, the centrifugal barrier for the $l = 1$ partial wave is shown. Values for C_6 are listed in table 2.2.

is only true for collisions within a single species. When collisions can occur between different bosons as in the Rb–Cs experiment, odd partial wave collisions can also happen and the factor of 8π in equation (2.11) is reduced to 4π.

2.2.2 Low energy collisions

In general, several partial waves are involved in the scattering process of particles and therefore contribute to the scattering cross-section. For higher order modes ($l > 0$), a centrifugal term $\hbar^2 l(l+1)/(2m_{\text{r}}r^2)$ arises which leads to an effective barrier superimposed on the long range part of $V(r)$

$$V_{\text{eff}}(r) = -\frac{C_6}{r^6} + \frac{\hbar^2 l(l+1)}{2m_{\text{r}}r^2}. \tag{2.12}$$

This term leads to a barrier suppressing collisions of higher order partial waves below a certain temperature. The effective potential for Rb–Cs scattering of $l = 1$ is shown in figure 2.3. This barrier suppresses all but s-wave scattering below a temperature of $54\,\mu$K. At higher temperatures, p-wave collisions contribute to the elastic cross section. The barrier for d-wave scattering in this mixture is $282\,\mu$K high. The first centrifugal barrier in Rb

Species	C_6 (a.u.)	Partial Wave	Centrifugal Barrier (μK)
Rb–Rb	4709	d-wave	412
Cs–Cs	6890	d-wave	180
Rb–Cs	5694	p-wave	54
		d-wave	282

Table 2.2: C_6 coefficients for the scattering partners relevant for this work in atomic units [83, 109, 110] and the temperature below which only s-wave scattering contributes to the elastic cross section. Conversion of the C_6 coefficients into SI units is performed by multiplication with a_0^6 and the Hartree energy $E_\mathrm{h} = \hbar^2/(m_\mathrm{e} a_0^2)$.

(Cs), where d-wave collisions contribute, is $412\,\mu$K ($180\,\mu$K) high. The d-wave threshold is higher than the temperature in a MOT and thus d-wave collisions are not considered in a cold atom experiment. However, p-wave scattering is possible in a mixture experiment and thus contributes to the scattering properties between Rb and Cs in the magnetic trapping stage.

At low temperatures, the energy of the particles is not large enough to overcome the centrifugal barrier for partial waves $l > 0$ (see table 2.2) and access the interaction region. The scattering cross section for pure s-wave collisions is

$$\sigma = \frac{8\pi}{k^2} \sin^2 \delta_0(k). \tag{2.13}$$

The scattering phase shift scales as $\delta_l \propto k^{2l+1}$ at low energies where the relative wave vector $k \to 0$ [108]. The s-wave scattering length can be defined as

$$a = -\lim_{k\to 0} \frac{\tan \delta_0(k)}{k}, \tag{2.14}$$

and the resulting scattering cross section, neglecting influences due to the effective range, can be written as [111]

$$\sigma_0 = \frac{8\pi a^2}{1 + k^2 a^2}. \tag{2.15}$$

Two limits can be found for this equation. At large velocities $ka \gg 1$, the scattering cross section is

$$\sigma_{\text{unitarity}} = \frac{8\pi}{k^2}, \tag{2.16}$$

independent of the scattering length and limited by the relative energy of the particles. This is called the unitarity limit. For low velocities, where $ka \ll 1$, the scattering cross section is

$$\sigma_{\text{ultracold}} = 8\pi a^2, \tag{2.17}$$

and hence is isotropic and only depends on the s-wave scattering length a, not on the particle energy any more. In this ultracold limit, the interactions are equivalent to scattering of hard spheres with radius a. The value for a can be positive or negative, where a positive scattering length describes repulsive interactions and negative values describe attractive interactions between the particles.

2.2.3 Feshbach resonances

Feshbach resonances are one of the core elements used in the work for this thesis. Both the change in scattering interactions with magnetic field between ultracold particles, discussed in chapters 5 and 6, and the production of weakly bound molecules, presented in chapters 7 and 8, rely on the existence of Feshbach resonances.

A Feshbach resonance occurs when two colliding atoms have the same energy as a bound state of a higher lying potential. This situation is presented in figure 2.4(a). The energy of two colliding ultracold atoms is very small and can thus be described by the asymptotic far field energy of their molecular potential. This is represented by the open channel in figure 2.4. When another, higher lying potential (closed channel) supports a bound state at an energy close to the one of the two atoms, coupling between the states leads to mixing of the two channels. In general, the magnetic moments of the open and closed channels are different, which makes it possible to tune the

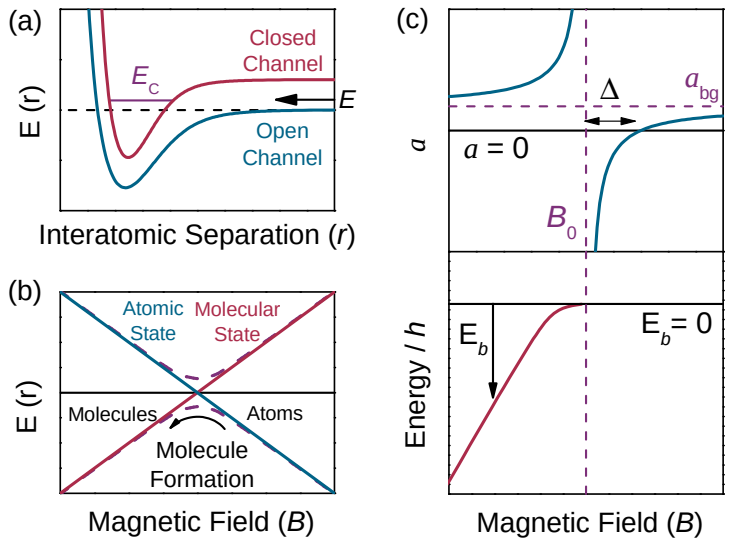

Figure 2.4: (a): A Feshbach resonance occurs when the energy of a bound state of a closed channel is degenerate with the energy of two atoms scattering in the open channel. (b): An atomic and a molecular state cross at a Feshbach resonance. Coupling between the states leads to molecule formation while sweeping adiabatically across the resonance. (c): The evolution of the scattering length at a resonance according to equation (2.21) is presented in the top panel. The bottom panel shows the bound state existing at the high scattering length side of the resonance. The binding energy is given relative to the energy of the two free atoms.

relative position of the states by changing the magnetic bias field. Feshbach resonances generally exist for pairs of alkali-metal atoms due to the coupling provided by the difference between the singlet and triplet potential curves and the magnetic dipolar interaction between the electron spins [112].

From the experimental point of view, a Feshbach resonance causes a change in scattering length a with magnetic field B of the form [113]

$$a(B) = a_{\mathrm{bg}}\left(1 - \frac{\Delta}{B - B_0}\right). \tag{2.18}$$

Here, B_0 is the field at which the scattering length is infinite (the 'pole' of the resonance), Δ is the theoretical width of a Feshbach resonance (the difference in magnetic field from the pole to the closest zero crossing of the scattering length) and a_{bg} is the background scattering length away from the resonance. Its value is determined by the position of the last bound vibrational level of the open channel. A plot of the function is presented in the top panel of figure 2.4(c). Since a Feshbach resonance can be used to adjust the s-wave scattering length, the interactions in an ultracold sample can be controlled over a wide range. This can be used to optimise evaporative cooling and to tune the interactions in a BEC [114].

2.2.4 Feshbach molecule formation

Molecules can be formed by a magnetic field sweep across a Feshbach resonance [115]. This mechanism is pictured in figure 2.4(b). The energy of the two free atoms is lower on one side of the resonance and the energy of the bound molecule is lower on the other side. Since the two states are coupled, the population follows the avoided crossing from one state into the other during an adiabatic magnetic field sweep across the resonance. The crossings can be described within the Landau-Zener model where avoided level crossings are characterised by two parameters: the coupling strength V is one-half the energy splitting between the two states at the crossing point and $\Delta\mu$ is the difference in magnetic moment of the two states. Now the critical ramp speed, $\dot{r}_{\mathrm{c}}$ in units of G/ms, can be defined as [116]

$$\dot{r}_{\mathrm{c}} = 10 \cdot \frac{2\pi V^2}{\hbar|\Delta\mu|}. \tag{2.19}$$

The crossing is diabatic, hence the population stays in the same state for fast magnetic field ramps $\dot{B} \gg \dot{r}_{\mathrm{c}}$. For slow ramps, $\dot{B} \ll \dot{r}_{\mathrm{c}}$, the population is transferred adiabatically to the other state. This technique works in both directions, hence the molecules can be dissociated by a magnetic field sweep in the opposite direction. This model can be used for molecule association, hence for avoided crossings between an atomic and a molecular state, and for changing the internal state of Feshbach molecules which is possible due to avoided crossings between two molecular states. Both types of crossings are used in chapters 7 and 8.

The bound state exists on the positive scattering length side of a Feshbach resonance and the relation between scattering length and binding energy of this state for a very large scattering length is [117]

$$E_{\mathrm{b}} = \frac{\hbar^2}{2m_{\mathrm{r}}a^2}. \tag{2.20}$$

This bound state energy is shown in the bottom panel of figure 2.4(c). The equation above is only valid in the non-linear part close to the pole of the resonance. The binding energy is plotted relative to the energy of the two free atoms. The slope of the binding energy with magnetic field is given by the difference in magnetic moment of the two channels involved in the Feshbach resonance and determines the magnetic moment of the molecules in the appropriate state. When the magnetic moment to mass ratio of both atoms forming the molecule are similar, which is true for Rb and Cs, the levitation gradient for the atoms and molecules is similar for bound states running parallel to threshold. This is important for atom-molecule separation using the Stern-Gerlach technique.

2.3 Weakly bound molecular states

Knowledge of the scattering length and weakly bound-state energies are essential for the work presented in this thesis. Hence, a close collaboration be-

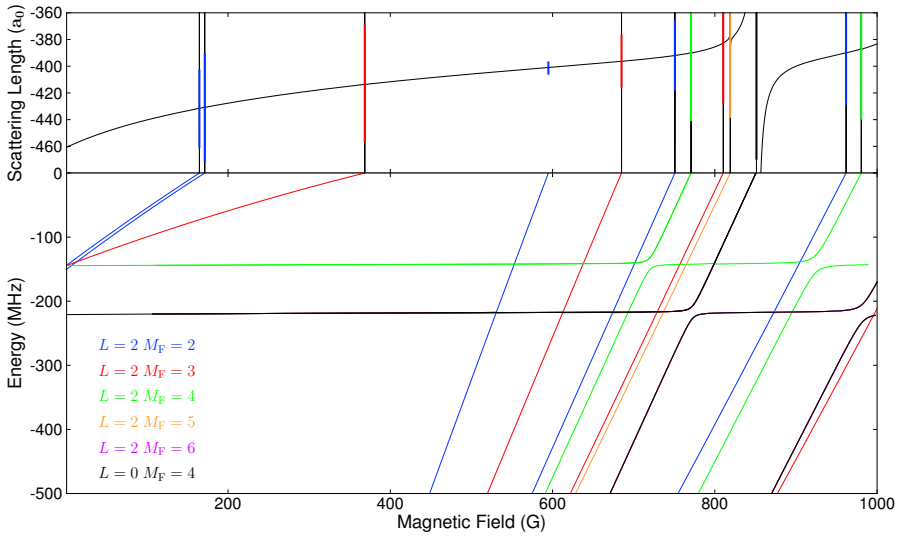

Figure 2.5: Top panel: ^{85}Rb s-wave scattering length in the (2,+2) state. Bottom panel: Binding energy of weakly bound molecules with respect to the energy of the free atoms in the (2,+2) state. Feshbach resonances are marked with lines and their different colours indicate their value of M_F (see legend). All calculations in this figure are for $M_{\rm tot} = 4$, corresponding to s-wave scattering in the (2,+2) channel [123].

tween theory and experiment throughout the work was very advantageous. All scattering lengths and bound state energies presented were calculated by Jeremy Hutson's group at Durham University. To obtain the s-wave scattering length, coupled-channel calculations [118] are performed using the MOLSCAT programme [119] as modified to handle collisions in external magnetic fields [120]. The bound states are calculated using the BOUND [121] and FIELD [122] packages.

For accurate results, the potential curves and the number of bound states have to be known. This information can be obtained from spectroscopic work [124] and the precision increased by the experimental localisation of Feshbach resonances [125, 126]. The potential curves used to determine the ^{85}Rb–Cs scattering length were obtained by mass scaling between ^{87}Rb–Cs and ^{85}Rb–Cs [127].

In figure 2.5, an example showing the ^{85}Rb s-wave scattering length (top panel) and binding energy of weakly bound $^{85}Rb_2$ molecular states (bottom panel) is presented. Narrow Feshbach resonances are indicated by vertical

lines. A broad resonance exists at 851.3 G, where the characteristic evolution of the scattering length at a Feshbach resonance can be observed. The resonances appear where molecular bound states cross the atomic threshold in the bottom panel. This picture can be compared to figure 2.4(c), showing the general evolution of the scattering length and the corresponding bound state at a Feshbach resonance.

The set of quantum numbers used for the near-threshold levels are slightly different for Cs_2 molecules and RbCs molecules. Cs_2 molecules are described by $n(f_1 f_2)FL(M_F)$, where n is the vibrational level counted from the least bound state, f_i are the zero-field levels of the atoms, F is the resultant of the f_i, L is the partial-wave angular momentum, and $M_F = m_1 + m_2$ following [110]. For RbCs molecules a different set of good quantum numbers is used and they are described by $|n(f_{\mathrm{Rb}}, f_{\mathrm{Cs}})L(m_{f_{\mathrm{Rb}}}, m_{f_{\mathrm{Cs}}}), M_{\mathrm{tot}}\rangle$ with the magnetic sublevels $m_{f_{\mathrm{Rb}}}$ and $m_{f_{\mathrm{Cs}}}$ and the sum of all angular momenta projected onto the field axis $M_{\mathrm{tot}} = m_{f_{\mathrm{Rb}}} + m_{f_{\mathrm{Cs}}} + M_{\mathrm{L}}$ [83].

2.4 Levitation using a magnetic gradient field

A magnetic gradient field can be used to control the vertical acceleration of a particle with magnetic moment μ. When the magnetic gradient field has the value such that

$$\mu \frac{\partial B}{\partial z} - mg = 0, \tag{2.21}$$

the particles are exactly levitated against gravity. This is used in the experimental setup where the atoms and molecules are supported in the optical dipole trap and to separate atoms and molecules using the Stern-Gerlach method. Here different magnetic moment to mass ratios are used to obtain different accelerations. The magnetic moment of atoms and therefore their levitation gradient changes with magnetic bias field according to the Breit-Rabi diagram. The levitation gradients for ^{85}Rb, ^{87}Rb and ^{133}Cs at zero magnetic field and for molecular states used in this work are displayed in table 2.3.

Species	State	Magnetic Field (G)	Magnetic Moment (μ_B)	Levitation Gradient (G/cm)
^{87}Rb	(1,+1)	0	-0.50	30.5
^{85}Rb	(2,+2)	0	-0.67	22.4
^{133}Cs	(3,+3)	0	-0.75	31.1
$^{133}Cs_2$	-2(33)4g(4)	17	-0.9	51.9
$^{133}Cs_2$	-2(33)6g(6)	11	-1.5	31.1
^{87}RbCs	-1(1,3)s(1,3)	185	-1.33	29.1
^{87}RbCs	-6(2,4)d(2,4)	181.6	+1.5	-25.8
^{87}RbCs	-2(1,3)d(0,3)	181.0	-0.84	46.0

Table 2.3: Levitation gradient for different species used for the work presented in this thesis. The magnetic moment for atoms is given at zero magnetic bias field and that of the molecules at the relevant bias fields.

2.5 STIRAP

After the Feshbach association, the molecules are only weakly bound. These molecules have a short lifetime in the range of 100 ms and a negligible dipole moment [101]. Due to this, an additional step is needed to transfer the population into the absolute ground state. This can be achieved by Stimulated Raman Adiabatic Passage (STIRAP) where two pulses of frequency stabilised light are used for coherent state transfer of the population. The two light pulses couple three states as shown in figure 2.6. In our case $|1\rangle$ is the Feshbach state, $|2\rangle$ an electronically excited state and $|3\rangle$ the absolute ground state of the molecule. The states $|1\rangle$ and $|2\rangle$ are coupled by the pump field $\vec{E}_P(t)$ and the states $|2\rangle$ and $|3\rangle$ are coupled by the the Stokes field $\vec{E}_S(t)$. Generally, the initial and final states are long lived compared to the time of the STIRAP transfer, whereas the intermediate state undergoes spontaneous emission into a manifold of states.

The STIRAP process can be described by a three-level system coupled with two electric fields

$$\vec{E}(t) = \vec{E}_P(t)\cos(\omega_P t + \phi_P) + \vec{E}_S(t)\cos(\omega_S t + \phi_S), \tag{2.22}$$

with the frequencies of the two light fields ω_P and ω_S and their phases ϕ_P and ϕ_S. The single-photon detunings from resonance of the two transitions

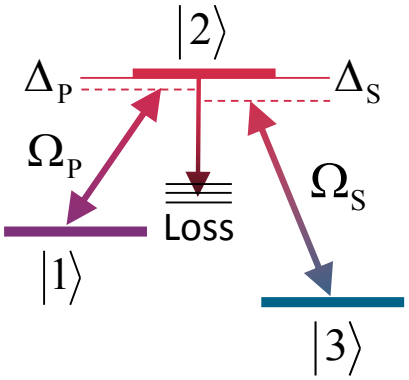

Figure 2.6: Scheme of the STIRAP transfer. The initial state $|1\rangle$ and final state $|3\rangle$ are coupled via an intermediate state $|2\rangle$. The coupling strengths of the transitions driven by the pump (Stokes) laser are described by their Rabi frequencies Ω_P (Ω_S) [128]. The detuning from resonance of the pump (Stokes) laser is Δ_P (Δ_S).

are described by

$$\begin{aligned} \hbar\Delta_P &= (E_2 - E_1) - \hbar\omega_P, \\ \hbar\Delta_S &= (E_2 - E_3) - \hbar\omega_S. \end{aligned} \tag{2.23}$$

The Hamiltonian of a three-level system in the rotating-wave approximation and neglecting losses can be written as

$$H(t) = \frac{\hbar}{2}\begin{pmatrix} 0 & \Omega_P(t) & 0 \\ \Omega_P(t) & 2\Delta_P & \Omega_S(t) \\ 0 & \Omega_S(t) & 2(\Delta_P - \Delta_S) \end{pmatrix}. \tag{2.24}$$

The eigenstates of this Hamiltonian for zero two-photon detuning ($\Delta_P - \Delta_S = 0$) are

$$\begin{aligned} |a^+\rangle &= \sin\theta\sin\Phi|1\rangle + \cos\Phi|2\rangle + \cos\theta\sin\Phi|3\rangle \\ |a^0\rangle &= \cos\theta|1\rangle - \sin\theta|3\rangle \\ |a^-\rangle &= \sin\theta\cos\Phi|1\rangle - \sin\Phi|2\rangle + \cos\theta\cos\Phi|3\rangle. \end{aligned} \tag{2.25}$$

The time varying mixing angle θ is defined by

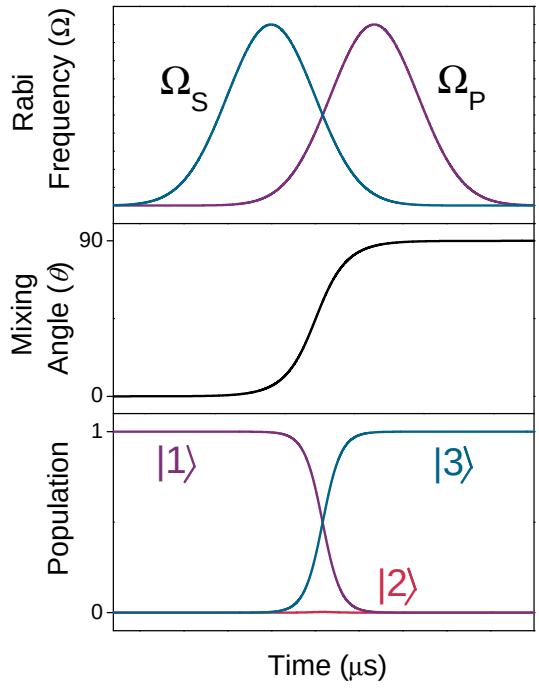

Figure 2.7: Top panel: Two Gaussian laser pulses induce the Rabi frequencies Ω_S and Ω_P coupling the states $|2\rangle$ and $|3\rangle$ and the states $|1\rangle$ and $|2\rangle$ respectively. The pulses are separated by the FWHM of the pulses. Centre panel: Evolution of the mixing angle θ over time during the two pulses are applied. Bottom panel: Population of the three states involved during the STIRAP transfer. Note that the lossy intermediate state $|2\rangle$ is never populated.

$$\tan\theta = \frac{\Omega_P(t)}{\Omega_S(t)}, \tag{2.26}$$

and the angle Φ is a function of the Rabi frequencies and detunings and is not relevant for the following discussion [129]. Note that the intermediate state $|2\rangle$ is not present in the eigenstate $|a^0\rangle$. This makes it possible to transfer the population from state $|1\rangle$ to $|3\rangle$ without populating state $|2\rangle$. As long as $\Omega_P = 0$, the population is in state $|1\rangle$ and changes in the Rabi frequency of the Stokes laser have no effect. The mixing angle can be changed slowly from 0 to 90° by altering the ratio of the two Rabi frequencies. Thus the population is transferred adiabatically from state $|1\rangle$ to $|3\rangle$. The evolution of the relevant values in time during the STIRAP process is shown in figure 2.7.

So far losses from the intermediate state were not considered. Also the inter-

mediate state is not meant to be populated during the STIRAP process and thus a highly efficient population transfer of theoretically 100 % is possible, the state transfer in the $|a^0\rangle$ state can be perturbed. This leads to a population of the lossy intermediate state. The efficiency in experiments is limited due to incoherence in the light fields [129, 130], but a transfer efficiency close to unity can be achieved [66]. The efficiency of a STIRAP transfer can be described by [130]

$$P = \exp\left(-\frac{\pi^2\Gamma}{\Omega_0^2\tau} - \frac{D\tau}{2}\right), \tag{2.27}$$

with the natural linewidth of the excited state Γ, the pulse duration τ. D is a factor describing the relative linewidth of the two lasers and Ω_0 is the reduced Rabi frequency where $\Omega_0 = \sqrt{\Omega_P^2 + \Omega_S^2}$. The Rabi frequency is defined as $\Omega = \vec{d}\cdot\vec{E}/\hbar$ with the dipole matrix element $\vec{d}$ and the electric-field amplitude $\vec{E}$. The consequences of equation (2.27) for an experimental setup are discussed in chapter 4.

2.6 RbCs molecular potentials

The STIRAP transfer relies on the existence of transitions that can be used to couple the three states. The RbCs Feshbach molecules belong predominantly to the $a^3\Sigma^+$ potential and hence have triplet character and the final rovibrational ground state of the $X^1\Sigma^+$ potential has singlet character. If all the states would be described accurately by the Hund's cases, selection rules ($\Delta S = 0$) would prevent optical dipole transitions between these states. However, it was proposed that electronically excited states with mixed character exist [89, 131–133] due to strong spin-orbit coupling in heavy alkali dimers. Through strong mixing of the $A^1\Sigma^+$ and the $b^3\Pi^+$ state, common vibrational levels of the two states exist that have mixed singlet and triplet character. This makes coupling between the three states possible. The potential energy curves supporting the states relevant for the proposed STIRAP scheme are presented in figure 2.8. Another important factor is the coupling strength between the different states. Large transition dipole moments (Franck-Condon factors) were proposed, since the turning points of the relevant potentials

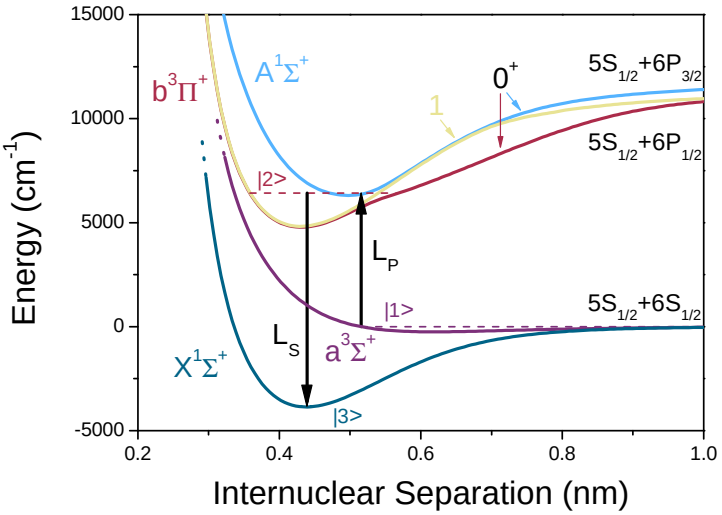

Figure 2.8: Molecular potentials involved in the STIRAP scheme proposed [131, 132] and experimentally realised in the Innsbruck group [94]. The triplet Feshbach state $|1\rangle$ is coupled to the singlet ground state $|3\rangle$ via a mixed intermediate state $|2\rangle$. The transitions for the proposed STIRAP sequence are indicated by arrows. The wavelength of the two lasers is $\lambda_P = 1556\,\text{nm}$ and $\lambda_S = 980\,\text{nm}$. The molecular term symbols are described in appendix A.

were expected to lie above each other [132].

Possible candidates for the intermediate state due to singlet-triplet mixing and relatively large transition dipole moments are in the range between $6300\,\mathrm{cm}^{-1}$ and $6600\,\mathrm{cm}^{-1}$ above the $5S_{1/2} + 6S_{1/2}$ threshold, which corresponds to a wavelength between 1515 nm and 1587 nm [89, 94]. Since the binding energy of the absolute ground state is measured to be $3811.5755(16)\,\mathrm{cm}^{-1}$ [94], these states lie $10111\,\mathrm{cm}^{-1}$ to $10411\,\mathrm{cm}^{-1}$ above the ground state and require a wavelength between 960 nm and 989 nm.

However, later calculations proposed relatively small transition dipole moments [94]. Measurements by the Innsbruck group using the $(v' = 29, J' = 1)$ intermediate state resulted in normalised Rabi frequencies of $\Omega_\mathrm{P} = 2\pi \times 0.33\,\mathrm{kHz}/\sqrt{\mathrm{mW/cm^2}}$ and $\Omega_\mathrm{S} = 2\pi \times 0.51\,\mathrm{kHz}/\sqrt{\mathrm{mW/cm^2}}$ for the two transitions of a STIRAP transfer performed in this group [134], where v' describes the vibrational and J' the rotational level of the electronically excited state. This makes Rabi frequencies of the order of 500 kHz possible in a standard setup as it is described in this work. Although this value is smaller than in other experiments where several MHz are achieved [90–92], STIRAP transfer is still possible in this system.

Chapter 3

Experimental apparatus

The experimental setup is explained comprehensively in former publications and here only a brief overview of the experimental techniques relevant for this work is given [135, 136]. The main changes made to the experiment since the last publication are described in chapter 4. A detailed description of the cooling techniques introduced in this chapter can be found in review papers and textbooks [8, 9, 12, 137].

The experimental setup described in the following text is capable of producing a sample of ultracold heteronuclear Feshbach molecules. To achieve this, a setup is used that allows for cooling of two different atomic species to close to degeneracy, and incorporates coils that can produce precise magnetic fields for magnetoassociation. The different techniques involved to achieve this are described in this chapter. The focus is on the optical dipole trap where the final cooling stage takes place and on the production of stable magnetic fields used for the search of Feshbach resonances and magnetoassociation.

3.1 Experimental overview

The experimental sequence used to produce an ultracold mixture of ^{87}Rb and ^{133}Cs can be divided into several steps.

A background gas of Rb and Cs is produced in a vacuum chamber using dispensers before the atoms are loaded into a pyramid MOT [138, 139]. From here, the cold atoms are pushed through an aperture at the apex of the

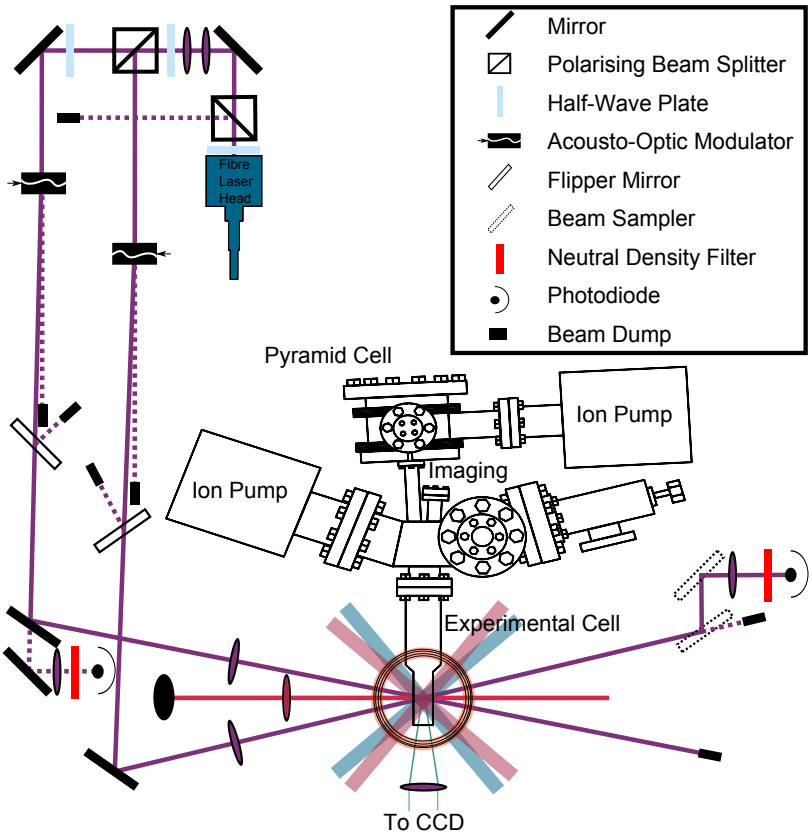

Figure 3.1: The vacuum chamber consists of a pyramid cell, where atoms are loaded from a background gas into a pyramid MOT. Subsequently they are transferred into a high vacuum glass cell (experimental cell) where they are loaded into a six beam MOT (blue and pink beams) and further cooled in a magnetic quadrupole and optical dipole trap (purple beams). The two dipole trap beams are derived from a single fibre laser and intersect in the centre of the magnetic trapping coils at an angle of $\sim 22°$. The red beam represents the molecular spectroscopy and STIRAP beams coming from a lower lying level of the experimental setup (see chapter 4.4.3). The light for absorption imaging is coupled through the flange labelled 'imaging' into the vacuum chamber.

pyramid along a differential pumping stage into the 2nd MOT, which is situated in an ultra-high vacuum glass cell. After sufficient atoms are collected in the 2nd MOT, a compressed MOT stage [140] is performed, followed by further cooling in an optical molasses [141]. Subsequently, the atoms are optically pumped into their individual low-field seeking stretched states, before they are loaded into a magnetic quadrupole trap, where radio frequency (RF) evaporative cooling is applied to cool the atoms further and increase their PSD. When losses due to Majorana spin flips prohibit further efficient cooling [142], the atoms are loaded into an optical dipole trap [143]. Here atoms are transferred into their absolute ground state using rapid adiabatic passage and a magnetic gradient field is applied to levitate the atoms against gravity. Reduction of the trap beam power leads to evaporative cooling and a quantum degenerate gas can be formed. During the final cooling process and for magnetoassociation, stable magnetic bias fields are applied.

The vacuum chamber and optics of the optical dipole trap are placed on one optical bench, from now on called the 'experimental table'. A sketch of the vacuum chamber and optics of the dipole trap and STIRAP transfer is shown in figure 3.1. The light frequencies necessary for laser cooling, repumping, optical molasses and imaging are derived on a second optical bench, from now on called the 'laser table'. The light is transferred between the tables using polarisation-maintaining single-mode optical fibres. The experimental sequences are computer controlled using a LabView-based programme.

3.1.1 Laser light

Two similar optical setups are used for simultaneous laser cooling of Rb and Cs. The same lasers and only minor changes in the optical setup are used to cool ^{85}Rb or ^{87}Rb. The closed D_2-line transitions used for laser cooling are at a wavelength of $\sim 780.2\,\text{nm}$ for Rb and $\sim 852.3\,\text{nm}$ for Cs. The hyperfine structure of ^{85}Rb, ^{87}Rb and ^{133}Cs and the transitions relevant for this work are presented in figure 3.2. One Toptica DL 100 'master laser' is used for each species for laser cooling in the 2nd MOT, imaging of the atoms and injection of a home-built slave laser which provides the cooling light for the pyramid MOT. The frequencies of the master lasers are locked using modu-

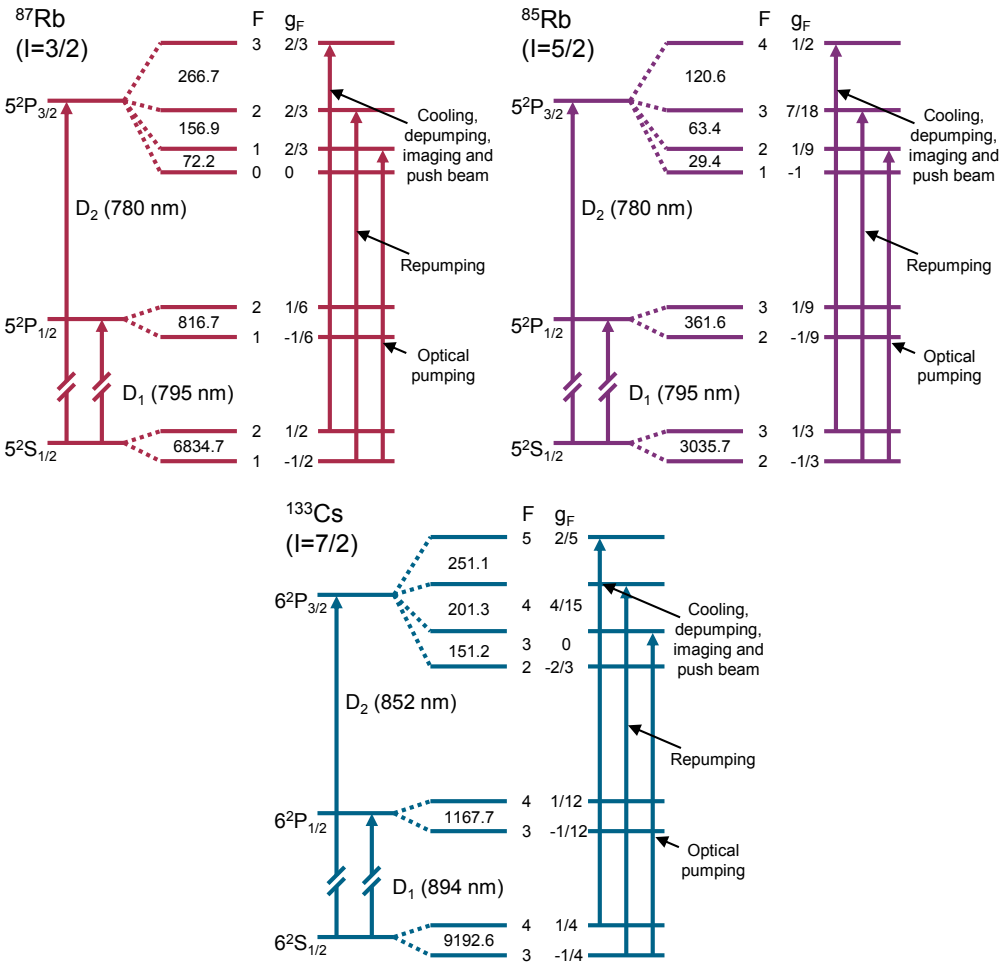

Figure 3.2: Energy level diagrams for the atomic species used in the experiment. The transitions driven by lasers are indicated by arrows. The splittings are given in MHz and are not to scale. Figure taken from [136].

lation transfer (MT) spectroscopy [144–146]. One home-built external cavity diode laser (ECDL) for each species provides the repumping light for both the pyramid and the 2$^{\text{nd}}$ MOT, plus the light for optical pumping. These lasers are frequency stabilised using frequency modulation (FM) spectroscopy [147, 148]. When ^{85}Rb is cooled in the experiment, the repump laser is locked using dichroic atomic vapour laser locking (DAVLL) [149, 150] instead so all AOM frequencies can be maintained when switching between the two Rb isotopes. The exact AOM frequencies and laser detunings from the transitions as well as the optical and electronic setups for laser stabilisation are described elsewhere [135, 136].

3.1.2 Cooling sequence

A pyramid MOT is used as a source of ultracold atoms. This MOT is loaded from a background gas of ^{133}Cs and Rb in its natural abundance. All beams necessary for this two species MOT are overlapped on the laser table and transferred to the experimental table in a single optical fibre. This setup makes it simple to realign the MOT beams. Through an imbalance in the radiation pressure, the cold atoms are then pushed through a hole in the apex of the pyramid into the UHV region where they are trapped in the 2$^{\text{nd}}$ MOT. To guarantee good optical access, this MOT is situated in a glass cell. After a loading time of 30 s, typically 1×10^9 ^{87}Rb atoms and up to 3×10^8 ^{133}Cs atoms are trapped in the MOT. The ^{133}Cs MOT number is controlled using a servo circuit. The MOT fluorescence is detected by a photodiode and a servo circuit stabilises its output voltage by changing the RF power to the Cs repump AOM. This control is very important for the work presented in this thesis, since this is how the composition of the mixture in later stages of the experimental cycle is controlled. The Rb number is controlled by triggering the next experimental step at a particular MOT load. Light resonant with the Rb atoms is applied from one direction to displace the Rb atoms and increase the MOT load.

After the required Rb MOT load is reached, a 40 ms CMOT stage [140] is used to match the shape of the atomic cloud to the magnetic trap geometry. During this step the magnetic field gradient is reduced and the detuning

of the cooling lasers increased. Subsequently, the atoms are cooled to sub-Doppler temperatures in an optical molasses [141]. The magnetic field is switched off and the detuning of the cooling lasers detuned even further for 15 ms.

Until this point, the population of the atoms is distributed over all possible m_f states. Hence, circularly polarised light is applied to transfer all atoms into their magnetically trappable stretched state of the lower hyperfine ground state. This increases the number of atoms that can be trapped in the magnetic quadrupole trap and suppresses inelastic collisions which decrease the cooling efficiency. Subsequently, the magnetic quadrupole trap is loaded by increasing the magnetic field gradient in two linear ramps to its final value of 184(1) G/cm. The single steps are used to spin polarise the atoms, as atoms in the wrong spin states leave the trap at lower gradient fields. The high magnetic field gradient is chosen to increase the collision rate of the atoms and thus decrease the evaporation time. In a single species experiment, $6.2(2) \times 10^8$ ^{87}Rb atoms at a temperature of 140(10) μK and a PSD of $2.2(7) \times 10^{-6}$ can be detected in the magnetic trap. Following this, the atoms are cooled using forced RF evaporative cooling in the magnetic trap. This is done by a single linear RF sweep from 28.8 MHz to 6.6 MHz in 15.1 s. Since the depth of the quadrupole trap determined by the RF frequency is three times larger for ^{133}Cs than for ^{87}Rb, the ^{133}Cs cooling process relies on sympathetic cooling through elastic collisions with ^{87}Rb. The cooling process is stopped when Majorana losses prevent further efficient cooling [142]. At this stage, up to $7.3(3) \times 10^7$ ^{87}Rb atoms at a temperature of 33.6(3) μK and a PSD of $1.6(2) \times 10^{-4}$ are confined in the magnetic trap.

3.2 Optical dipole trap

Following the evaporation in the magnetic trap, the atoms are loaded into an optical dipole trap. The light for the trap is provided by a single-frequency IPG Photonics ELR-30LP-SF fibre laser with a maximum output power of 30 W at 1550 nm. The optical setup for this laser is shown in figure 3.1. The beams forming the dipole trap intersect at an angle of 22° at the position of the atoms and have a $1/e^2$ radius of 63 μm and 68 μm respectively. The

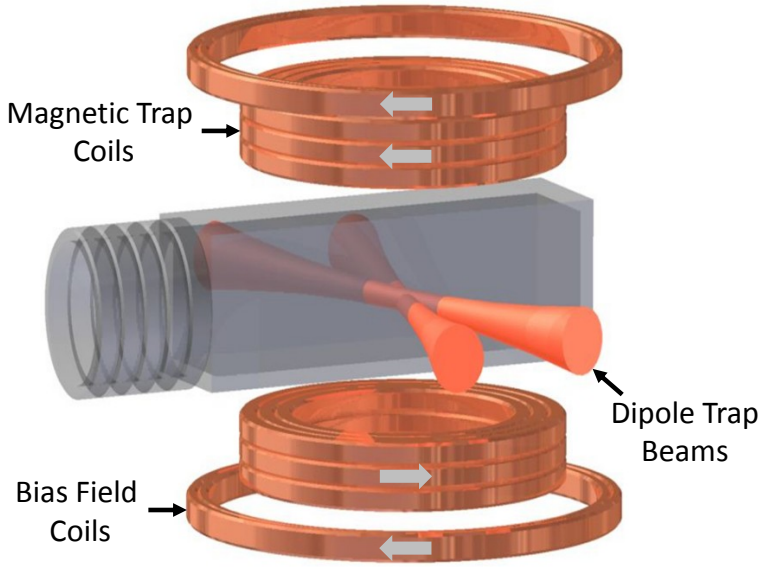

Figure 3.3: Simplified diagram of the experimental setup used for the final cooling stages. The two 1550 nm laser beams forming the optical dipole trap intersect at an angle of 22°. The magnetic trap coils also generate the gradient field for the MOT and the levitation of the atoms and molecules. The bias field coils provide the magnetic field for the Feshbach association.

power in the dipole trap beams is controlled by stabilising the output voltage of two photodiodes, detecting light from each beam, and stabilising their output voltages to a set value by varying the RF power to AOMs in each beam path of the dipole trap (see figure 3.1). The polarisability for ^{133}Cs at 1550 nm is 1.35 times larger than for ^{87}Rb, resulting in an equivalently deeper trap for ^{133}Cs [151].

The dipole trap is on during the evaporation process in the magnetic trap and is hence loaded continuously through elastic collisions. The final transfer into the dipole trap happens by decreasing the magnetic field gradient from 187 G/cm to 28 G/cm. The atoms are no longer completely levitated at this gradient and fall into the optical potential, which is located $\sim 100\,\mu$m below the magnetic trap centre. At the same time, the RF is reduced to 3.5 MHz. Typically 6 W in each beam are used during the loading process. The trap depth and frequencies for different dipole trap beam powers are given in table 3.1.

In a single species ^{87}Rb experiment, typically $1.45(6) \times 10^7$ atoms are

Beam Power (W)	Species	Trap Depth (μK)	f_{rad} (Hz)	f_{ax} (Hz)
6	Rb	76	612	118
	Cs	103	570	110
4	Rb	51	495	95
	Cs	69	466	90
1	Rb	13.7	247	47
	Cs	17.2	233	45

Table 3.1: Trap depth and frequencies for different beam powers in the optical trap for atoms in their absolute ground state and a magnetic field gradient of 30 G/cm, supporting the atoms against gravity.

loaded into the dipole trap at a temperature of 11.7(1) μK and a PSD of $1.39(3) \times 10^{-2}$. Once in the dipole trap, the atoms are transferred into their absolute ground state via rapid adiabatic passage [66] to suppress two-body losses which are forbidden in this state for energetic reasons [152]. This is essential for efficient cooling of ^{133}Cs [153, 154]. Here, a magnetic field ramp from 0 to $\sim$ 1 G is performed at a fixed RF field of 1.64 MHz. Thus the atoms are swept through resonance and the population is transferred into the absolute ground state.

When ^{133}Cs is being cooled in the dipole trap, the magnetic bias field is set to a value of 22 G due to a favourable intraspecies scattering length for efficient cooling. Further cooling in the optical dipole trap is performed via plain evaporation; a reduction of the beam power in the dipole trap decreases the trap depth. The atoms thermalise through elastic collisions supported by the high trapping frequencies of the optical dipole trap [143, 155–157].

Due to the different polarisabilities of Rb and Cs, the two species thermalise to different temperatures when no interactions occur. As we will show in chapter 5, this is the case over a wide magnetic bias field range in a mixture of ^{85}Rb and ^{133}Cs. In contrast to this, the interspecies scattering length between ^{87}Rb and ^{133}Cs is very large. At a bias field of 22 G, where evaporation of ^{133}Cs is efficient, the interspecies scattering length is 660 a_0. This leads to sympathetic cooling of Cs during the evaporation process, but also to large losses due to inelastic three-body collisions at high densities [158–160]. To circumvent this problem, a fast evaporation sequence is used to decrease the

peak density quickly.

The exact cooling sequence depends on the experiment performed and is described in each relevant chapter.

3.3 Magnetic fields

For the work presented in this thesis, stable magnetic bias fields up to $\sim 1200\,\mathrm{G}$ are required. The field is produced by three sets of coils. One small coil which can produce fast field ramps up to 50 G and two large coils which can produce the majority of high magnetic fields. The two large coils are used in series to produce high fields. However, when smaller fields below 400 G are needed they are separated and only one of them is used to increase the field stability.

The current in the coils is supplied by two Agilent power supplies (Agilent 6681A and Agilent 6690A) which are controlled via water cooled field-effect transistors (FETs). To stabilise the current through the coils, the current is measured using Hall effect sensors (Honeywell CSNL181) which generate a current 2000 times smaller than in the coils. This current is detected as a voltage drop across a sense resistor and is stabilised to a reference voltage set by the control programme. To guarantee good stability of the magnetic field, the sensing and feedback electronics have to be designed carefully. The combinations of capacitors on the feedback boards are selected to reduce current noise and suppress resonant frequencies of the individual coils. Furthermore, a $20\,\Omega$ power resistor (Isabellenhütte A-H2-20R0-F1-K2-0.1) is used as a sense resistor. Since the resistance is relatively large for a sense resistor and thus the power dropped over it is large, this resistor with 10 W load capacity and a small temperature coefficient of $\pm 10\,\mathrm{ppm/K}$ is chosen and mounted on a heat sink. This setup makes it possible to achieve a field stability of $\sim 0.001\,\mathrm{G}$ at 400 G, which means the current through the coils is stable to 1 part in 10^5.

3.4 Magnetic field calibration

The bias field produced in the experiment, is calibrated by driving microwave transitions between the ground states in the atoms. The separation of the two states changes with magnetic field due to the Zeeman effect. The precise field the atoms are exposed to can be determined by measuring this splitting and comparing it to the splitting calculated using the Breit-Rabi equation [161].

To calibrate the field, an ultracold sample of the desired species is produced and the microwaves applied during a 1 s hold in the optical dipole trap. The resonance can be detected as an atom loss feature. The typical uncertainty in the position of these features is in the range of 10 kHz and their width is ~ 100 kHz. This makes it possible to determine the magnetic bias field to an accuracy below 10 mG.

The microwave frequencies are generated using an Agilent E8257D analog signal generator. The output is connected to a Mini-Circuits MSP2T-18-12 switch to control when the microwaves are applied to the atoms. Due to the different splittings between the ground states of the individual species used in this experiment (see figure 3.2), the signal can then be connected to two different sets of amplifiers and waveguide-coaxial adapters to deliver microwaves to the atoms. For the calibration of the magnetic field using ^{133}Cs atoms, an AtlanTecRf AS6186 waveguide-coaxial adapter working in a frequency range from 8.2 to 12.4 GHz is used in combination with a Mini-Circuits amplifier ZVE-3W-183+ working in a range from 5.9 to 18 GHz. For the two Rb isotopes an AtlanTecRf AS6366 waveguide-coaxial adapter working in a frequency range from 2 to 8 GHz and a Mini-Circuits ZVE-3W-83+ amplifier working in a range from 2.6 to 7.8 GHz is used. With this combination, a wide range of microwave frequencies can be applied to the atoms and thus the field calibrated using all three species over the full accessible magnetic bias field range.

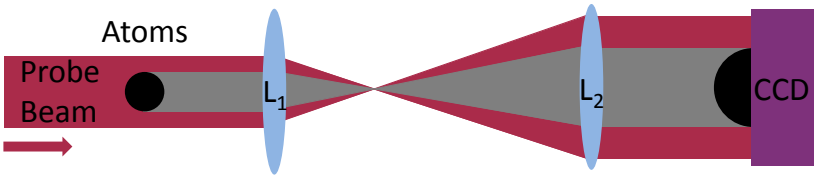

Figure 3.4: Optical setup for imaging the atomic cloud. Light is partially absorbed by atoms and detected by a CCD camera. The focal lengths of the two lenses are $f_1 = 80\,\text{mm}$ and $f_2 = 160\,\text{mm}$. The magnification of the imaging system is 1.858(2).

3.5 Imaging

Absorption images are taken to gain information about the ultracold sample in the form of its spatial profile and position. To take the images, the atoms are released from the trap for an appropriate time-of-flight (TOF). Then a quantisation field of 2.7(1) G is applied and the atoms are pumped out of their absolute ground states using the repump light. Subsequently, a $10\,\mu$s pulse of cooling light is applied. The atoms are pumped into their stretched states by the circularly polarised light before they absorb photons from the probe beam and decrease the intensity of the beam. To image atoms in magnetically trappable low-field seeking states, σ^- transitions are driven and σ^+ transitions are driven to image atoms in their high-field seeking absolute ground state. The spatial intensity profile of the probe beam after interacting with the atomic cloud is detected with a CCD camera (Andor iXon 885). The optical setup is shown in figure 3.4.

To obtain a density profile of the cloud, three images are taken. The first one is with the atoms, the probe beam light and background (I_1). The second one with the probe beam light and the background (I_2), and the third one only of the background (I_3). The optical depth (OD) of the atomic cloud can now be calculated at each point of the image using

$$OD = \ln\left(\frac{I_2 - I_3}{I_1 - I_3}\right), \tag{3.1}$$

with the intensities of light on each pixel for the three shots $I_{1,2,3}$. When a weak, resonant imaging beam is used, then

$$I = I_0 \exp(-OD), \tag{3.2}$$

with the detected intensity I and the intensity of the probe beam without atoms I_0.

The number of atoms in the cloud can be determined from a Gaussian fit to the absorption image using

$$N = \frac{4\pi^2}{3\lambda^2}\sigma_x\sigma_z OD_{\mathrm{PK}}, \tag{3.3}$$

with the widths of the Gaussian fit $\sigma_{x,z}^2 = k_{\mathrm{B}}T/m\omega_{x,z}^2$, the wavelength λ of the light and the peak optical depth OD_{PK}.

The temperature of the cloud in a harmonic trap can be calculated when the radial and longitudinal trap frequencies $\omega_{x,z}$ are known by

$$T_{x,z} = \frac{m\omega_{x,z}^2}{k_{\mathrm{B}}} \frac{\sigma_{x,z}^2(TOF)}{1+\omega_{x,z}^2 TOF^2}, \tag{3.4}$$

with the time-of-flight TOF and the cloud size after the time-of-flight $\sigma_{x,z}(TOF)$.

Chapter 4

STIRAP laser system

The experimental setup described in the previous section is capable of producing ultracold atoms and molecules via magnetoassociation. The next step is to transfer the weakly bound Feshbach molecules into their rovibrational ground state via STIRAP. The required experimental setup for the transfer is presented in this chapter. An optical cavity is used to produce stable reference points in frequency space. The frequency of two diode lasers is then stabilised to it using the Pound-Drever-Hall technique.

4.1 Experimental requirements

The theoretical background of the STIRAP transfer is described in section 2.5. In this section it is shown what this means for the requirements on an experimental setup. STIRAP is a coherent transfer during which the molecules have to be kept in a superposition state using two laser fields. Following equation (2.27), the condition for an efficient transfer is [65]

$$\frac{\Omega_0^2}{\pi^2\Gamma} \gg \frac{1}{\tau_p} \gg D, \tag{4.1}$$

with the reduced Rabi frequency $\Omega_0 = \sqrt{\Omega_\mathrm{P}^2 + \Omega_\mathrm{S}^2}$, the natural linewidth of the excited state Γ, the pulse duration τ_p and the relative linewidth of the two lasers D. Ω_P and Ω_S are the Rabi frequencies of the pump and Stokes transition. Thus a high transfer efficiency can be achieved either

by high laser powers (i.e. Rabi frequencies) or a small relative linewidth of the two lasers which allows a slower change of the ratio of the laser fields. Since the maximum power is limited by the lasers used, this sets specific requirements for the long and short term frequency stability. The linewidth of the excited state and the Rabi frequencies typically achieved in transitions between molecular states are both on the order of $\Omega = 1\,\mathrm{MHz}$ [94, 162], thus the pulse duration for the transfer is $\tau_p \sim 1\,\mu\mathrm{s}$ and the laser linewidths have to be on the order of 1 kHz.

The requirements for a STIRAP laser setup can be summarised by

1. Narrow linewidth lasers.
2. Tunability of the laser frequency.
3. Long term frequency stability.
4. Ability to produce light pulses.
5. High laser intensity at the position of the molecules.

To meet requirements 1 to 3, in previous experiments, frequency combs, optical cavities or a combination of both were used to produce stabilisation points at the required frequencies [91, 92]. For this work, we use an optical cavity and stabilise the frequency of both transfer lasers to it. The laser frequencies are locked using the Pound-Drever-Hall (PDH) technique which, in combination with a fast feedback locking circuit, allows us to narrow the linewidth of the lasers. To achieve tunability of the laser frequencies and cover the range between the resonances of the optical cavity, the laser frequencies are shifted with fibre-coupled electro-optical modulators (EOMs). Sidebands generated by the EOMs are used to stabilise the laser frequencies to the optical cavity, such that the carrier laser frequency (used for the STIRAP beams) can be scanned by changing the EOM frequencies. Acousto-optical modulators (AOMs) are used to control the laser power and to produce light pulses as short as 200 ns. Requirement 5 is accounted for by focussing the transfer beams down to the size of the molecular cloud.

4.2 Theory of optical cavities

4.2.1 Introduction

An optical cavity represents the central component of the setup utilised to stabilise the frequency of the lasers we will use for STIRAP. This section gives a brief overview of the cavity light field properties crucial to understand the laser locking technique used in the experiment. Far more detailed descriptions can be found in textbooks on optics and lasers [163–165].

Two different cavity designs are described below. First, a home-built design with a piezo to vary the resonator length and with high reflectivity mirrors for the two STIRAP wavelengths and at 852 nm so that the cavity can be stabilised to the Cs D_2 transition. The second cavity is a commercial, passive stable resonator which is used for the experiments presented in section 8.5.

An optical cavity is a resonator for light. It is formed when optical devices are arranged in a way such that a closed light path is formed. The easiest geometry is a linear resonator consisting of two mirrors facing each other separated by a distance L. A standing light wave is generated when the resonator length is a multiple integer of half the wavelength λ of the light, given by

$$L = n \cdot \lambda/2 \ , \ n \in \mathbb{N}. \tag{4.2}$$

Under this condition, there is a build up of light within the resonator (a longitudinal mode) and an appreciable fraction of the incident light is transmitted through the cavity. The frequency difference between two adjacent longitudinal modes is

$$\Delta\nu_{\mathrm{FSR}} = c/2L, \tag{4.3}$$

where c is the speed of light. This spacing is called the free spectral range (FSR) of the resonator. For convenience, and because such a design is used in the experiment, here only a linear resonator geometry is considered.

4.2.2 Theory

Cavity light field

Only electromagnetic waves with certain shapes fit into an optical cavity. These can be described by Gauss-Hermite beams. The Gaussian beam, which is usually used in this context, is only one of many solutions to the wave equation using the paraxial approximation.

Gauss-Hermite beams propagating in the z direction can be described by [163]

$$\begin{aligned} U = U_0 \exp\left(ikz - i\omega t\right) \frac{\exp\left(ikr^2/2q\right)}{q} \\ \times H_l\left(\sqrt{2}\frac{x}{w}\right) \times H_p\left(\sqrt{2}\frac{y}{w}\right) \\ \times \exp\left[-i\left(l+p\right)\alpha\right], \end{aligned} \tag{4.4}$$

where $k = 2\pi/\lambda$ is the wave number and ω the angular frequency. The first row is the Gaussian beam with $q = z - z_{\text{waist}} - iz_{\text{R}}$. The second row contains the Hermite polynomials H_l and H_p with their eigenvalues l and p. The third row is the increased phase shift with $\tan\alpha = z/b$ for beams with $l, p > 1$. Results for Hermite polynomials of different orders l and p are distinctive transverse modes of the electromagnetic field. The notation is TEM_{lp} and the simplest mode TEM_{00} is the Gaussian beam, for which $H_l = H_p = 1$. Substitution for q leads to the familiar equations for a Gaussian beam. The Rayleigh range z_{R}, which is the distance from the beam waist after which the radius increased by a factor of $\sqrt{2}$, is

$$z_{\text{R}} = \frac{\pi w_0^2}{\lambda}, \tag{4.5}$$

where w_0 is the radius at the beam waist. The radius of curvature of the wave front $R_\Phi(z)$ is given by

$$R_\Phi(z) = \frac{z^2 + z_{\text{R}}^2}{z}. \tag{4.6}$$

Although one typically works with the TEM_{00} mode, higher order Hermite-

Gaussian modes can be excited in an optical cavity as well. Their frequency spacing is [166]

$$f_{n,l,p} = \frac{c}{2L}\left[p + (n+l+1)\,\frac{\arccos\sqrt{g_1 g_2}}{\pi}\right], \tag{4.7}$$

with $g_i = 1 - L/\mathcal{R}_i$. Here $\mathcal{R}_i$ are the radii of curvature of the mirrors. These modes can be used as frequency references with alternative spacing than the FSR. Careful mode matching of the light into the resonator ensures that the TEM_{00} Gaussian mode is the dominant mode.

Reflection and transmission signal

Incident light on an optical resonator is split into a reflected and a transmitted part

$$E_\mathrm{r} = rE_\mathrm{i} \text{ and } E_\mathrm{t} = tE_\mathrm{i} \text{ with } 0 \leq r, t \leq 1, \tag{4.8}$$

where r and t are the reflection and transmission coefficient and $E_\mathrm{i} = E_0 e^{i(kz-\omega t)}$ is the incident plane light wave. Due to conservation of energy and neglecting losses in the mirrors, we assume $r^2 + t^2 = 1$.

We are interested in the beam reflected from the cavity. It is a superposition of the light being coupled out of the cavity after m round trips and the light that never entered the cavity since it was directly reflected at the first mirror. To calculate the total reflected beam, its phase Φ has to be taken into account. It changes during the round trip time T_Φ and an additional phase shift of π during the reflection at the first mirror has to be considered.

The phase evolves with each round trip by

$$\Phi = \omega T_\Phi = 2\pi\frac{2L}{\lambda}, \tag{4.9}$$

which means a factor of $e^{i\Phi}$ needs to be added for every round trip. According to figure 4.1, this leads to a reflected beam

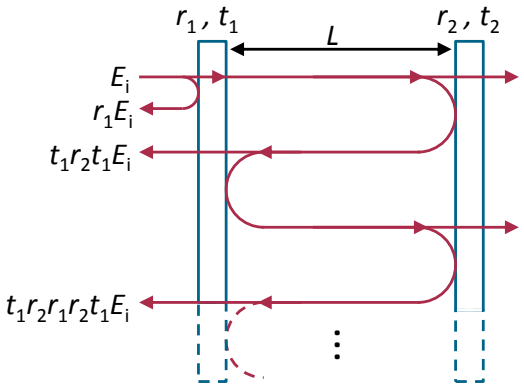

Figure 4.1: Light reflected from a cavity after a different number of round trips.

$$\begin{aligned} E_\mathrm{r} &= E_\mathrm{i}\left(-r_1 + t_1 r_2 t_1 e^{i\Phi} + t_1 r_2 r_1 r_2 t_1 e^{i2\Phi} + ...\right) \\ &= E_\mathrm{i}\left(-r_1 + \frac{t_1^2 r_2 e^{i\Phi}}{1 - r_1 r_2 e^{i\Phi}}\right), \end{aligned} \tag{4.10}$$

where the indices represent the individual mirrors. For a cavity, where $r_1 = r_2 = r$ and no losses occur, the reflected beam can be written as

$$E_\mathrm{r} = E_\mathrm{i} r \frac{e^{i\Phi} - 1}{1 - r^2 e^{i\Phi}}. \tag{4.11}$$

We derived this reflected beam thoroughly because it will be used in section 4.4.2 to derive the Pound-Drever-Hall error signal.

The transmitted intensity of an optical resonator can be described by the Airy function

$$\frac{I_\mathrm{t}}{I_\mathrm{i}} = 1 - \frac{I_\mathrm{r}}{I_\mathrm{i}} = \frac{1}{1 + \frac{2r^2}{(1-r^2)^2}(1 - \cos\Phi)}. \tag{4.12}$$

For $\Phi = 2\pi$, the beams interfere constructively and a transmission signal can be detected. This function is plotted in figure 4.2 for two different values of the reflectivity r.

The finesse $\mathcal{F}$ of a cavity describes the ratio between its FSR and the full width half maximum (FWHM) of a cavity peak $\delta\nu_{\mathrm{cav}}$. For a cavity with the same reflectivity $R = |r|^2$ for both mirrors, it is

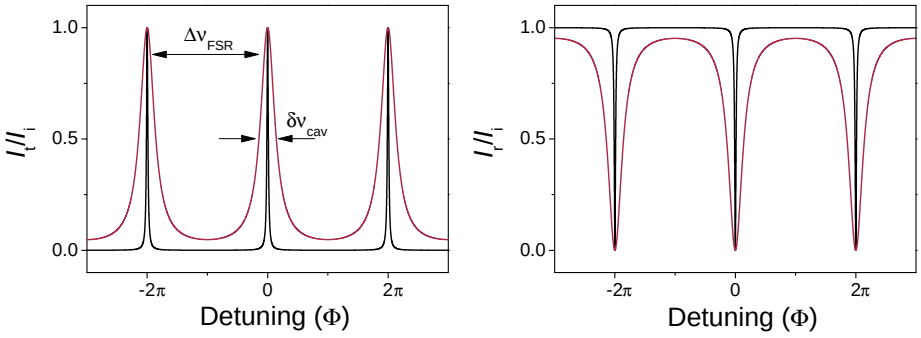

Figure 4.2: Cavity transmission (left) and reflection (right) signal for high (black) and low (red) reflectivity of the mirrors. The signal is shown for phase differences Φ between beams coupled out after two consecutive cavity round trips. At a phase difference of 2π the beams interfere constructively and a transmission maximum (reflection minimum) can be detected. The peaks are described by the Airy function expressed in equation (4.12).

$$\mathcal{F} = \pi \frac{\sqrt{R}}{1-R}. \tag{4.13}$$

Mode matching

Generally, many different Gauss-Hermite beam shapes fit into an optical cavity. These different shapes are referred to different transverse modes of the electric field. The aim is to couple as much light as possible into the TEM_{00} laser mode. To achieve this, the shape of the incoming laser beam must be matched to the cavity geometry. This means that the radius of curvature of the beam's wave front must match the radius of curvature of each mirror.

To calculate the required beam parameters, the properties of a Gaussian beam are used. The correct beam for a cavity with one flat mirror can be calculated quite easily. Since the radius of curvature is infinite at the waist, the beam is focussed onto the flat mirror and the distance and curvature of the second mirror determines the beam waist.

The required beam waists w_0 at the plane mirror can be calculated using the following expression derived from equation (4.5) and (4.6)

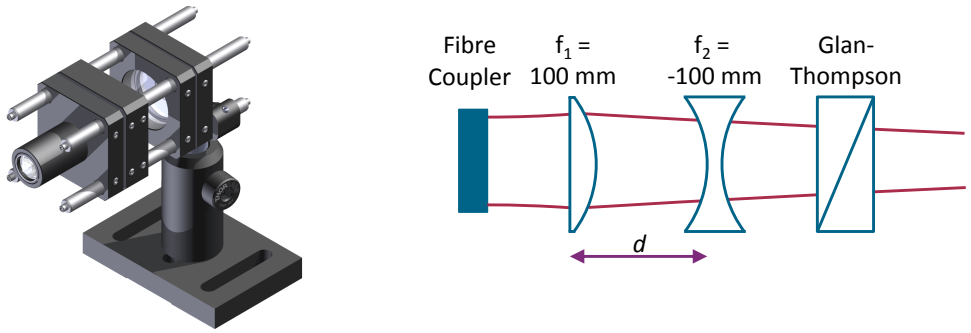

Figure 4.3: Setup to shape the laser beam to the resonator geometry. The optics shown on the right are mounted in the cage system on the left. The distance d is changed for fine adjustment of the beam waist.

$$w_1 = \frac{[4\,(L\mathcal{R} - L^2)]^{1/4}}{\sqrt{k}}, \tag{4.14}$$

where $\mathcal{R}$ is the radius of curvature of the second mirror.

An optical path has to be constructed that produces the calculated focus size at the first cavity mirror. Our experimental approach is to build a compact fibre-coupled cage system to clean up the beam profile and produce the correct waist size at an appropriate distance considering that optics for locking and overlapping, and the vacuum chamber containing the cavity has to fit in the beam path. Hence, we need a distance of about 50 cm from the last lens to the cavity.

An optical cage system shown in figure 4.3, consisting of two lenses and a matched initial beam radius is sufficient to produce the desired beam parameters. We simulated such a layout using the ABCD-matrix formalism. The results are presented in figure 4.4. For this data initial beams with an $1/e^2$-radius of 1 mm (980 nm) and 1.5 mm (1556 nm) are assumed. These sizes are used since they are achievable with standard fibre couplers. Both beams are focussed with an $f = 100$ mm lens mounted right after the fibre couplers. A second lens with $f = -100$ mm is mounted so that the distance d between the lenses is adjustable. The plots show the distance between the second lens and the focus on the left axes and the size of the focus on the right axes versus the separation d of the two lenses. The desired focus waists of

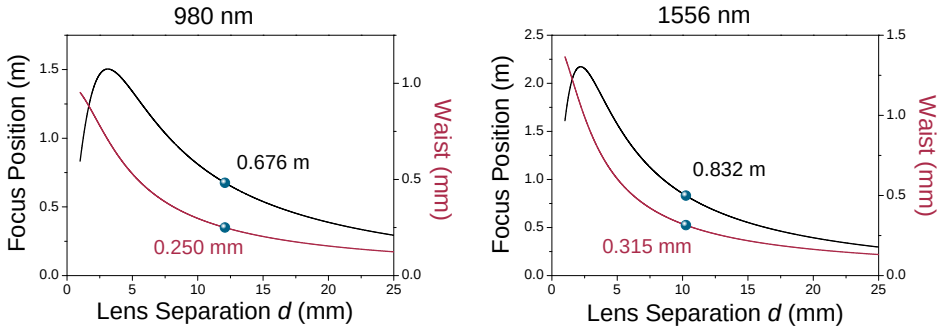

Figure 4.4: Focus position (black) and waist (red) versus lens position. An optical system illustrated in figure 4.3 is simulated. The waist position from the second lens and the $1/e^2$ radius at the waist are plotted for different lens separations d. The dots mark the parameters we aimed for to match the beam to the ULE cavity.

250 μm (980 nm) and 315 μm (1556 nm) are calculated using equation (4.14) for the commercial cavity presented in section 4.3.2. The results show that the required focusses are achieved for $d \sim 1$ cm in both cases. With 67.6 cm (980 nm) and 83.2 cm (1556 nm), both focusses are at an appropriate distance to place optics for locking in the beam path between the lens system and the cavity.

4.3 Design of optical cavities

In the following section, the two different cavity designs we used are described. A first approach was a cavity with a spacer made from Zerodur and a piezoelectric transducer to scan the length of the resonator. The second cavity, which is used in the final experimental setup, has a spacer made from ultra low expansion glass (ULE) and its length is passively stable. The basic properties of both cavities are summarised in table 4.1. The Zerodur resonator has a high finesse at the wavelengths of the two STIRAP transitions and for the wavelength of the Cs D_2 line while the ULE resonator has a high finesse only at the two STIRAP wavelengths. The reflectivity for both resonators is plotted in figure 4.5.

	L (cm)	$\Delta\nu_{\mathrm{FSR}}$ (GHz)	$\mathcal{R}$ (cm)	λ (nm)	Finesse $\mathcal{F}$	w_0 (μm)	$\delta\nu_{\mathrm{cav}}$ (kHz)
Zerodur	20	0.75	50	852	$3.11(1) \times 10^3$	258	241.2(8)
				980	$4.2(1) \times 10^3$	276	179(4)
				1556	$3.1(1) \times 10^3$	348	242(8)
ULE	10	1.5	50	980	$1.820(5) \times 10^4$	250	82.2(2)
				1556	$1.12(2) \times 10^4$	315	134(2)

Table 4.1: Parameters of the home-built Zerodur and the commercial ULE cavity. The mirror spacing L and radius of curvature $\mathcal{R}$ of the second cavity mirror define the beam waist at the position of the first mirror w_0 for optimum coupling into the TEM_{00} mode for each wavelength λ.

4.3.1 Three wavelengths cavity

A cavity with a high finesse for three different wavelengths was built. The mirrors have a high reflectivity at the two STIRAP wavelengths of 980 nm and 1556 nm and the Cs D_2 transition at 852 nm. The spacer, that keeps the two resonator mirrors at a fixed distance, is made from Zerodur glass. This material has a low thermal expansion coefficient of 0.2×10^{-7}/K, which means a spacer with a length of the order of 10 cm changes its length by 2 nm/K. Unfortunately, this already causes a significant drift of the resonance peaks of 6 MHz/K at 980 nm. As described in section 4.1, this drift is too large for a reproducible system.

To eliminate the drift an active stabilisation of the resonator length is implemented. A ring piezo is placed between the spacer and one of the mirrors, which can be used to tune the length of the resonator and to stabilise the length to a certain value. A laser, locked to the caesium D_2 line, is used to produce a reference signal for the stabilisation.

Cavity design

There are some basic properties to consider when planning a new cavity. The material and length of the spacer, the curvature and especially reflectivity of the mirrors have to be matched to the application. We decided to use a

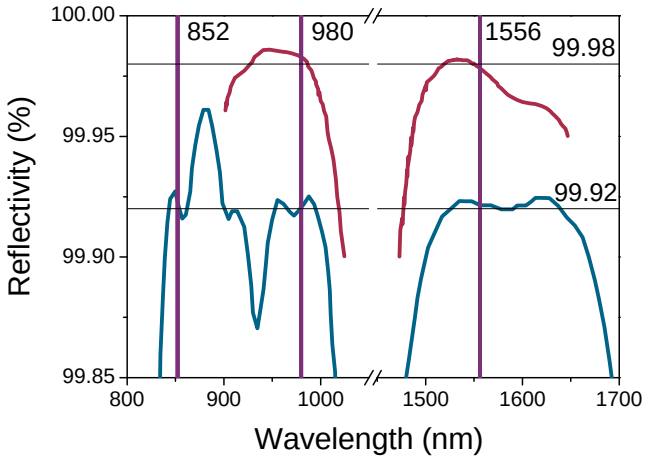

Figure 4.5: Reflectivity of the mirrors used in the Zerodur (blue) and ULE (red) cavity. The purple lines mark the position of the STIRAP wavelengths and the Cs D_2 line at 852 nm.

mirror spacing of $L = 20\,\text{cm}$, which results in an FSR of $\Delta\nu_{\text{FSR}} = 750\,\text{MHz}$. The length is always a trade off between a small FSR and a high stability given by the spacer material. We found that using a scheme where different peaks of the cavity are locked to the Cs transition and using only one AOM with a bandwidth of 50 MHz for each wavelength, a gapless tuning of a laser locked to the cavity would be possible with this FSR. Since we wanted to be able to vary the length of the resonator, a ring piezo was placed between one mirror and the spacer. We used an 8 mm long piezo stack from Noliac. The manufacturer specifies a stroke of 8 μm at 200 V supply voltage. The piezo material usually has a thermal expansion coefficient of $10^{-5} - 10^{-6}/\text{K}$. This means that the length change with temperature of the whole Zerodur spacer is an order of magnitude smaller than that of the piezo. The cavity was placed in a vacuum chamber to isolate it from environmental effects in which it was supported by a stainless steel mount. A schematic of the setup is shown in figure 4.6.

The Zerodur spacer is produced by Hellma Optik. It is 192 mm long and together with an 8 mm long piezo, the mirror spacing is 200 mm. The spacer has a square cross section with an edge length of 30 mm. It has a 10 mm diameter longitudinal hole and a second 'radial' hole to connect the cavity

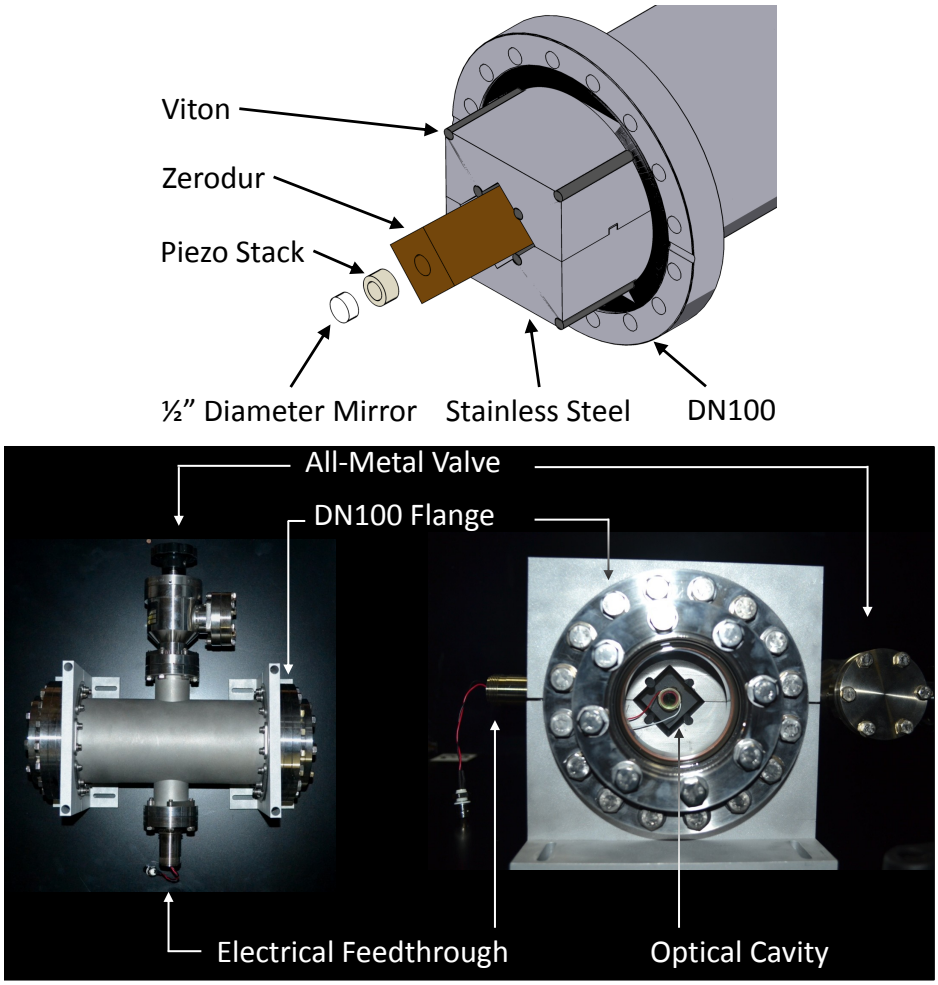

Figure 4.6: The Zerodur spacer is held with a stainless steel mount in the vacuum tube. Viton cord is used to fix the parts in place. The piezo and 1/2-inch diameter mirror are glued to the spacer which has an edge length of 30 mm. The resonator is mounted with an angle of 2° with respect to the vacuum viewports to avoid unwanted etalon effects.

to the outside to allow the evacuation of the cavity.

We decided to use a resonator design with one planar mirror and one mirror with a radius of curvature of 50 cm because a good separation of transverse modes is generated and the planar mirror makes mode matching easier. The planar mirror is glued directly onto the spacer. We used UV curing glue (Norland NOA 61), to be able to correct the position of the mirror until the glue is exposed to UV light. Then the curing process is very fast and the glue is hardened within minutes.

The cavity mirrors have a high reflectivity at three different wavelength ranges at a zero degree angle of incidence at the two STIRAP wavelengths around 980 nm and 1550 nm plus 852 nm to be able to stabilise the cavity length to a Cs transition. We use mirrors from Layertec that are specified to have a reflectivity of 99.92(3) % at 852 nm, 969-989 nm and 1550-1590 nm (see figure 4.5). This results in a finesse of 3900^{+2400}_{-1100} in these ranges from equation (4.13) and a cavity resonance width of ~ 200 kHz.

We wanted the piezo to have a large free stroke so it can compensate for a large temperature drift and still has enough scan range to provide the option to lock to different cavity peaks. A Noliac SCMAR04 H8 piezo with an outer diameter of 15 mm and inner diameter of 9 mm is used. The piezo is glued onto the spacer and the second 1/2-inch diameter mirror is glued to the piezo.

The resonator is mounted in a stainless steel block. This material is used to increase the thermal time constant of the cavity. The parts are placed in a vacuum chamber where the resonator is mounted at an angle of 2° with respect to the vacuum viewports to avoid unwanted etalon effects. The parts are fixed in the vacuum using Viton cord with a diameter of 5.7 mm. The chamber consists of a cross with DN100 diameter and two DN40 flanges perpendicular to the cavity axis. An all-metal valve (MDC AV-150M) and an electrical feedthrough (MDC IFM5-C40) are connected to the smaller flanges and DN63 viewports to the larger ones. The piezo and a thermistor (NJ28, 10kΩ) are connected to the electrical feedthrough. The chamber was evacuated to a pressure of 1×10^{-7} mbar using a pump station combining a rotary pump and a turbo pump. The all-metal valve was closed then to seal the vacuum chamber.

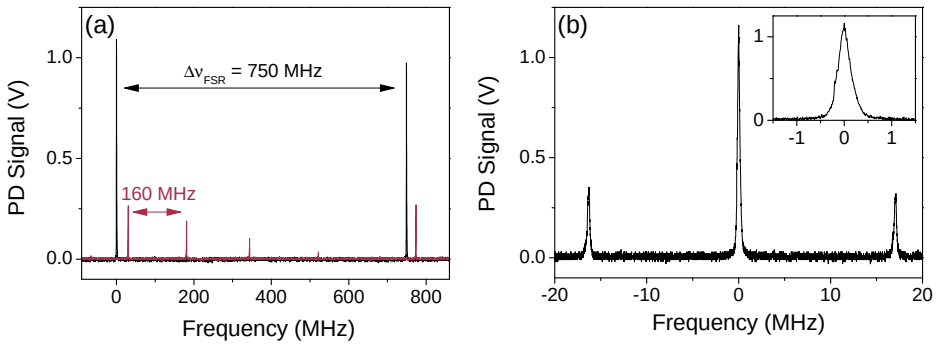

Figure 4.7: Transmission signals of the home-built cavity for 852 nm. (a): The transmission signal for good (black) and bad (red) mode matching. Here, peaks for higher order transverse modes are visible and the frequency spacing agrees with equation (4.7). (b): 16 MHz sidebands were added to calibrate the frequency axis. The inset shows a zoom onto the cavity peak with the same axis assignments as the main plot. A Lorentzian fit to the carrier peak gives a FWHM of 0.27(2) MHz.

Cavity characteristics

In figure 4.7, the transmission signal of the cavity for 852 nm light is shown. In figure 4.7(a), a frequency scan over a whole FSR is presented. For the signal shown in red, the light is coupled into several higher order transverse modes. Their spacing agrees with equation (4.7). The second trace represents the signal for good coupling into the TEM_{00} mode. No higher order modes are visible on this scale; a sign of good mode matching. For figure 4.7(b), an EOM was used to produce sidebands at precisely known frequencies 16 MHz away from the carrier frequency to calibrate the frequency scale on the x-axis. A Lorentzian fit to the carrier peak results in a FWHM of 0.27(2) MHz. Combined with the FSR of $\sim$ 750 MHz, this would give a finesse of $\sim$ 2800 for the cavity which is within the expected range.

However, this technique is not suitable to determine the finesse precisely, since the width of the transmission signal depends on the linewidth of the Toptica DL 100 pro design laser used. Another technique to determine the finesse is to measure the dynamic response of the cavity [167]. To do this, a laser is swept across a cavity resonance and the reflected signal is detected.

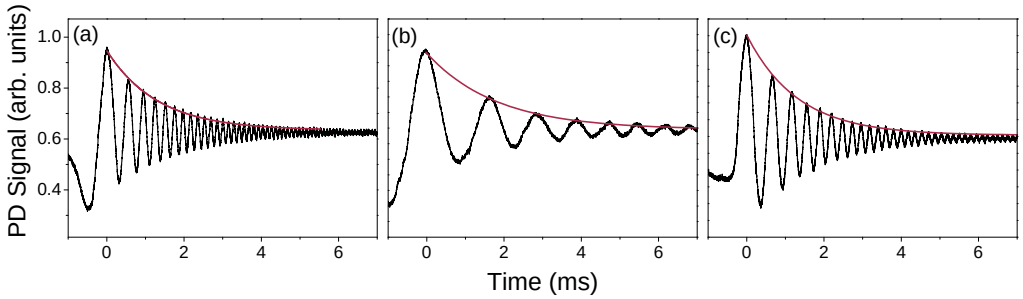

Figure 4.8: Dynamic response signal at (a) 852 nm, (b) 980 nm and (c) 1550 nm. The different oscillation frequencies are due to different scan speeds of the lasers. The results of the measurements are summarised in table 4.2.

Wavelength λ (nm)	Storage time τ_s (μs)	Finesse $\mathcal{F}$
850	1.32(1)	$3.11(2) \times 10^3$
980	1.80(4)	$4.2(1) \times 10^3$
1550	1.32(5)	$3.1(1) \times 10^3$

Table 4.2: Finesse of the home-built cavity for different wavelengths.

This signal is the beat signal between the light coupled out of the cavity after each round trip and the off-resonant light reflected at the first cavity mirror. The cavity decay time τ_s in a high finesse cavity is,

$$\tau_s \approx \frac{2\mathcal{F}L}{\pi c}, \tag{4.15}$$

and hence a direct indicator of the cavity finesse at the laser wavelength. The signals of this measurement are presented in figure 4.8 and the results in table 4.2. The finesses for all wavelengths agree within the quoted error. All values result in a cavity peak width suitable for our application.

We measured how many cavity resonances can be reached at 852 nm by changing the piezo voltage to test if the piezo is working as expected. According to equation (4.2) the light is resonant at a length change corresponding to half the wavelength, which is every 426 nm in this case. The piezo is specified to have a free stroke of 8 μm at 200 V. The piezo driver can provide 150 V, so we expect a total stroke of 6 μm, which means we expect to see 15 cavity modes at 852 nm. Figure 4.9 shows the position of the cavity resonances and the length change of the resonator with respect to the piezo voltage. A linear

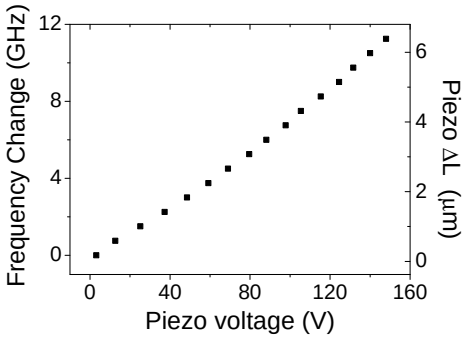

Figure 4.9: Piezo voltage and length change (ΔL) for different longitudinal modes of an 852 nm laser. The change in piezo voltage to shift the cavity resonance frequency by one FSR is recorded. The cavity length changes by 426 nm for each FSR.

fit gives a length change of 43.7(8) nm/V which, when extrapolated to 200 V, results in a total stroke of 8.74 μm and thus a bit more than specified. For the stability of a laser stabilised to the cavity, this means that the noise on the piezo voltage must be below 0.13 mV for laser frequency noise smaller than 10 kHz.

Since a piezo is used in the cavity design, length changes and thus drifts of the peak positions are significant. The 8 mm piezo changes its length by 80 to 800 nm/K, which results in a drift of 141 to 1410 MHz/K. We measured this drift by locking one laser to a Cs transition and another one to a cavity peak. The beat note is recorded together with the room temperature and the temperature inside the cavity vacuum chamber over several hours. The results are presented in figure 4.10(a). The top panel shows that the temperature inside the cavity (black) always lags behind the room temperature (blue) which decreases the total temperature change over a day and filters out the fast temperature changes from the air-conditioning. The temperature changed by $\sim$ 0.5 K in the recorded time window. The cavity drift during this time is shown in the bottom panel of figure 4.10(a) and is $\sim$ 200 MHz. This implies a cavity drift of $\sim$ 400 MHz/K and a thermal expansion coefficient of the piezo material of 3×10^{-5} /K. The resonator length change for a drift of 400 MHz is 227 nm.

To suppress the cavity drift, we stabilise the cavity length to a Cs transition. An 852 nm laser is locked to a cavity resonance which is shifted to

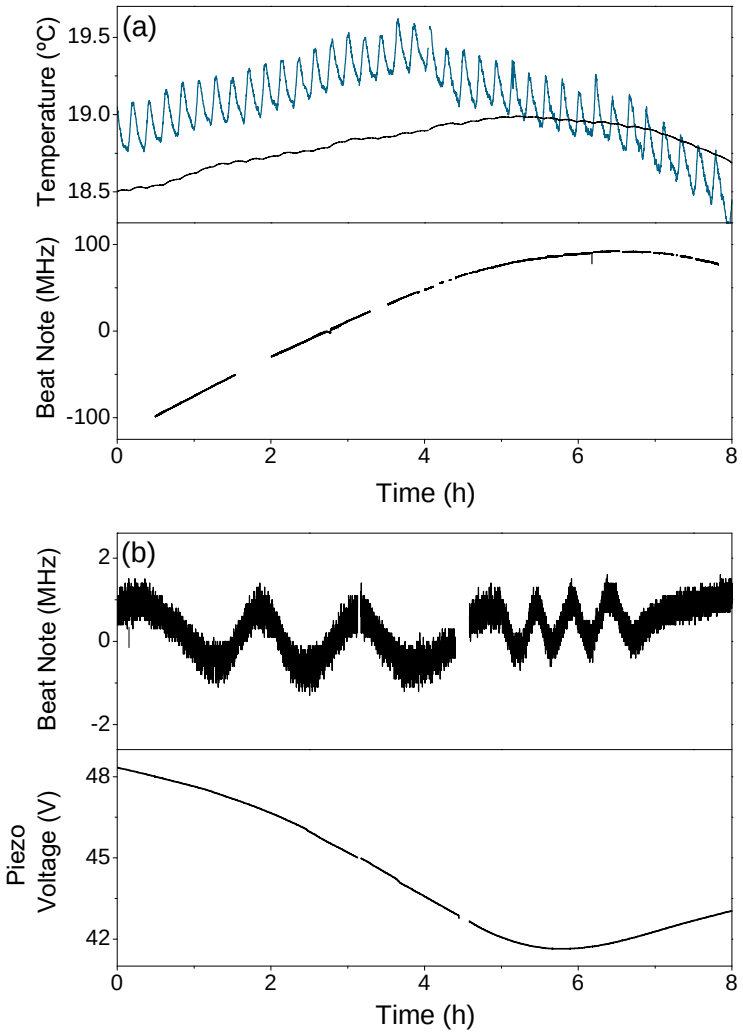

Figure 4.10: Drift of the home-built cavity over 8 hours. (a) Top panel: Room temperature (blue) and the temperature inside the vacuum chamber (black). The fast temperature change from the air-conditioning is filtered out and the maximum temperature is not as high inside the chamber. Bottom panel: Beat note between a laser locked to an atomic transition and one locked to a cavity mode. The laser locked to the cavity drifts $\sim 400\,\mathrm{MHz/K}$. (b) Top panel: Same beat note as in the graph above, but now the cavity length is stabilised by locking a cavity resonance to a Cs transition. The amplitude decreased to $\sim 3\,\mathrm{MHz}$. Bottom panel: Piezo voltage to keep the resonator length stable whilst the cavity is locked.

a Cs transition. An error signal is produced and fed into a PID-controller connected to the piezo driver. This way, a cavity peak position is fixed to the frequency of the Cs transition and thus the cavity length is fixed. A beat note between the laser used to stabilise the cavity and a second laser locked to another Cs transition is taken over the same time interval and during a similar temperature change as the previous measurement. The beat signal is shown in the top panel of figure 4.10(b). The temperature drift over this period of time is suppressed. An oscillation with an amplitude in the range of 2 MHz is left over. The piezo voltage, presented in the bottom panel, was recorded as well. To keep the length of the resonator stable, the piezo voltage changed by 6 V which changes the piezo length by ~ 260 nm. This is in the range we expected from the previous measurement.

Better performance should be attainable by stabilising the temperature of the vacuum chamber, but the potential for noise to be added to the laser frequency by the piezo driver is not negligible. To circumvent these problems and to achieve a better day-to-day reproducibility, we decided to change to a different, passively stable cavity design described in the next section.

4.3.2 Ultra low expansion cavity

To circumvent the problems with length drifts of the cavity and the trade-off in finesse due to the fact that high reflectivity is needed for three wavelengths in the previous resonator, we changed to a new, passively stable design. The spacer of this cavity is made from ULE which is a TiO_2-doped fused silica glass. The unique feature of this material is a zero crossing of the thermal expansion coefficient. The temperature of the zero crossing depends on the amount of titanium dioxide in the glass sample. This can not be predicted precisely due to the production process of ULE in which an inhomogeneous distribution of the TiO_2 is attained [168]. Our cavity spacer and the mirrors were produced and assembled by ATFilms. It was then mounted and housed in a vacuum chamber supplied by Stable Laser Systems. This company also measured the temperature of the zero crossing of the ULE spacer to be 35 °C. This means that our vacuum housing needs to be heated and stabilised to this temperature. The optically contacted mirrors are made out of ULE as

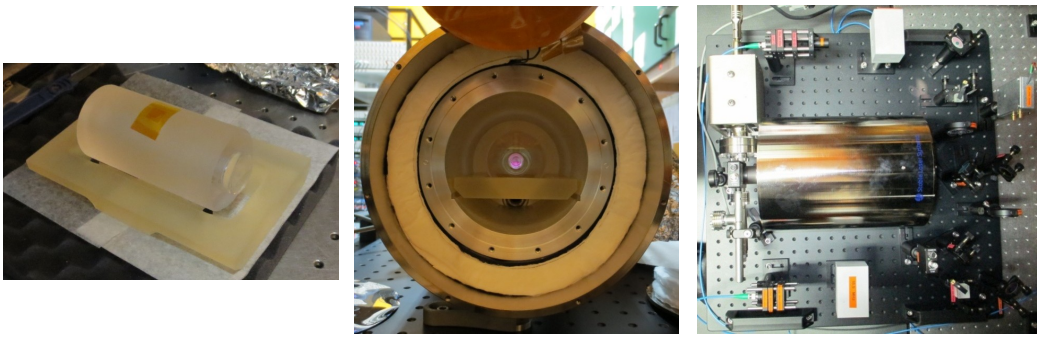

Figure 4.11: Left: The ULE cavity sitting on Viton balls on the Zerodur mount. Centre: The ULE cavity in the vacuum can. Also the temperature insulating material and the heater (bent upwards) can be seen here. Right: The cavity and associated optics are mounted on a breadboard.

well, so the material is not stressed due to different expansions of the spacer and the mirrors [169]. In this design, one planar mirror and one mirror with a radius of curvature of 50 cm is used. The planar mirror makes the design of the mode-matched beams easy, as described in section 4.2.2.

The cavity setup is shown in figure 4.11. The cavity is placed in a vacuum chamber with a Zerodur mount, sitting on Viton balls. The chamber is connected to a 10 l/s ion pump (Gamma Vacuum) which keeps the pressure at $\sim 1 \times 10^{-8}$ mbar. The vacuum chamber is placed in an outer metal can together with two heaters and temperature insulating material. To suppress vibrations, the cavity and associated optics are placed on a 60×60 cm breadboard lying on Sorbothane which sits on the optical table. The breadboard is surrounded by a plywood box, the inside of which is covered with acoustic foam.

Two cavity values are important for the expected locking performance. The width of the cavity peak for the short time locking and the possibility to narrow the linewidth of the laser, and the long term drift of the cavity peaks for reproducibility. The width of the peaks can be calculated when the finesse and the FSR of the cavity is known. To measure the long term drift, the cavity signal has to be compared to another stable signal with known properties.

We determined the finesse using the dynamic response technique as described for the home-built cavity in the previous section. The manufacturer quoted

a finesse of 1.832×10^4 at 980 nm and 1.4×10^4 at 1560 nm from mirror transmission measurements. We measured a finesse of $1.820(5) \times 10^4$ at 980 nm and $1.12(2) \times 10^4$ at 1550 nm. To determine the FSR of the cavity, we added sidebands to the laser using the fibre-coupled EOMs described in section 4.4.3. When the laser is scanned, the positive sideband of one peak overlaps with the negative sideband of the neighbouring cavity peak. This happens for an EOM frequency of 748.36(1) MHz, which results in an FSR of 1496.72(2) MHz. This corresponds to a cavity length of $L = 100.150(2)$ mm. The FSR together with the finesse gives cavity peak linewidths of 82.2(2) kHz at 980 nm and 134(2) kHz at 1550 nm.

For a preliminary test of the cavity drift, we measured its stability with respect to an atomic transition. The $5P_{3/2} - 4D_{3/2}$ and $5P_{3/2} - 4D_{5/2}$ two-photon transitions in ^{87}Rb are at a wavelength of 1529 nm and thus within the high finesse range of the cavity [170]. We locked one laser to the two-photon transition and another one to the cavity. From the beat note of the two lasers on different days, we concluded that the observed drifts of ~ 1 MHz are dominated by the locking instabilities and the cavity drift is well below these drifts.

For a more precise estimate of the drift, we measure the position of a narrow electronically excited state of ^{87}RbCs molecules several times within five months. The position of this resonance was always within a range of 800 kHz with respect to the closest cavity resonance. Since we do not detect a drift in one direction as expected from cavity material ageing, we assume this shift is mainly caused by small changes in the magnetic bias field which superposes the smaller cavity drift. This small long term drift promises a good reproducibility for future experiments using this cavity.

4.4 Laser stabilisation

4.4.1 Introduction

Frequency stabilised lasers are one of the fundamental tools for cold atom experiments. The frequency of a free running diode laser can drift by some

GHz per day due to temperature or current fluctuations or mechanical instabilities. Since laser cooling would not be possible with these drifts, the laser frequency must be stabilised. The lasers used for cooling in our experiment are locked to Rb and Cs transitions using frequency modulation and modulation transfer spectroscopy. This way, the laser drift can be limited to below 1 MHz.

The requirements for STIRAP lasers are different. Generally, there is no nearby atomic transition which can be used to derive an error signal, so these stable reference points have to be produced artificially. Another difference arises from the requirement of a good relative stability between the two STIRAP lasers. A very narrow reference is needed to suppress drifts and use the feedback for linewidth narrowing. A way to produce stable reference points in frequency space is presented in the previous section in the form of an optical resonator. Now the lasers have to be stabilised to the cavity resonances. There are different ways to derive an error signal from a cavity resonance. Some of them lock to the side of a cavity fringe and some to the top of it. In this work, we use the top-of-fringe Pound-Drever-Hall locking technique [171].

4.4.2 Pound-Drever-Hall lock

We use the Pound-Drever-Hall (PDH) technique to derive a dispersive error signal for laser locking from cavity peaks. The advantages of this technique are that a very steep zero crossing is produced where a broad recapture range can be achieved. A modulated laser beam with a carrier frequency ω and sidebands at $\omega \pm \omega_\mathrm{m}$ with opposite phase is incident on an optical cavity. The reflected beam is detected with a photodiode. This signal consists of the beat signal of the carrier with the sidebands. This is mixed with the modulation frequency to produce an error signal at DC. Below, the derivation of the PDH signal based on [172] is presented.

The electric field of a beam, phase modulated with the frequency ω_m is described by

$$E_\mathrm{inc} = E_0 e^{i(\omega t + \beta \sin(\omega_\mathrm{m} t))}, \tag{4.16}$$

where β is the modulation index.

Using the Bessel functions $J_{\mathrm{i}}(\beta)$, this equation can be expanded to

$$E_{\mathrm{inc}} \approx E_0 \left[J_0(\beta) e^{i\omega t} + J_1(\beta) e^{i(\omega+\omega_{\mathrm{m}})t} - J_1(\beta) e^{i(\omega-\omega_{\mathrm{m}})t} \right]. \tag{4.17}$$

This representation is chosen because it highlights the character of the beam, which implies three different frequencies. The carrier with frequency ω and the two sidebands with $\omega \pm \omega_{\mathrm{m}}$. When the power of the incident beam is $P_0 = |E_0|^2$, the power in the carrier is

$$P_{\mathrm{c}} = J_0^2(\beta) P_0, \tag{4.18}$$

and in the sidebands

$$P_{\mathrm{s}} = J_1^2(\beta) P_0. \tag{4.19}$$

For a small modulation depth, nearly all the power is in the carrier and the first-order sidebands. The modulated beam is reflected by the cavity and detected. Now the reflection coefficient can be calculated using equations (4.3), (4.9) and (4.11)

$$F(\omega) = \frac{E_r}{E_i} = r \frac{\exp\left[i \frac{\omega}{\Delta\omega_{\mathrm{FSR}}} \right] - 1}{1 - r^2 e^{i \frac{\omega}{\Delta\omega_{\mathrm{FSR}}}}}, \tag{4.20}$$

and the reflected beam is

$$\begin{aligned} E_{\mathrm{ref}} = E_0 \Big[& F(\omega) J_0(\beta) e^{i\omega t} \\ & + F(\omega+\omega_{\mathrm{m}}) J_1(\beta) e^{i(\omega+\omega_{\mathrm{m}})t} - F(\omega-\omega_{\mathrm{m}}) J_1(\beta) e^{i(\omega-\omega_{\mathrm{m}})t} \Big]. \end{aligned} \tag{4.21}$$

A photodiode detects power $P_{\mathrm{ref}} = |E_{\mathrm{ref}}|^2$, which results in a photodiode signal of

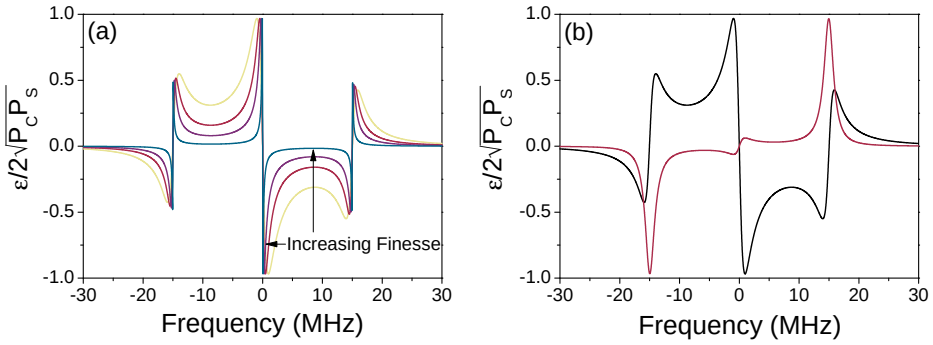

Figure 4.12: Calculated PDH error signal following equation (4.23). (a): Shape of the PDH signal with the modulation $\omega_\mathrm{m} = 15\,\mathrm{MHz}$ and a ratio $\omega_\mathrm{m}/\delta\nu_\mathrm{cav}$ of 15 (yellow), 30 (red), 60 (purple) and 300 (blue). (b): 0° phase shift between the two inputs of the mixer (black) and the signal for a 90° phase shift (red).

$$\begin{aligned} P_\mathrm{ref} &= P_c|F(\omega)|^2 + P_s|F(\omega+\omega_\mathrm{m})|^2 + P_s|F(\omega-\omega_\mathrm{m})|^2 \\ &\quad + 2\sqrt{P_cP_s}\,(\Re\{F(\omega)F^*(\omega+\omega_\mathrm{m}) - F^*(\omega)F(\omega-\omega_\mathrm{m})\}\cos\omega_\mathrm{m}t \\ &\quad + \Im\{F(\omega)F^*(\omega+\omega_\mathrm{m}) - F^*(\omega)F(\omega-\omega_\mathrm{m})\}\sin\omega_\mathrm{m}t) \\ &\quad + (2\omega_\mathrm{m}\text{ terms}). \end{aligned} \tag{4.22}$$

At this point, a frequency mixer is used in the experimental setup. It is used to extract either the $\cos\omega_\mathrm{m}t$ term or the $\sin\omega_\mathrm{m}t$ term. The $2\omega_\mathrm{m}$ terms are blocked by a low-pass filter. For the optimum phase between the mixer's inputs, the error signal is given by

$$\epsilon = -2\sqrt{P_cP_s}\Im\left(F(\omega)F^*(\omega+\omega_\mathrm{m}) - F^*(\omega)F(\omega-\omega_\mathrm{m})\right). \tag{4.23}$$

The simulated error signal for a 15 MHz modulation frequency and different finesses is presented in the left panel of figure 4.12. In the right panel the signal for a cavity peak with a FWHM = 2 MHz and a modulation frequency $\omega_\mathrm{m} = 15\,\mathrm{MHz}$ is presented. The result of equation (4.23) is shown in black. This result is received when the real part is filtered out of equation (4.22), which happens when no phase shift is present between the two inputs of

the frequency mixer. The red trace shows the result for the real part of equation (4.22) which is obtained when there is a 90° phase shift between the mixer inputs. One can see that the black trace gives a good error signal with the recapture range determined by the modulation frequency ω_{m}. The maxima of the centre slope are separated by the FWHM of the cavity peaks. The centre slope D can be written in terms of the Bessel functions of the modulation depth and it reaches a maximum when $P_s/P_c = 0.42$ [172].

4.4.3 Setup

Two Toptica DLpro tunable extended cavity diode lasers are used as a basis for the production of the STIRAP light pulses. The laser used for the transition between the initial Feshbach state and the electronically excited state has a centre wavelength of 1558 nm. The maximum output power is 50 mW and it can be tuned from 1490 to 1580 nm. This gives a wide tuning range to address different vibrational levels of the electronically excited state. The second laser has a centre wavelength of 964 nm with a maximum output power of 80 mW. This laser can be tuned from 909 to 986 nm. The wavelength of both lasers is measured using a Bristol Instruments 621A laser wavelength meter which operates from 520 to 1700 nm. Its absolute accuracy is quoted to be ±60 MHz. We confirmed this by measuring the frequencies of the $5P_{3/2} - 4D_{3/2}$ and $5P_{3/2} - 4D_{5/2}$ two-photon transitions at 1529 nm in ^{87}Rb [170].

The optical setup for the STIRAP laser system is shown in figure 4.13. To produce the light pulses necessary for the STIRAP transfer, each beam passes an 80 MHz AOM from Crystal Technology. The diffraction efficiency is controlled by an Agilent 33500B series waveform generator. With this setup, light pulses as short as 200 ns can be produced. Additionally, shutters are used to block any leakage light from the AOMs into the experiment. The light is then delivered to the experiment using optical fibres.

It is important to reach Rabi frequencies as high as possible during the STIRAP process to reduce the transfer time. The intensity is maximised by matching the beam radius to the FWHM size of the atomic cloud prior to magnetoassociation which is $\sim 40\mu$m. The focussing lens has to be at a

Wavelength (nm)	Direction	w_0 (μm)	z_R (mm)
980	Horizontal	35.3(6)	4.0(2)
	Vertical	36(3)	4.2(7)
1550	Horizontal	37(1)	2.8(2)
	Vertical	40(1)	3.2(2)

Table 4.3: $1/e^2$-radii (w_0) at the beam waists of the STIRAP beams and the resulting Rayleigh ranges z_R.

distance of > 20 cm from the atoms due to the space constraints around the UHV glass cell. A combination of a beam with a radius of 2.62(3) mm and 4.33(2) mm for 980 nm and 1550 nm respectively and an achromatic doublet lens with a focal length of 250 mm leads to the desired tight focus at the position of the molecular cloud. To produce beams with the right diameter, the beams are collimated using 30 mm (980 nm) and 50 mm (1550 nm) achromatic doublet lenses after the light is coupled out of the bare fibres. The resulting beam parameters are presented in table 4.3. The beams then pass a half waveplate to adjust the polarisation before they are overlapped using a dichroic mirror (Thorlabs DMLP1180L).

The alignment of the STIRAP beams was divided into several steps. Due to the higher temperature and larger atom number, the atoms form a larger target than the molecular sample. Hence, for coarse alignment, atoms from the dipole trap were loaded into the 980 nm beam. The centre of the atomic cloud can be found by a fit to the loading efficiency versus beam position. Following this, the 1550 nm beam was overlapped with the 980 nm beam. Fine adjustment was possible after a bound molecular state was found and the 1550 nm laser was resonant with the molecular transition. The focus of the beam was shifted to minimise the lifetime of the molecules during irradiation with resonant light. The results of this measurement are presented in chapter 8.5.

A small amount ($\sim 500\,\mu$W) of the light at each wavelength is used to stabilise the lasers to the cavity. One drawback of a scheme where a laser is locked to the resonance of a cavity is that the locking points are separated by the FSR. Different techniques were developed to bridge these gaps. AOMs

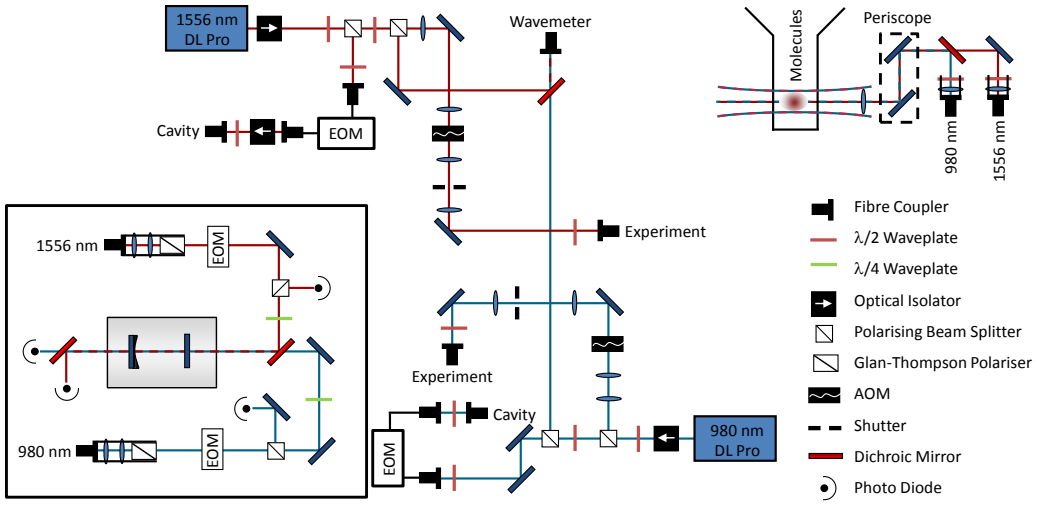

Figure 4.13: Overview of the STIRAP laser system. The light is produced by two Toptica DLpro lasers. Light for locking is sent to the cavity setup with the PDH locking optics via fibre coupled EOMs. The light used for the experiment passes through AOMs to produce the STIRAP pulses before it is coupled into optical fibres. The two beams are overlapped on the experimental table and the beam is focussed to the size of the atomic cloud before magnetoassociation.

can be used to shift the frequency [173], but this technique suffers from low bandwidth of a few 100 MHz. A second laser can be offset phase-locked to a laser stabilised to the cavity [174], but this requires a second laser and adds complexity. We followed the approach to send the laser light through a fibre-coupled EOM and lock the frequency of a sideband to a cavity [175]. The carrier frequency is then tuned by changing the phase modulator frequency with one sideband stabilised to the cavity. The advantage of fibre-coupled EOMs is that they do not need a resonant electric circuit and hence work in a much wider frequency range than free space EOMs. We use phase modulators from Thorlabs (LN65S-FC) and EOSpace (PM-0K5-10-PFA-PFA-980) for 1550 nm and 980 nm, respectively. The EOMs can produce sidebands from DC to 10 GHz and can thus easily be used to bridge the free spectral range of the cavity of 1.5 GHz. Two 1 GHz frequency generators (Agilent E4400B) are used to drive the EOMs.

The light from the fibre coupled EOMs is directed to the optical setup for the PDH lock shown in figure 4.13. In section 4.4.2 we have seen that the error signal is derived from a phase modulated beam which is reflected from

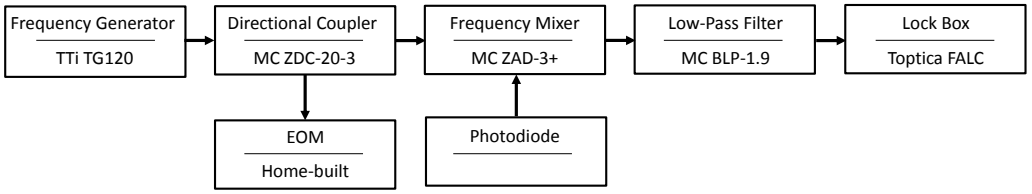

Figure 4.14: Electronic set up to produce the PDH error signal. The signal of a frequency generator is split into two parts using a Mini Circuits (MC) directional coupler. The main part is needed to drive the EOM, which phase modulates the laser beam. +7 dBm of the signal is coupled into a mixer together with the detected reflection signal from the cavity. The resulting signal is sent through a low pass filter to the lock box.

an optical cavity. The cavity we used is described in section 4.3.2 and we use an optical setup described in section 4.2.2 to couple the light into the resonator.

The light is modulated at 10.1 MHz (980 nm) and 13.6 MHz (1556 nm) using home-built EOMs. The EOM design is described in a previous thesis of our group [135]. It uses a 30 mm long lithium niobate ($LiNbO_3$) crystal from DÖHRER Elektrooptik. The crystal is embedded in a simple LCR circuit where it acts as the capacitance. The modulation frequency determines the recapture range of the lock and was chosen due to available electronic devices to produce and process the signal. The modulated beam, reflected from the cavity, is picked up using a quarter waveplate and a polarising beam splitter. A Thorlabs photodiode with a bandwidth of 150 MHz (PDA 10CF-EC) is used to detect the 1550 nm beam. For the 980 nm beam a home-built detector is used. It is based on a Hamamatsu S5971 photodiode and a design presented in [176]. The bandwidth of both photodiodes must be larger than the modulation frequency of the EOMs. A photodiode signal of 11 V/mW (980 nm) and 9.5 V/mW (1550 nm) is produced at the individual wavelengths.

The electronic path to produce and process the locking signal is shown in figure 4.14. The modulation signal is produced with a 20 MHz frequency generator. The 20 $V_{pk\text{-}pk}$ signal is split using a directional coupler. The main output is used to drive the resonant EOM and the coupled output provides a +7 dBm signal for the local oscillator (LO) input of the mixer. The generated frequency and the photodiode signal of the modulated laser beam reflected from the cavity, is fed into a frequency mixer. As we have

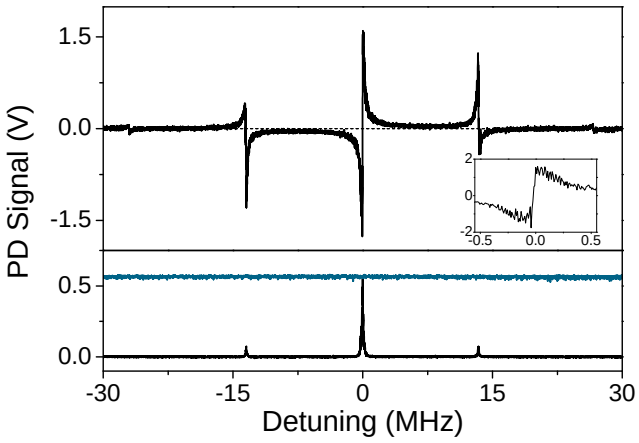

Figure 4.15: PDH error signal (top) and cavity transmission signal (bottom) at 1550 nm. The modulation frequency is $\omega_{\mathrm{m}} = 13.8\,\mathrm{MHz}$. One can clearly see that the outer zero crossings are at the positions of the sidebands. The transmission signal over 20 ms while the laser is locked is shown in blue. The dashed line in the top panel is at zero volts. The inset shows a zoom onto the centre slope which is used for locking with the same axis assignment as the main plot.

seen in the previous section, the phase of the two inputs is important and is adjusted using different cable lengths between the directional coupler and the frequency mixer. The mixer, together with the following low-pass filter, process the signal according to equation (4.22) and (4.23). The error signal at this point is shown in figure 4.15. This signal is fed into a fast analogue linewidth controller (FALC) from Toptica which stabilises the laser to the steep slope in the signal centre at the position of the cavity peak.

4.4.4 Locking performance

The PDH lock is used to both stabilise the laser frequency and to narrow the laser linewidth. We expect a linewidth around 1 kHz for our lasers. To determine how good the laser lock is, we have to measure the linewidth in this range. There are different techniques to do this. One of them is the self-heterodyne method [177]. Here, the beat note of a laser with itself is measured after the beam was split and one part sent through an AOM and the other part delayed by sending it through an optical fibre. The

fibre length must be longer than the expected coherence length of the laser. The coherence length of a 1 kHz laser is ~ 100 km and thus the technique is impractical for such low linewidths. A technique based on the self-heterodyne method where the laser beam is sent several times through the same fibre exists [178]. The problem here is the losses occurring after each round trip, which make it necessary to use a fibre amplifier in the loop. This falsifies the results for low laser linewidth. A different approach is to build a second setup with similar or better properties and beat the lasers against each other. The width of the beat note gives an estimate of the maximum linewidth of both lasers. This technique is cost, time and space-intensive.

Instead, we use two indirect ways to evaluate the performance of the locking setup. First we detect the transmission signal of the cavity. Since we know the shape of cavity transmission peaks from equation (4.12), we can determine frequency drifts by the noise on the transmission signal. We recorded the transmission signal of a locked laser for 20 ms (figure 4.15) and calculated its noise distribution. Comparing this distribution to the width of a transmission peak results in a FWHM of 22(2) kHz of the noise in the locking signal. Since this data is taken over a long time compared to a STIRAP transfer and the noise on the transmission signal is not necessarily frequency noise of the laser, this can only be seen as an upper limit of the linewidth of the laser.

The second technique allows us to improve the performance of a fast lock without knowing the resulting linewidth. A part of the error signal is fed into a spectrum analyser. The signal is extracted with a directional coupler before the mixer. In figure 4.16, the recorded noise spectrum for an unlocked laser, a laser locked to the cavity peak with a slow lock only and a laser locked to the cavity with a fast lock is presented. The frequency at which the system oscillates at high gain (yellow trace in figure 4.16) is an indicator of the locking bandwidth [179].

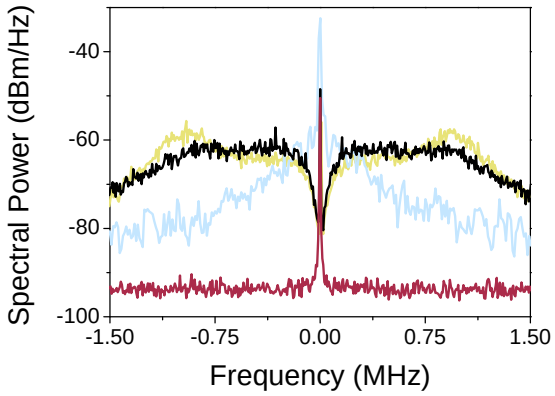

Figure 4.16: The noise spectrum measured at the mixer input of an unlocked laser (red), slow lock (blue), fast lock (black) and fast lock with high gain (yellow). The frequencies are given relative to 13.8 MHz. The peaks at high gain are at 0.97 MHz, which indicates that noise up to this frequency is suppressed, i.e. the servo bandwidth is approximately this wide.

Chapter 5

Interspecies Feshbach spectroscopy of ^{85}RbCs

The following publication resulted out of the work presented in this chapter:

Feshbach spectroscopy of an ultracold mixture of ^{85}Rb and ^{133}Cs
H.-W. Cho, D. J. McCarron, M. P. Köppinger, D. L. Jenkin, K. L. Butler, P. S. Julienne, C. L. Blackley, C. Ruth Le Sueur, J. M. Hutson and S. L. Cornish
Phys. Rev. A **87**, 010703(R) (2013), 10.1103/PhysRevA.87.010703

*We report the observation of interspecies Feshbach resonances in an optically trapped mixture of ^{85}Rb and ^{133}Cs. We measure nine resonances in the lowest spin channel for a magnetic field range from 0 to 700 G and show that they are in good agreement with coupled-channel calculations. The interspecies background scattering length is close to zero over a large range of magnetic fields, permitting the sensitive detection of Feshbach resonances through interspecies thermalisation. Our results confirm the quality of the Rb-Cs potential curves [Phys. Rev. A **85**, 032506 (2012)] and offer promising starting points for the production of ultracold polar molecules.*

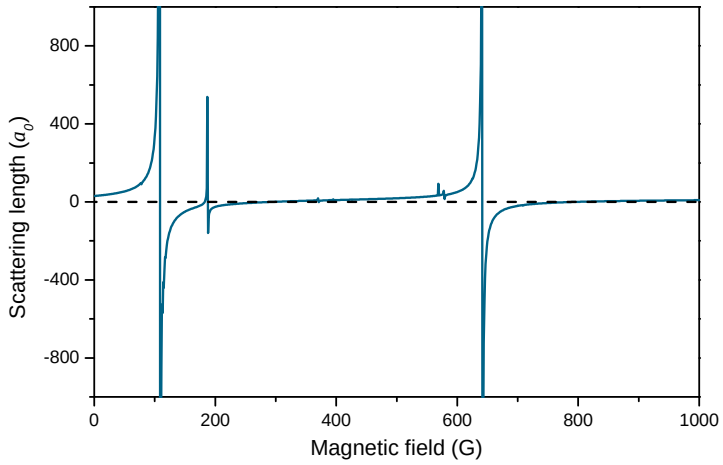

Figure 5.1: Interspecies s-wave scattering length between ^{85}Rb and ^{133}Cs in the $(2, +2)$ and $(3, +3)$ state respectively [180].

5.1 Introduction

Although the experiment was developed to produce ultracold mixtures of ^{87}Rb and ^{133}Cs, it was designed such that only minor changes had to be undertaken to adapt the system to cool ^{85}Rb instead [136]. This opens the door to investigate the interactions of ^{85}Rb and ^{133}Cs, presented in this chapter, and the intraspecies scattering properties of ^{85}Rb, presented in chapter 6. It should be noted that the two mixtures behave in a fundamentally different way, which was not known before the ^{85}Rb–^{133}Cs interactions were investigated during the course of this work.

The 'least-bound-state' of the ^{87}RbCs molecule has a binding energy of $110(20)\,\mathrm{kHz} \times h$ [83], which leads to a high interspecies scattering length between the two constituent species of $+645(60)\,a_0$. Due to this, this mixture suffers from high interspecies three-body recombination loss [158–160]. However, experiments investigating the scattering properties of this mixture [83, 126] resulted in a good model of the interspecies potential [83] that can be used to precisely predict the scattering properties between ^{85}Rb and ^{133}Cs in their absolute internal ground states using coupled-channels calculations. The results for ^{85}Rb in the $(2, +2)$ state and ^{133}Cs in the $(3, +3)$ state are pre-

sented in figure 5.1. We face the interesting situation that the interactions change completely, and instead of a high background scattering length in the ^{87}Rb–^{133}Cs mixture, we are dealing with very small interactions between ^{85}Rb and ^{133}Cs over a wide magnetic field range up to 1000 G. Due to this, an adapted cooling sequence has to be investigated in our experiment since cooling of ^{133}Cs at low temperatures can not rely on sympathetic cooling any more. On the other hand, Feshbach resonances are predicted in this field range which offer the possibility to tune the interactions of the mixture and open the door to magnetoassociation of Feshbach molecules. A total of 32 s-wave resonances were predicted in the field range from 0 to 800 G, eight of them wider than 0.1 G. Note that the definition of a resonance width is complicated due to the small background scattering length of this system. The definition of a calculated width is the difference between the pole and the zero crossing of the scattering length at a Feshbach resonance. In a system with small background scattering length, this definition can lead to very large theoretical width.

5.2 Experiment

The experimental procedure and changes made to the setup for the production of a high PSD mixture of ^{85}Rb and ^{133}Cs is described in a previous PhD thesis from our group [136].

After both species are loaded into the magnetic trap in the $(2, -2)$ (^{85}Rb) and $(3, -3)$ (^{133}Cs) states, forced RF evaporation is applied to cool ^{85}Rb. At this stage, ^{133}Cs is cooled sympathetically by interspecies elastic collisions. At a temperature of 50 μK, when further efficient cooling is prohibited due to Majorana spin flips [157] in the quadrupole trap, the atoms are loaded into the optical dipole trap by lowering the field gradient to 21.2 G/cm, just below 22.4 G/cm, the value required to levitate ^{85}Rb at zero magnetic bias field. At this stage, 4.05 W are used in each dipole trap laser beam. Now the atoms are transferred into their absolute ground state via RF rapid adiabatic passage [66], where two-body loss is suppressed for energetic reasons [152]. At this stage, $2.0(1) \times 10^5$ ^{85}Rb atoms with a temperature of 7.9(1) μK and $2.3(1) \times 10^4$ ^{133}Cs atoms at 10.6(5) μK are confined in the dipole trap. The

trap depth is 53 μK and 71 μK for ^{85}Rb and ^{133}Cs, respectively. We load ~ 10 times more ^{85}Rb than ^{133}Cs into the dipole trap so that the minority species is exposed to a collisional bath of the other species to increase the signature of Feshbach resonances [181]. Evaporative cooling is applied to both species by reducing the beam power to 1.01 W in 2 s, which reduces the trap depth to 14 μK for ^{85}Rb and 19 μK for ^{133}Cs. The trap frequencies at this point are $\omega_{\mathrm{rad}} = 2\pi \times 251\,\mathrm{Hz}$ and $\omega_{\mathrm{ax}} = 2\pi \times 48\,\mathrm{Hz}$ for ^{85}Rb and $\omega_{\mathrm{rad}} = 2\pi \times 235\,\mathrm{Hz}$ and $\omega_{\mathrm{ax}} = 2\pi \times 46\,\mathrm{Hz}$ for ^{133}Cs.

Since the magnetic moment to mass ratio of both species is different, in contrast to an ^{87}Rb–^{133}Cs mixture, different magnetic gradient fields are necessary to levitate both species. To load the dipole trap, a gradient which is slightly too small to levitate ^{85}Rb is applied. This results in a gravitational sag of the ^{133}Cs cloud which is levitated at a gradient field of 31.1 G/cm. We calculated the sag to be $\lesssim 2$ μm, which is significantly less than the full width at half-maximum of the atomic clouds which is $\simeq 24\,\mu$m. This means that the overlap of the clouds is not strongly affected.

In contrast to previous experiments, where Feshbach resonances were detected by loss features induced by an increased three-body recombination rate in the vicinity of a Feshbach resonance [69, 182, 183], the small background scattering length makes another detection method possible. Since the trap is ~ 1.35 times deeper for ^{133}Cs than for ^{85}Rb due to different polarisabilities at 1550 nm, the two gases thermalise to different temperatures after evaporation in the absence of interspecies collisions. If there are elastic collisions between the species, sympathetic cooling can be observed and the two species thermalise to the same temperature. To make use of this property, the whole evaporation process after the spin flip is undertaken at different magnetic bias fields and the atoms are subsequently held in the trap for an additional 1 s. Feshbach resonances are then detected by thermalisation of the two species in their position. Using this method, interactions between the two species can be detected for scattering lengths larger than $60\,a_0$.

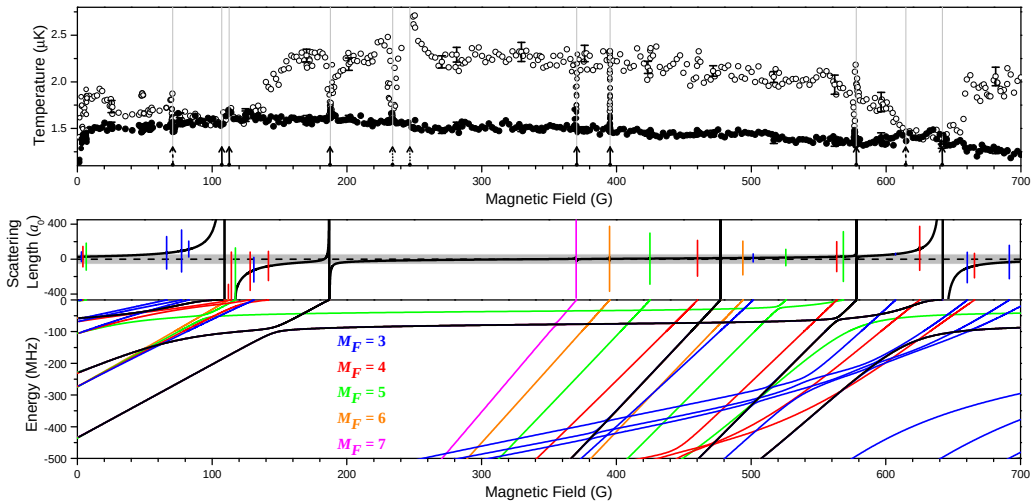

Figure 5.2: Top: Temperature data for a mixture of ^{85}Rb (closed circles) and ^{133}Cs (open circles) in the $(2, +2)$ and $(3, +3)$ state, respectively, evaporated at different magnetic bias fields from 0 to 700 G. The positions of observed Feshbach resonances are marked with arrows, where solid (dashed) arrows mark s-wave (p-wave) resonances. The dotted arrows mark features generated by the dipole trap lasers (see section 5.4). The standard deviation at representative magnetic fields is shown with error bars. Bottom: Interspecies scattering length and molecular states close to threshold. The bound-state energies are plotted relative to the energy of the lowest hyperfine state of ^{85}Rb ^{133}Cs. The black lines mark bound states arising from $L = 0$ (s states). Bound states arising from $L = 2$ (d states) are represented by coloured lines corresponding to their value of M_F. Vertical lines in the scattering length data mark the position of Feshbach resonances and their length is proportional to the logarithm of the width of the resonance. The grey shaded area marks the region where $|a| < 60\,a_0$ and no thermalisation is observed [127].

5.3 Results

We measured the interactions between ^{85}Rb and ^{133}Cs in the (2,+2) and (3,+3) respectively in a field range from 0 to 700 G. The results for a coarse magnetic field scan together with the interspecies scattering length and the bound-state energies obtained from coupled-channel calculations are presented in figure 5.2.

Sympathetic cooling of ^{133}Cs by ^{85}Rb can be observed where $|a| > 60\,a_0$. The range of $|a| < 60\,a_0$ is shaded grey in the panel showing the scattering length. Without interactions, the final ^{85}Rb and ^{133}Cs temperatures after evaporation are 1.50(3) μK and 2.4(1) μK, respectively. The final atom number depends

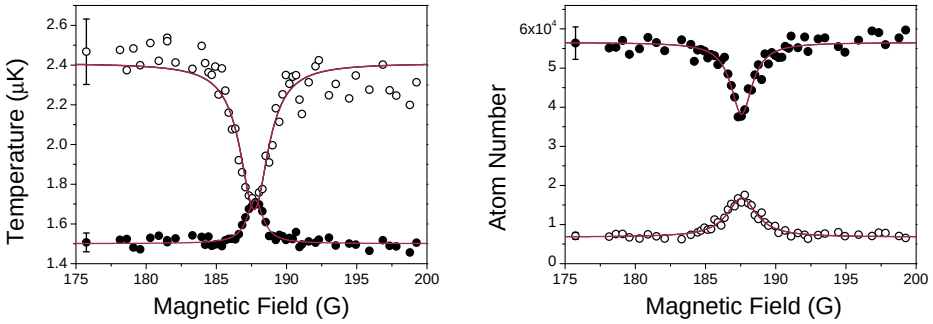

Figure 5.3: ^{85}Rb–Cs interspecies Feshbach resonance at 187.66(5) G. Data for ^{85}Rb (^{133}Cs) is presented in closed (open) circles. Left: In the presence of a Feshbach resonance the interspecies interactions increase and ^{85}Rb cools ^{133}Cs sympathetically during the evaporation process. Right: The cooling process is more efficient for ^{133}Cs when cooled sympathetically. Here atom loss is observed for ^{85}Rb due to an increased heat load on the gas. The standard deviation at a representative magnetic field is shown with error bars.

strongly on the intraspecies scattering properties at the individual magnetic fields.

Figure 5.3 represents the signature of an interspecies Feshbach resonance at 187.66(5) G. In the vicinity of a Feshbach resonance, the interactions between the two species increase and thermalisation can be observed. In this magnetic field range, ^{133}Cs is cooled sympathetically by ^{85}Rb. The final temperature of ^{85}Rb is increased. The additional heat load on ^{85}Rb leads to losses while the sympathetic cooling of ^{133}Cs leads to more atoms remaining in the trap. Lorentzian fits are used to determine the position of each feature. For the final field of the Feshbach resonance, weighted averages of all positions are calculated. In some cases, not all four features were as prominent as in this example. For instance, around the broad Feshbach resonances at 110 G, only the atom number data was useful to determine the position of a resonance (figure 5.4).

When examining the results of this measurement, one has to carefully distinguish between features caused by an intraspecies Feshbach resonance and features caused by interspecies interactions, especially in this mixture, where

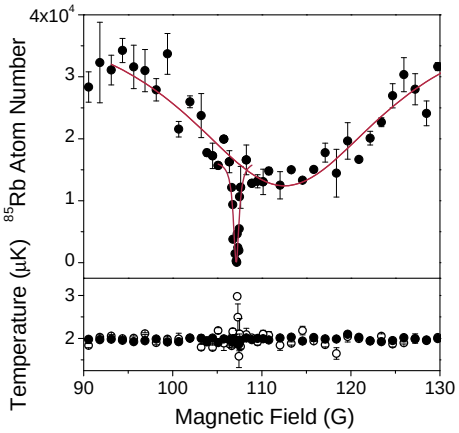

Figure 5.4: ^{85}Rb-Cs Feshbach resonances at 107.13(1) and 112.6(4) G. Data for ^{85}Rb (^{133}Cs) is presented in closed (open) circles. The temperature data presented in the bottom panel can not be used to determine the position of Feshbach resonances in areas with large interspecies scattering length since both species are in thermal equilibrium over a wide magnetic field range. Here only the atom number loss data presented in the top panel is used to determine the position of the Feshbach resonances. The error bars indicate the statistical uncertainties gained from three measurements.

both ^{85}Rb and ^{133}Cs show a rich Feshbach structure in the investigated magnetic field range. Figure 5.5 shows a region where one intraspecies ^{85}Rb and one interspecies resonance exist. A peak in temperature and a drop in atom number for ^{85}Rb exist in both cases, but since no effect on the ^{133}Cs temperature data is detected, the feature at 368.78(3) G can be identified as a ^{85}Rb intraspecies resonance. In contrast to this, thermalisation can be observed at 370.39(1) G through sympathetic cooling.

In table 5.1, all nine experimentally confirmed Feshbach resonances between ^{85}Rb in the (2,+2) and Cs in the (3,+3) state are listed with their individual state assignment. Their positions are in good agreement, with theoretical predictions also shown in the table.

5.4 Dipole trap induced features

In the process of this measurement, two prominent features which were not predicted in theory were observed. They are marked with dotted arrows in

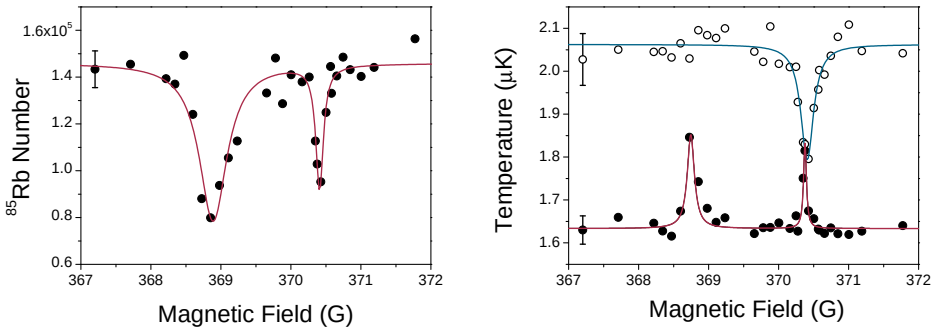

Figure 5.5: ^{85}Rb-Cs interspecies Feshbach resonances at 370.39(1) G and intraspecies ^{85}Rb resonance at 368.78(3) G. Data for ^{85}Rb (^{133}Cs) is presented in closed (open) circles. Left: In the position of both resonances ^{85}Rb atom loss can be observed. Right: The temperature data for both species helps to identify the origin of the features. While thermalisation can be observed at an interspecies resonance, no effect on the Cs temperature is detected in the vicinity of an intraspecies ^{85}Rb Feshbach resonance. The standard deviation at a representative magnetic field is shown with error bars.

figure 5.2 at 233.9(2) G and 246.5(3) G. Additional to the temperature data shown here, large losses were observed at these fields. We found that the features were induced by the dipole trapping lasers. AOMs are used to control the power in the two dipole trap laser beams (see figure 3.1). They detune the beams by 50 MHz in opposite directions to avoid interferences. The frequency can not be changed easily, since fixed frequency drivers are used for the AOMs. Additionally, a polarising beam splitter is used to split the beam derived from one fibre laser, which leads to a perpendicular polarisation between the two beams. This makes it possible to inadvertently drive two-photon transitions.

To test if this happens in this case, we repeated the experiment under different conditions. In figure 5.6(a), a zoom into the data from the coarse scan is presented. The two species thermalised at 233.9(2) G. No reliable temperature data was present for 246.5(3) G due to large atom losses in this field region, which was used to determine the position of this feature. For the data presented in figure 5.6(b), the polarisation of both dipole trap laser beams was rotated by 90° by placing two zero-order $\lambda/2$-waveplates into the beam paths. The two species still thermalised at the same fields and data at

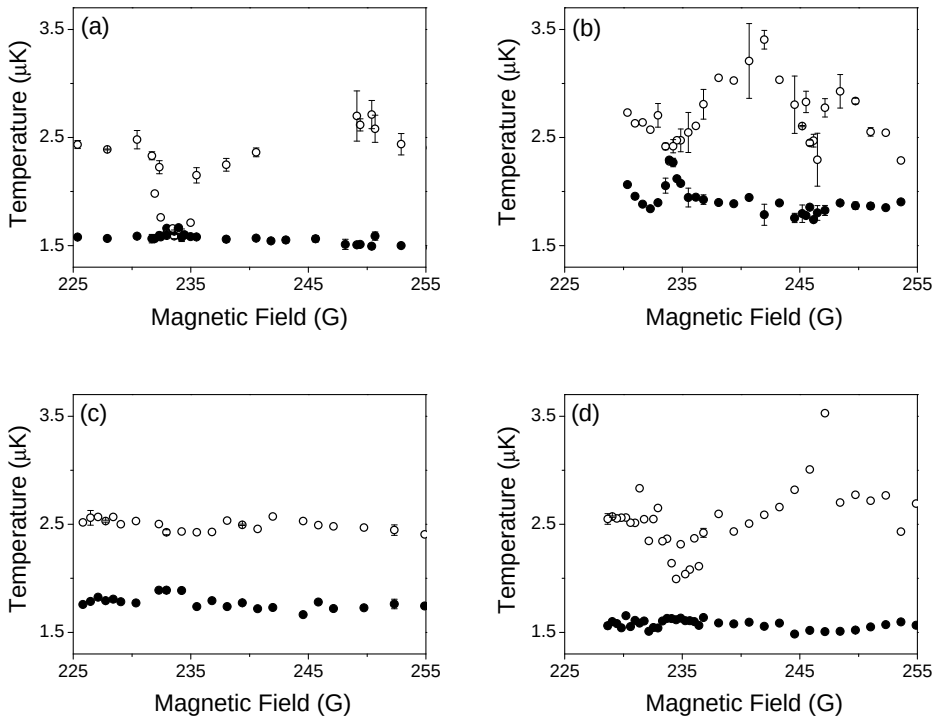

Figure 5.6: Temperature of ^{85}Rb (closed circles) and ^{133}Cs (open circles) in a magnetic field range including the two unpredicted features. The data was taken with (a) perpendicular polarisation of the crossed dipole trap laser beams (normal operating conditions), (b) perpendicular polarisation rotated by 90°, (c) parallel polarisation and (d) parallel polarisation plus a 100 MHz RF magnetic field perpendicular to the quantisation field. The feature can be suppressed using parallel polarisation and recovered by applying a magnetic field modulated at the same frequency as the detuning of the two dipole trap beams.

Experiment		Theory					
		Assignment					
B (G)	ΔB (G)	Inc. Wave	l	f	m_f	B (G)	ΔB (G)
70.68(4)	0.8(1)	p	1	-	-	70.54	-11.62
107.13(1)	0.6(2)	s	0	5	5	109.08	35.0
112.6(4)	28(5)	s	2	6	6	112.21	-0.1711
187.66(5)	1.7(3)	s	0	6	5	187.070	-4.0580
370.39(1)	0.08(4)	s	2	7	7	370.374	3.909
395.20(1)	0.08(1)	s	2	7	6	395.112	0.4488
577.8(1)	1.1(3)	s	0	6	5	578.365	0.3412
614.6(3)	1.1(4)	p	1	-	-	614.984	-6.773
641.8(3)	6(2)	s	0	5	5	642.115	576.5

Table 5.1: Feshbach resonances in a mixture of ^{85}Rb and Cs in their individual absolute ground states. The experimental errors in B_0 and δ are statistical uncertainties resulting from the Lorentzian fits to the loss features. Additional systematic magnetic field uncertainties of ± 0.1 G and ± 0.5 G have to be added for the ranges $0 - 400$ G and $400 - 800$ G, respectively. The theoretical and experimental positions of resonances around 110 G can not be compared since not all resonances in this region have been resolved experimentally.

the 246.5(3) G feature could now be taken since the evaporation process was stopped earlier, resulting in a slightly higher atom number and temperature.

In another experiment, both beams were horizontally polarised. The results in figure 5.6(c) show that the features disappeared for this configuration. The same applies to a configuration where both lasers were polarised in the vertical direction. Subsequently, we applied a 100 MHz RF magnetic field perpendicular to the quantisation axis while the beams were polarised parallel to each other. In this experiment, the features reappeared as the results in figure 5.6(d) show. The measurements together with calculations of the position of bound states in this field region suggest that the features arise from a two-photon Raman coupling to bound or quasibound states of the ^{85}RbCs molecule with $M_F = +4$ or $+6$. The state can not be populated using parallel polarised light due to selection rules and therefore the features disappear under this condition.

5.5 Conclusion

The results presented in this chapter show the fundamentally different interactions between the two species in an ^{85}Rb–Cs mixture compared to an ^{87}Rb–Cs mixture. A background scattering length close to zero over a wide magnetic field range potentially allows efficient cooling of both species without suffering from high interspecies three-body collisions. A phase separation of the two condensed clouds observed in the ^{87}Rb–Cs mixture [160] is not expected in this mixture. This would lead to a better overlap of the clouds at high PSD. The presence of several narrow Feshbach resonances in an easily accessible magnetic field range makes this mixture a good candidate for magnetoassociation. The two wide resonances at 112.6(4) G and 641.8(3) G can be used to precisely control the interactions of the mixture and open the possibility to study Efimov physics in a heteronuclear system [184].

The observed features make this mixture an interesting candidate for future experiments with heteronuclear molecules. However, efficient magnetoassociation is not possible in the apparatus yet because the highest achievable PSD of the mixture is 0.059(4) for ^{85}Rb and 0.041(4) for ^{133}Cs and thus not sufficiently high [185]. To reach a higher PSD and presumably condensation of ^{85}Rb, a new dipole trap setup with larger trapping volume is planned. Here we profit from experiences made with a similar setup in another experiment of our group where quantum degeneracy can be reached with ^{85}Rb atoms [186]. The initial number of atoms trapped in the optical dipole trap there is a factor of two higher. A new dipole trap using a 1070 nm single mode fibre laser with 50 W maximum output power will make it possible to produce a larger trapping volume, benefiting from the larger polarisability of the atoms at this wavelength and the higher output power compared to the current setup. This change will make it possible to produce ^{85}RbCs molecules and explore the molecular states close to threshold presented in the bottom panel of figure 5.2.

Chapter 6

Feshbach spectroscopy of ^{85}Rb

The following publication resulted out of the work presented in this chapter:

Feshbach resonances in ultracold ^{85}Rb
C. L. Blackley, C. Ruth Le Sueur, J. M. Hutson, D. J. McCarron, M. P. Köppinger, H.-W. Cho, D. L. Jenkin and S. L. Cornish
Phys. Rev. A **87**, 033611 (2013), 10.1103/PhysRevA.87.033611

We present 17 experimentally confirmed Feshbach resonances in optically trapped ^{85}Rb. Seven of the resonances are in the ground state channel $(f, m_f) = (2, +2) + (2, +2)$, and nine are in the excited state channel $(2, -2) + (2, -2)$. We find a wide resonance at high field in each of the two channels, offering new possibilities for the formation of larger ^{85}Rb condensates and studies of few-body physics. A detailed coupled-channels analysis is presented to characterize the resonances, and also provides an understanding of the inelastic losses observed in the excited-state channel. In addition we have confirmed the existence of one narrow resonance in a $(2, +2) + (3, +3)$ spin mixture.

6.1 Overview

The scattering properties of ^{87}Rb and ^{85}Rb are vastly different. ^{87}Rb was amongst the first atomic species to be condensed due to its favourable scattering length of about $100\,a_0$ in a very wide accessible magnetic field range. This makes the formation of the BEC possible almost independent of the magnetic bias field. Amongst others, this is a reason why ^{87}Rb is one of the favourite species used in BEC experiments. In contrast, ^{85}Rb has a large negative background scattering length of about $-400\ a_0$. However, it also has Feshbach resonances at easily accessible magnetic fields [187]. The negative background scattering length prohibits condensation, but the possibility to tune the interactions in the vicinity of a wide Feshbach resonance at 155 G makes the formation of a BEC in the $(2, -2)$ state possible [186, 188, 189]. The existence of this resonance makes ^{85}Rb an interesting species where precise tuning of the interactions is desired. For example, for studies of condensate collapse [114, 188, 190, 191], bright matter wave solitons [192] and few-body physics [193]. However, all these experiments were undertaken in the $(2, -2)$ state at fields near the 155 G resonance. The scattering properties at larger bias fields and in the absolute $(2, +2)$ ground state remained unexplored in theory and experiment.

Work on a mixture of ^{85}Rb and ^{133}Cs presented in the previous chapter shows that this combination has promising properties for the production of ultracold molecules. However, a good understanding of the scattering properties of the constituent species is necessary for further work on the mixture. While extensive studies on Cs have been performed [110] and the scattering properties are now well known, the scattering properties for ^{85}Rb still had to be investigated. Additionally, some intraspecies Feshbach resonances were already observed during the course of the work on ^{85}Rb–^{133}Cs.

In this chapter, the results of our studies on the scattering properties of ^{85}Rb in the $(2, -2)$ state and $(2, +2)$ state is presented. A total of 16 Feshbach resonances were located experimentally in a magnetic field up to 1000 G. Additionally, one Feshbach resonance in a $(2, +2) + (3, +3)$ spin mixture was detected.

6.2 Experiment

Since ^{85}Rb and ^{133}Cs do not interact over a wide magnetic field range, the two species can be seen as cooled independently in the mixture experiment scheme presented in the previous chapter. This is why the experimental procedure for cooling ^{85}Rb alone presented here is very similar.

About $6.0(3) \times 10^5$ ^{85}Rb atoms are loaded into the crossed optical dipole trap with 4 W in each beam. The trap is 51 μK deep and has trap frequencies of $\omega_{\mathrm{ax}} = 2\pi \times 95\,\mathrm{Hz}$ and $\omega_{\mathrm{rad}} = 2\pi \times 495\,\mathrm{Hz}$. For different experiments, we either keep the atoms in the $(2, -2)$ state or transfer them into the $(2, +2)$ state via rapid adiabatic passage [66]. When working in the magnetic low-field seeking $(2, -2)$ state, the magnetic gradient field is switched off and the atoms are confined in a pure optical trap. This must be done since the gradient field for our coil configuration adds to the gravitational force instead of cancelling it. Evaporative cooling is then performed by reducing the dipole trap power to 1 W within 2 s and a 1 s hold time at the final trap depth. The whole evaporation process is performed at individual magnetic fields between 0 and 1000 G. The position of a Feshbach resonance is then detected by a change of the atom number in the vicinity of the resonance, since the three-body recombination rate scales with a^4.

6.3 Feshbach resonances in the $(2, -2)$ state

We investigated the scattering properties of ^{85}Rb in the $(2, -2)$ state up to a magnetic bias field of 1000 G. In contrast to interactions in the absolute ground state of the atoms, inelastic scattering can also occur in this excited state. This leads to a complex scattering length [123]

$$a(B) = \alpha(B) - i\beta(B), \tag{6.1}$$

where $\alpha(B)$ corresponds to the real part of the scattering length responsible for elastic collisions and the two-body inelastic loss rate is proportional to $\beta(B)$. When colliding inelastically, the atoms decay into lower magnetic sublevels with $m_f > -2$ and are lost from the trap. Figure 6.1 shows the

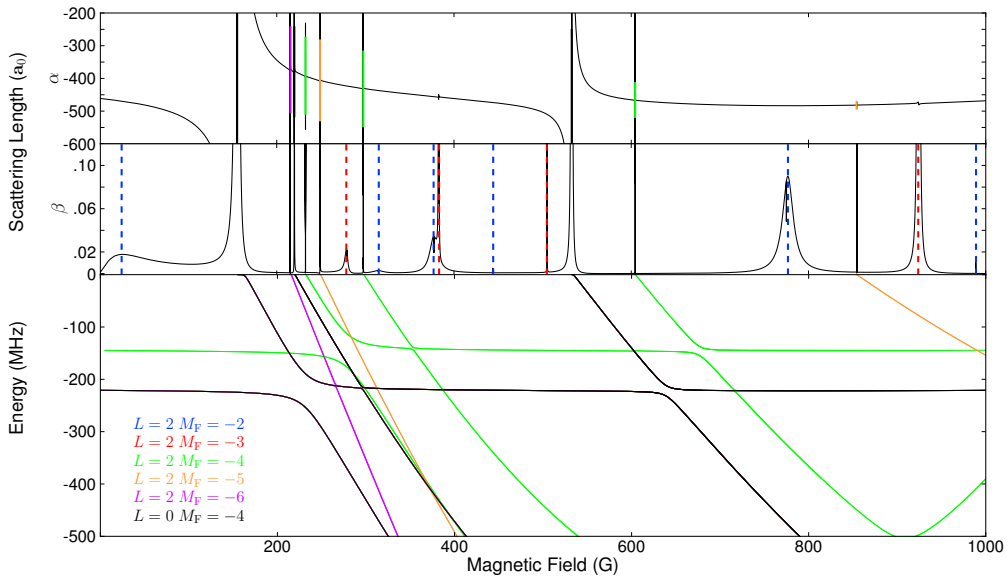

Figure 6.1: Real- (top panel) and imaginary- (centre panel) parts of the s-wave scattering length of ^{85}Rb in the $(2, -2)$ state. Each resonance is indicated by a coloured vertical line that indicates its M_F value (see legend); for pole-like resonances, the length of the line is proportional to the logarithm of the width of the resonance. Dashed lines mark inelastic dominated resonances that are present in the imaginary part β, but do not necessarily show a feature in the real part α of the scattering length. Bottom panel: Molecular states close to threshold. The bound-state energies are plotted relative to the energy of the $(2, -2)$ state of ^{85}Rb. Only states with no continuum interference ($M_F \leq -4$) are shown in the bound-state map, but all resonances are included in the scattering length. All calculations in this figure are for $M_{\text{tot}} = -4$, corresponding to s-wave scattering in the $(2, -2)$ channel.

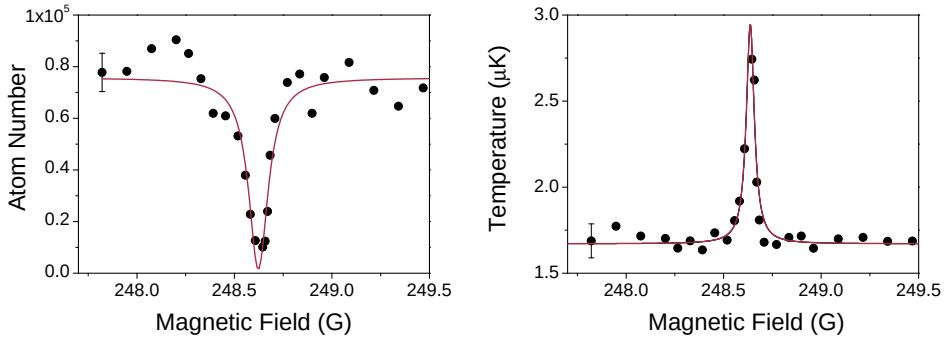

Figure 6.2: A narrow ^{85}Rb Feshbach resonance at 248.64(1) G in the $(2, -2)$ state. Left: Atom loss is observed at a Feshbach resonance due to the increased three-body recombination rate. Right: The temperature is increased in this region due to a decreased evaporation efficiency. The error bars indicate the statistical uncertainties gained from three measurements.

real part (α) and the imaginary part (β) of the scattering length in the top two panels. In order to characterise the Feshbach resonances in an excited state, the resonant scattering length (a_{res}) is defined. It is the ratio of the couplings from the quasibound state the resonance arises from and the incoming inelastic channels [194]. The real part of the scattering length shows an oscillation at an amplitude a_{res} when the background inelastic scattering is small. Similarly, the imaginary part has a peak with height a_{res}. The real and imaginary part of the scattering length show poles at Feshbach resonances arising from bound states with $M_F = -4, -5$ and -6. For all of them, $a_{\mathrm{res}} > 20\,a_0$ and for most of them, $a_{\mathrm{res}} > 1000\,a_0$. The features due to resonances arising from $M_F = -2$ and -3 states have $a_{\mathrm{res}} < 15\,a_0$ and show nearly no feature in the real part, but weak, broad features in the imaginary part of the scattering length.

In figure 6.2, the atom loss signal for a narrow Feshbach resonance is shown. Here a dip in the atom number can be observed due to increased three-body losses. At the same time, the evaporation efficiency decreases, since losses occur predominantly from the coldest atoms in the sample, leading to a peak in the temperature. The final position of a resonance is determined by the weighted average of the position of both features determined by Lorentzian fits. The experimental width of a Feshbach resonance showing such a feature

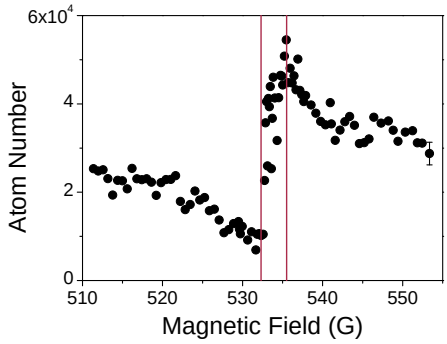

Figure 6.3: A broad ^{85}Rb Feshbach resonance at 532.3(3) G in the $(2, -2)$ state. The feature shows a minimum in atom number at the position of the pole of the Feshbach resonance and a maximum at a scattering length where evaporative cooling is most efficient. The width of such a resonance is determined by the difference in field between the maximum and the minimum.

is determined by the width of the loss feature.

Broad Feshbach resonances show a feature in the atom number with a different shape, presented in figure 6.3. Here a number maximum and a minimum can be observed. The minimum marks the position of the pole in the scattering length and the maximum of the scattering length where evaporative cooling is most efficient. The difference in the field is used to determine an experimental width of these resonances. The definition is not necessarily the same as the calculated width of a resonance, which is the difference in field between the pole and the closest zero crossing of the scattering length. This leads to different experimental and theoretical widths presented in table 6.1 [195].

In figure 6.4, two features dominated by inelastic collisions are presented. In the presence of such a feature, the atoms experience an increasing two-body loss rate and thus a minimum in atom number can be detected. Additionally, the evaporation efficiency decreases and a peak in temperature can be observed. The two examples are the features with the largest calculated values of a_{res}. The rate coefficient, also shown in figure 6.4, for two body losses due to inelastic collisions from a channel n is

$$K_{\mathrm{loss}}^{(2)}(B) = \frac{2h}{\mu} g_n \beta(B), \tag{6.2}$$

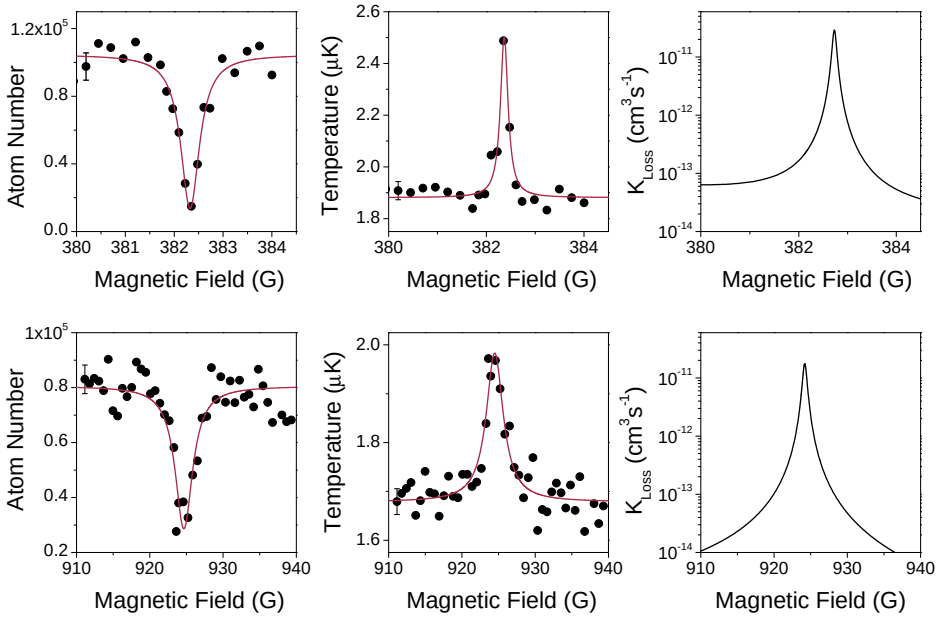

Figure 6.4: Features, dominated by inelastic scattering of ^{85}Rb in the $(2, -2)$ state with the largest calculated values of a_{res} at 382.36(2) G and 924.52(4) G. Left: Atom loss due to increased two-body loss rate in the vicinity of an inelastically dominated feature. Centre: The evaporation efficiency at a loss feature is decreased since the coldest atoms are lost preferably. Right: Rate coefficient for two-body losses due to inelastic collisions.

where $\beta(B)$ is the imaginary part of the scattering length and, for a thermal cloud of identical bosons, $g_n = 2$ [59].

The position, width and assignment of all calculated and of the experimentally confirmed features in ^{85}Rb in the $(2, -2)$ state in a magnetic field range up to 1000 G are summarised in table 6.1.

6.4 Feshbach resonances in the $(2, +2)$ state

A full understanding of the scattering properties of ^{85}Rb in the relevant magnetic field range is necessary for future work on the ^{85}Rb–^{133}Cs mixture. The scattering length in a magnetic field range up to 1000 G was calculated using coupled-channel calculations and is presented in figure 6.5 together with the energy of bound states close to threshold.

Incoming s-wave $(2,-2)+(2,-2)$ state							
Experiment		Theory					
B_0	δ	Assignment		B_0	Δ	$a_{\rm res}$	$a_{\rm bg}$
(G)	(G)	L	M_F	(G)	(mG)	(a_0)	(a_0)
156(1)	10.5(5)	0	-4	155.3	10900	$\geq$10000	-441
-	-	2	-6	215.5	5.5	4000	-374
219.58(1)	0.22(9)	0	-4	219.9	9.1	4000	-379
232.25(1)	0.23(1)	2	-4	232.5	2.0	400	-393
248.64(1)	0.12(2)	2	-5	248.9	2.9	5000	-406
297.42(1)	0.09(1)	2	-4	297.7	1.8	5000	-432
382.36(2)	0.19(1)	2	-3	382	-	15	-457
532.3(3)	3.2(1)†	0	-4	532.9	2300	$\geq$10000	-474
604.1(1)	0.2(1)	2	-4	604.4	0.03	700	-466
-	-	2	-5	854.3	0.002	25	-481
924.52(4)	2.8(1)	2	-3	924	-	9	-476

Table 6.1: Position and assignment of Feshbach resonances for $^{85}Rb_2$ in the $(2,-2)$ channel in the field range between 0 and 1000 G. All resonances shown satisfy $a_{\rm res} \geq 1\ a_0$. The quantum numbers indicate the molecular states. Experimental errors are uncertainties in the position and width determined from the Lorentzian fits. Broad resonances, where the experimental width is determined between the minima and maxima in the atom number, are labelled with †. Additional systematic uncertainties of 0.1 G and 0.5 G apply to resonance positions in the field ranges 0 to 400 G and 400 to 1000 G respectively. The resonances near 155 G and 220 G have been measured previously [196, 197].

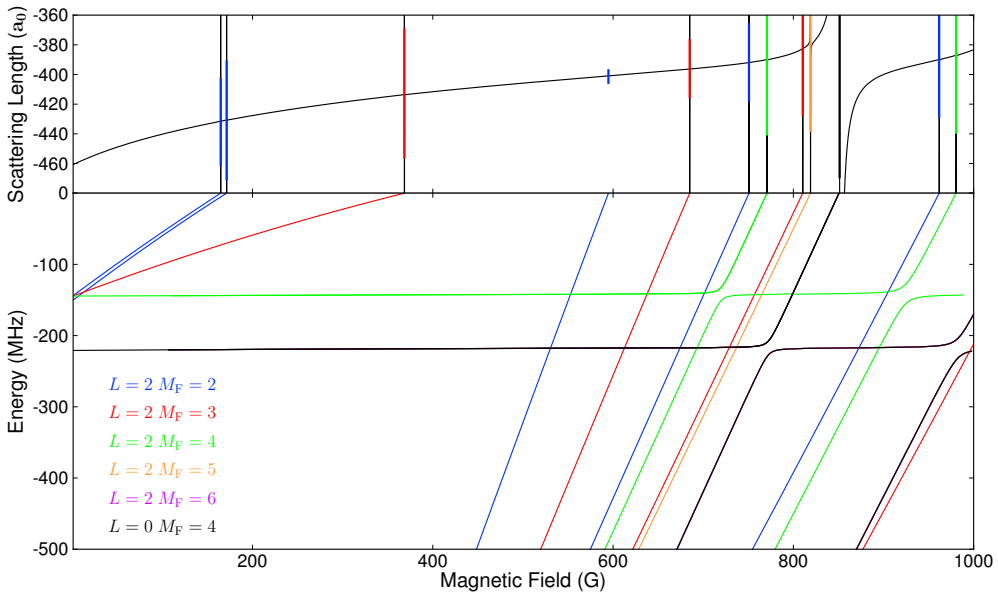

Figure 6.5: Top panel: ^{85}Rb s-wave scattering length in the $(2, +2)$ state. Bottom panel: Binding energy of weakly bound molecules with respect to the energy of the free atoms in the $(2, +2)$ state. Feshbach resonances are marked with lines and their different colours indicate their value of M_F (see legend). Their length is proportional to the logarithm of the width of the resonance. All calculations in this figure are for $M_{\text{tot}} = 4$, corresponding to s-wave scattering in the $(2, +2)$ channel [123].

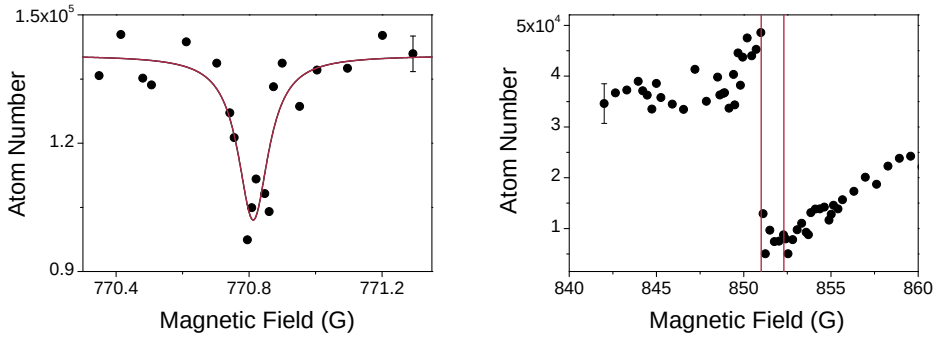

Figure 6.6: ^{85}Rb Feshbach resonances at 770.81(1) G and 852.3(3) G in the $(2, +2)$ state.

The scattering length is negative in this field range and affected by the broad Feshbach resonance in the $(2, -2)$ state at 155 G. Interestingly, in addition to several narrow features, the scattering length shows a broad Feshbach resonance at 851.3 G. Here the scattering length is positive between 850.1 G and the position of the pole. This feature opens the possibility to produce a ^{85}Rb BEC in the absolute ground state in future experiments. The atom loss feature observed at the position of this resonance is presented in figure 6.6 together with the loss feature of a narrow Feshbach resonance at 770.81(1) G. The features show the same properties for broad and narrow resonances as described in the previous section. The calculated and measured results of Feshbach resonances in the $(2, +2)$ state are summarised in table 6.2.

6.5 Feshbach resonances in a spin mixture

Additionally to the calculations for the two previous states, the scattering length between different spin states of ^{85}Rb was studied. The scattering length was calculated between atoms in the $(2, +2)$ state and the $(3, 0... + 3)$ states and atoms in the $(2, -2)$ state and the $(3, 0... - 3)$ states. Feshbach resonances are predicted for all spin mixtures. We have measured the position of one Feshbach resonance in a spin mixture of ^{85}Rb in the $(2, +2) + (3, +3)$ states. For this measurement, the atoms were first cooled in the dipole trap according to the experimental sequence for a measurement in the $(2, +2)$

Incoming s-wave $(2,+2)+(2,+2)$ state								
Experiment		Theory						
B_0	δ	Assignment				B_0	Δ	a_{bg}
(G)	(G)	L	(f_a,f_b)	F	M_F	(G)	(mG)	(a_0)
164.74(1)	0.08(2)	2	(2,2)	4	2	164.7	-0.0006	-432
171.36(1)	0.12(2)	2	(2,2)	2	2	171.3	-0.02	-431
368.78(4)	0.4(1)	2	(2,2)	4	3	368.5	-0.06	-413
-	-	2	(2,3)	3	2	594.9	-0.4×10^{-6}	-401
-	-	2	(2,3)	5	3	685.0	-0.4×10^{-4}	-396
-	-	2	(2,3)	5	2	750.8	-0.0003	-392
770.81(1)	0.11(2)	2	(2,3)	5	4	770.7	-0.5	-390
809.65(3)	0.3(1)	2	(2,3)	3	3	809.7	-0.09	-383
819.8(2)	0.7(5)	2	(2,3)	5	5	819.0	-5.4	-380
852.3(3)	1.3(4)†	0	(2,3)	5	4	851.3	-1199	-393
-	-	2	(2,3)	2	2	961.8	-0.01	-390
-	-	2	(2,3)	4	4	980.5	-0.7	-387

Table 6.2: Position and assignment of Feshbach resonances for $^{85}Rb_2$ in the $(2,+2)$ channel in the field range between 0 and 1000 G. The quantum numbers indicate the molecular states. Experimental errors are uncertainties in the position and width determined from the Lorentzian fits. Broad resonances, where the experimental width is determined between the minima and maxima in the atom number, are labelled with †. Additional systematic uncertainties of 0.1 G and 0.5 G apply to resonance positions in the field ranges 0 to 400 G and 400 to 1000 G respectively.

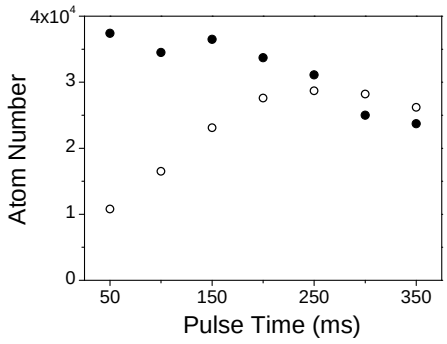

Figure 6.7: Number of ^{85}Rb atoms in the (2,+2) state (closed circles) and in the (3,+3) state (open circles) versus microwave pulse time. A 250 ms pulse with a frequency of 3088.78 MHz is used to produce a mixture with equal number in each state. Stern-Gerlach separation is used to image atoms in each species.

state. After the evaporation sequence, a 3088.78 MHz microwave pulse at a bias field of 22.6 G is used to populate the $(3, +3)$ state. Before imaging, atoms in the two states are separated using the Stern-Gerlach technique.

Figure 6.7 shows the dependency of the population distribution on the pulse length. Initially, all atoms are in the $(2, +2)$ state and after $\sim$ 250 ms, a mixture containing up to $7(1) \times 10^4$ atoms in each spin state can be produced by increasing the atom number loaded into the MOT.

When measuring this Feshbach resonance, one must be careful, since resonances in the $(2, +2)$ state at 810.2 G and 818.8 G are close to the predicted position of this resonance of 816.9 G. The loss feature measured in the atom number of ^{85}Rb atoms in the $(2, +2)$ state is shown in figure 6.8. A position of 817.45(5) G and a width of 0.031(1) G are determined from a Lorentzian fit. To test if the feature originates from scattering of atoms in different spin states, the experiment was repeated without applying the microwave pulse to populate the $(3, +3)$ state. In this experiment, with all atoms in the $(2, +2)$ state, the feature disappeared, confirming that the feature arises from scattering between particles in the different spin states.

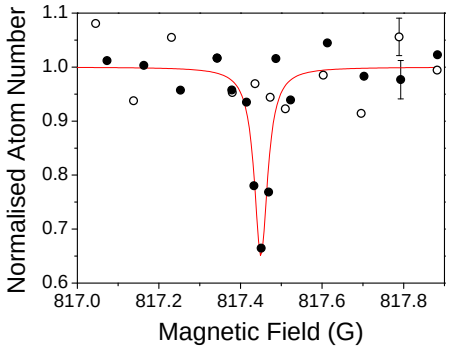

Figure 6.8: ^{85}Rb Feshbach resonance between ^{85}Rb atoms in the $(2, +2)$ and $(3, +3)$ spin states at 817.45(5) G. A loss feature in the atom number in the $(2, +2)$ state is detected in a mixture with an equal number of atoms in the $(2, +2)$ and $(3, +3)$ state (closed circles). The loss feature is not visible in a sample prepared purely in the $(2, +2)$ state (open circles).

6.6 Conclusion

Previous work with ^{85}Rb has focussed on a broad Feshbach resonance at 155 G in the $(2, -2)$ state, which makes it possible to precisely tune the interactions. This has led to the production of a BEC [186, 188, 189], bright matter wave solitons [192] and studies of few-body physics [193]. Only one other resonance at a slightly higher field (219.9 G) in this state was also observed previously [197].

We explored the scattering properties of ^{85}Rb in the $(2, -2)$ state to a magnetic field range up to 1000 G and expanded the investigation to the $(2, +2)$ absolute ground state in the same field range. In addition to numerous narrow resonances, broad resonances were found in both states. Interestingly, a broad resonance at 851 G in the $(2, +2)$ state offers the possibility to tune the scattering length to a positive value, making evaporative cooling without two-body loss possible and offering the prospect of BEC formation in the absolute internal ground state. Insight gained from this work will help to produce a high PSD sample of ^{85}Rb which is essential for further work on the ^{85}Rb–Cs mixture and the production of molecules. Furthermore, work is underway on the construction of a new dipole trap with a larger beam waist to produce larger samples of ultracold ^{85}Rb and reach a higher PSD.

Chapter 7

Creation of ultracold Cs_2 molecules

7.1 Overview

An important milestone on the way to the production of ultracold polar ground state molecules is the association of Feshbach molecules from ultracold atoms. Although the final goal is to produce dimers from ^{87}Rb and ^{133}Cs, we first tested the association ramp sequence with Cs_2, where there is a substantial body of published work [73, 110, 198]. The bound state spectrum just below threshold is the subject of much current research [110, 116, 199, 200]. The Cs_2 Feshbach molecules have been transferred into a metastable state above the dissociation threshold [201] and the collisions between dimers [202–204] and between dimers and atoms [205] have been investigated. Cs_2 molecules were also the first ultracold molecules transferred to a deeply bound ground state after magnetoassociation using STIRAP [91].

Producing dimers from a single species circumvents some problems one has to face when working with a two species mixture. One advantage is that the overlap of the constituent atoms does not have to be taken into account, since the molecules are formed from one atomic cloud. Another advantage concerns the imaging. The number of molecules is usually relatively small, in the range of 10^4. After dissociation of a homonuclear dimer, double the number of atoms are imaged, which increases the OD and the minimum number of

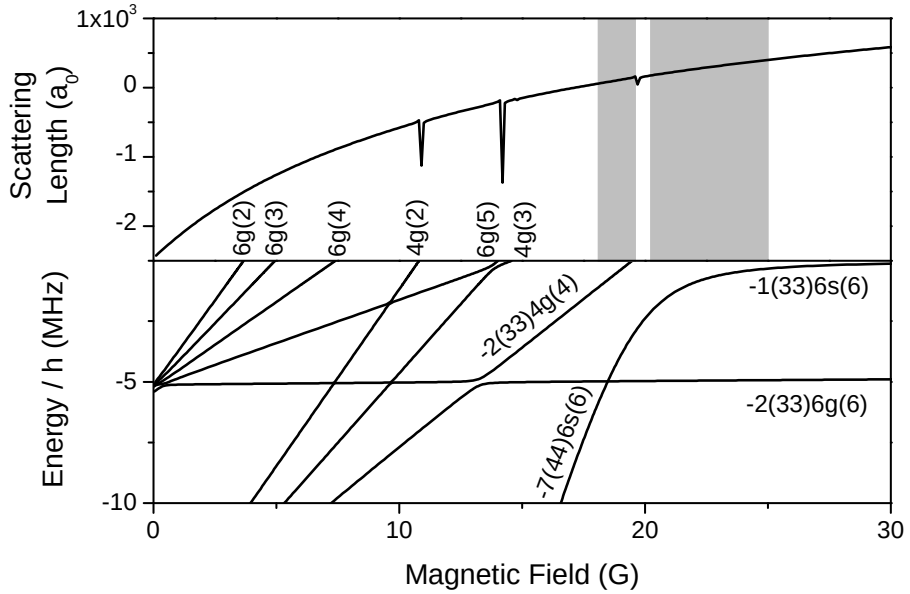

Figure 7.1: Top panel: Cs scattering length. The grey areas mark the magnetic fields where the creation of Cs Bose-Einstein condensates is possible in the experiment. Bottom panel: Cs bound state energies for weakly bound states. The notation is $n(f_1 f_2)FL(M_F)$ [206].

molecules that can be detected compared to a heteronuclear molecule.

Figure 7.1 shows the scattering length of Cs in the high-field seeking $(3, +3)$ state and the bound state spectrum just below threshold for a magnetic field up to 30 G. Most of the previously mentioned experiments were undertaken in this field range. The set of quantum numbers used for the near-threshold levels is $n(f_1 f_2)FL(M_F)$, where n is the vibrational level counted from the least bound state, f_i are the zero-field levels of the Cs atoms, F is the resultant of the f_i, L is the partial-wave angular momentum and $M_F = m_1 + m_2$ following [110]. In the rest of this chapter, an abbreviation of the assignment to $FL(M_F)$ is used.

For magnetoassociation, the Feshbach resonance arising from the $4g(4)$ molecular state at ~ 19.9 G is used. This resonance lies in an easily accessible field range and it couples directly into a high-field seeking state which can be levitated against gravity with the implemented coil configuration. This makes further experiments with the molecules possible without changing the

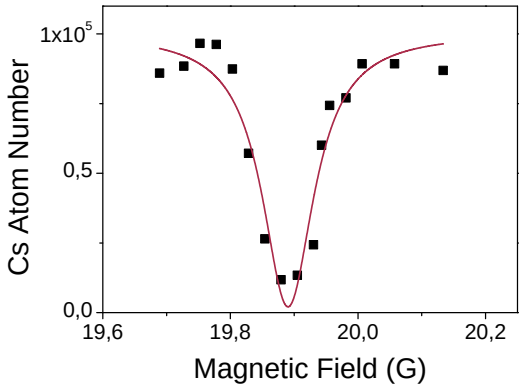

Figure 7.2: Cs Feshbach resonance at 19.89(2) G which is used to associate Cs_2 molecules. The position and width of 0.10(2) G are determined by a Lorentzian fit to the loss feature.

trap parameters significantly. Additionally, cooling of Cs atoms is efficient in a range of magnetic fields around the Feshbach resonance. The production of a Cs BEC in our experiment is possible in the two grey shaded field ranges in figure 7.1, from 18.1 to 19.6 G and from 20.2 to 25 G separated by the Feshbach resonance used for magnetoassociation [207].

7.2 Association of Cs_2 molecules

The starting point for the magnetoassociation of Cs_2 molecules is the production of a Cs BEC, the full details of which can be found in previous publications from our group [135, 136, 160]. Cs is loaded into the optical dipole trap with 6 W per beam, which results in a trap depth of $\sim$100 μK. Before the evaporation, $2.4(3) \times 10^6$ Cs atoms are trapped in the $(3, +3)$ state with a temperature of 15.04(4) μK and a PSD of $1.03(2) \times 10^{-3}$. Evaporation is achieved by decreasing the dipole trap power over 5.55 s to 55 mW, corresponding to a final trap depth of 0.9 μK. The atom number after evaporation is $2.79(4) \times 10^5$ and the PSD 0.26(1) at a temperature of 0.26(1) μK. At this point, a magnetic field gradient is applied to tilt the trapping potential. This reduces the trap depth with little effect on the trap frequencies [207, 208]. Using this technique, a Cs BEC with $\sim 1 \times 10^5$ atoms can be produced. In the molecule production sequence, we usually stop the evaporation before a BEC is formed.

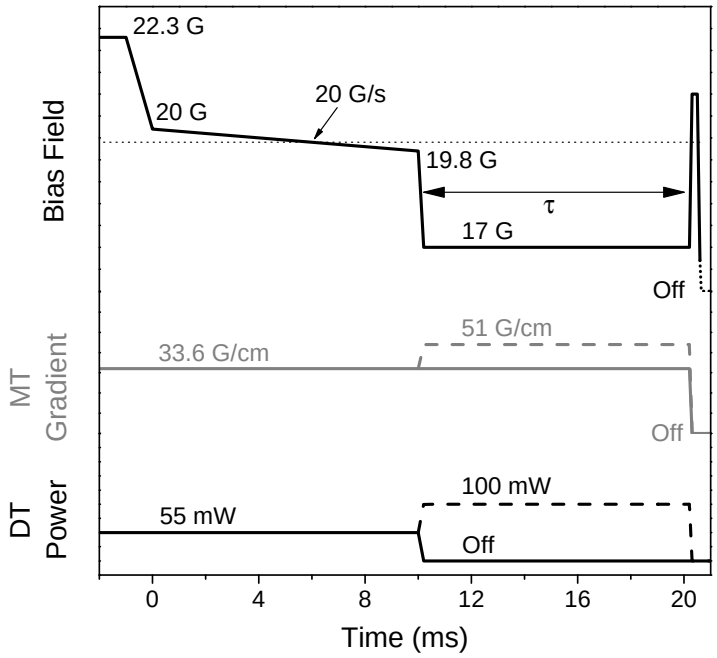

Figure 7.3: Cs_2 molecules association sequence. The dashed lines show the sequence for trapping of Cs_2 molecules in the optical dipole trap. The dotted line illustrates the position of the Feshbach resonance. The hold time, τ, in the dipole trap is varied to measure the lifetime of the molecules.

Before the molecules are associated, the Feshbach resonance has to be located according to the techniques presented in chapters 5 and 6. After an ultracold sample is produced, the atoms are exposed to different magnetic fields for 500 ms. The three-body recombination rate scales with a^4, leading to enhanced loss at the pole of a Feshbach resonance. The loss feature of the resonance we use for association is presented in figure 7.2. A Lorentzian fit results in a position of 19.89(2) G and a width of 0.10(2) G.

The experimental sequence after evaporation is presented in figure 7.3. The magnetic field is decreased to a field just above the Feshbach resonance. The molecules are associated during a 200 mG ramp in 10 ms across the resonance. After the association, the dimers are in the $4g(4)$-state illustrated in figure 7.1. A ramp to 17 G binds the molecules by 2 MHz$\times h$. They have a magnetic moment of $-0.9\,\mu_B$, which corresponds to a levitation gradient of 52 G/cm compared to 31 G/cm for the Cs atoms. This means the molecules are under-levitated and fall down when the dipole trap is switched off while

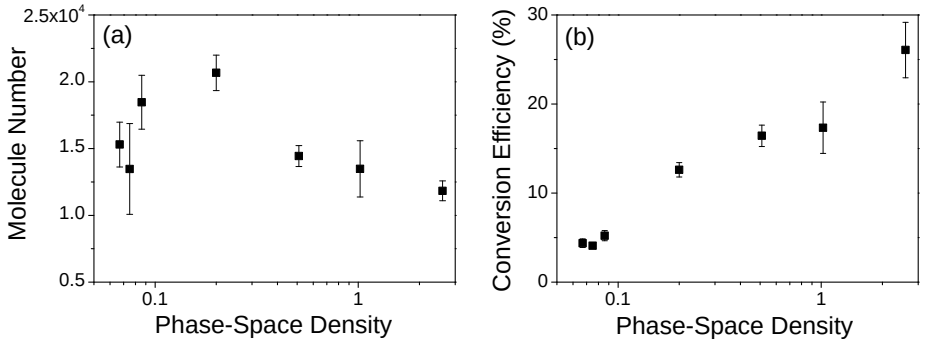

Figure 7.4: Molecule number (a) and Cs atoms to molecules conversion efficiency (b) versus PSD of the atomic sample before the association ramp. The maximum molecule number is $2.1(1) \times 10^4$ and the maximum conversion efficiency 26(3) %. The error bars indicate the statistical uncertainties gained from three measurements.

the atoms remain levitated. This Stern-Gerlach separation is used to isolate the two components. Since we can not image the molecules directly, the magnetic field is swept across the Feshbach resonance in the opposite direction to dissociate the molecules again and detect the atoms using resonant absorption imaging.

The absolute molecule number and conversion efficiency depends on the PSD of the atomic sample before association [185] and is presented in figure 7.4. Here, the conversion efficiency is defined by $2N_{\mathrm{mol}}/N_{\mathrm{Cs\ initial}}$. The maximum molecule number is $2.1(1) \times 10^4$ coupled out of a sample of $3.28(2) \times 10^5$ Cs atoms with a PSD of 0.20(1). The highest conversion efficiency, 26(2) %, is observed when the molecules are coupled out of a BEC.

For further experiments, it can be advantageous to keep the molecules confined in the optical dipole trap. We achieve this by small changes in the experimental sequence visualised with dashed lines in figure 7.3. After the association ramp, the power of the dipole trap beams is increased to 100 mW and the field gradient increased to 51 G/cm. At this value, the molecules are levitated and the atoms are pushed upwards out of the trap. Figure 7.5 shows the trapping time of Cs_2 molecules. The bottom panel shows the horizontal width of the sample. The open circles show the expansion of an untrapped sample and the closed squares show the width of the cloud with the dipole

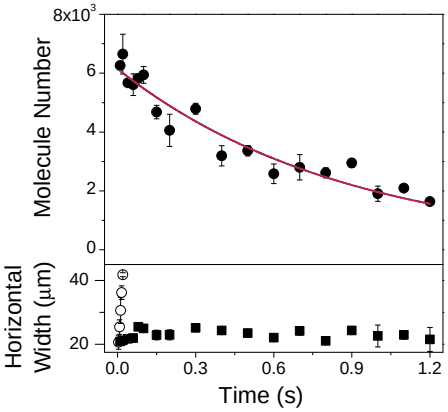

Figure 7.5: Top panel: Cs_2 molecule number in the 100 mW dipole trap. The lifetime is 0.88(8) s. The bottom panel shows the horizontal width of the cloud with (filled squares) and without (open circles) the dipole trap beams.

trap on. The constant width is an indicator that the sample is trapped.

7.3 Controlling the molecular state

Once Feshbach molecules are produced, they are coupled into the specific state that the Feshbach resonance arises from. In the bound-state spectrum, shown in figure 7.1, one can see that avoided level crossings between different molecular states exist. These can be used for internal state transfer of the molecules by changing the magnetic bias field [116]. When the magnetic field is ramped slowly, the population is transferred adiabatically into another state. A fast ramp has no effect on the molecules and they remain in their initial state (see equation (2.19)).

The first avoided crossing of the $4g(4)$-state is with the $6g(6)$-state around 13.5 G. The coupling strength between the two states is $V \cong h\times 150\,\mathrm{kHz}$ [202], which results in a critical ramp speed $\dot{r}_\mathrm{c} \sim 1100\,\mathrm{G/ms}$. The $6g(6)$-state has a magnetic moment of $-1.5\,\mu_\mathrm{B}$ and thus the levitation gradient is 31 G/cm.

The difference in magnetic moment of the two states involved in this avoided crossing gives us the chance to apply a magnetic field gradient that over-levitates one state and under-levitates the other one. Combined with the fact that the atoms experience a different bias field as a function of position

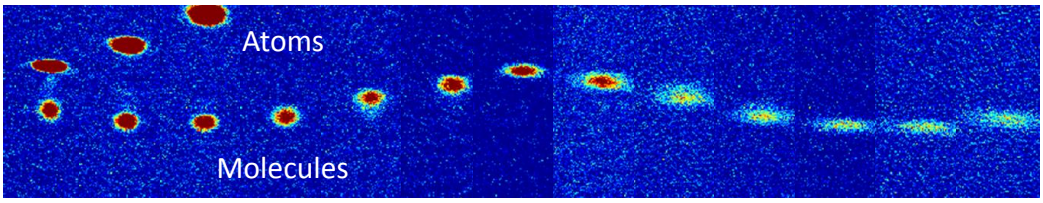

Figure 7.6: 'Bouncing' of Cs_2 molecules. The molecules are exposed to a gradient field of 40 G/cm which under-levitates molecules in the $4g(4)$-state and over-levitates molecules in the $6g(6)$-state. The molecules are oscillating around the point in space where they experience a bias field corresponding to the avoided crossing at 13.5 G. The atoms are pushed out of the top of the image area. The images are taken in steps of 5 ms and their size is 1.3 × 0.55 mm.

due to the magnetic field gradient, this gives us the possibility to 'bounce' the molecular cloud, which can be seen in figure 7.6 [74]. For this experiment, a field gradient of 40 G/cm is applied and the bias field after the association sequence set to 14.9 G at the position of the optical dipole trap. Thus the falling molecules are exposed to a magnetic bias field just below 13.5 G. During the magnetic field ramp, they are transferred into the $6g(6)$-state and thus pushed upward. Above a certain position, they are transferred back into the $4g(4)$-state for which the gradient field is not sufficiently high to support the molecules any more, so they fall down.

The magnetic moment of the molecules is calculated from the bound-state picture shown in figure 7.1. Here, the binding energy is given with respect to the energy of two unbound atoms, which changes with magnetic field according to the Breit-Rabi formula. The slope of the bound-state energy with respect to the energy of the free atoms gives the magnetic moment of the molecules. The magnetic moment does not change instantly, but follows the curvature at the avoided crossing. In the left panel of figure 7.7, the magnetic moment of a molecular sample adiabatically following the avoided crossing between the $4g(4)$ and $6g(6)$-state is shown.

When a magnetic field gradient of 40 G/cm is applied, the molecules experience the potential presented in the right panel of figure 7.7 due to the changing magnetic moment. We simulated the motion of a particle in this potential using the equation

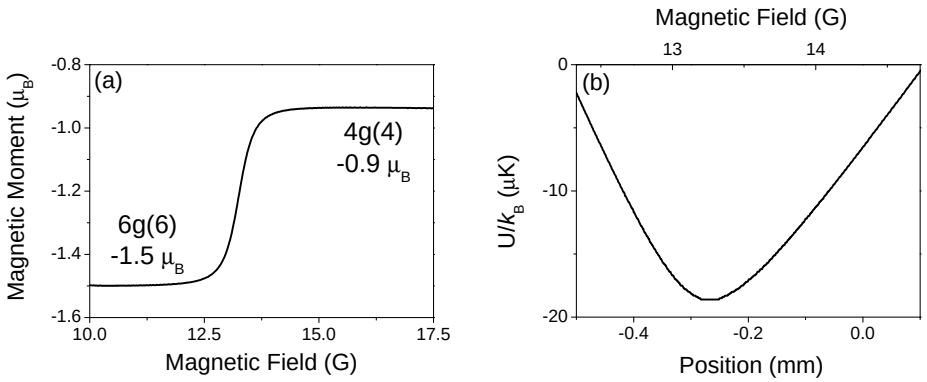

Figure 7.7: (a): Magnetic moment versus bias field of a Cs_2 dimer following the avoided crossing between the $4g(4)$ and $6g(6)$-state adiabatically. (b): The potential for the Cs_2 molecules for a magnetic field gradient of 40 G/cm including gravity in the vertical direction resulting from their change in magnetic moment with position.

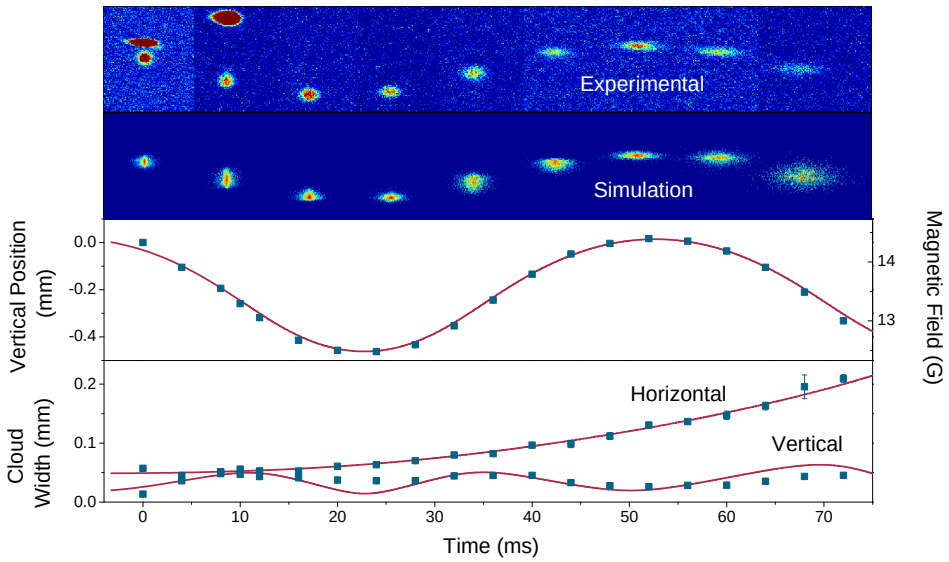

Figure 7.8: Position and shape of the molecular cloud versus time. The motion of the molecules is simulated in a quadrupole field with a magnetic field gradient of 40 G/cm and the potential presented in figure 7.7. In the top panel, absorption images and results of the simulation are presented. In the two panels below, the experimental data and results of the simulation of the cloud position and widths in the horizontal and vertical direction are shown.

$$\frac{\mathrm{d}^2 z}{\mathrm{d}t^2} = -\frac{\nabla(\mu(z) \cdot B(z))}{m} - g, \tag{7.1}$$

where m is the mass of the molecules, g the gravitational acceleration and z is the position in the vertical direction. Additional knowledge of the horizontal potential due to the quadrupole field makes it possible to simulate the motion of a two dimensional cloud in the gradient field. The initial spread of molecules is caused by the Gaussian distribution of the atomic cloud before the association and the time over which the magnetic field is swept over the Feshbach resonance to associate the molecules. The velocity of the molecules follow the Maxwell-Boltzmann distribution of the particles with a temperature of 60 nK. The results are presented in figure 7.8. The top panel shows absorption images of the oscillating Cs_2 cloud and the simulated model. In the two panels below the experimental data, results of the simulation of the cloud position and widths in the horizontal and vertical direction are shown.

During the motion, the maximum rate of change of the magnetic field is 0.134 G/ms which is well below the critical ramp speed of $\sim$ 1100 G/ms (see equation (2.19)). Hence, the molecules are all transferred adiabatically between the two states.

The theory agrees with the experimental results, which confirms good knowledge of our trapping potential and the bound-state picture near the avoided crossing.

7.4 Multiple outcoupling of molecules

The molecules and atoms experience a potential consisting of a dipole trap plus a magnetic field gradient to cancel gravity. The latter has the effect that the magnetic field the ultracold sample is exposed to, changes with position. When the molecules fall down after their association, during the Stern-Gerlach separation, they are exposed to a decreasing bias field. This makes it possible to increase the bias field after the association ramp again to a value above the Feshbach resonance at the position of the atoms but not the

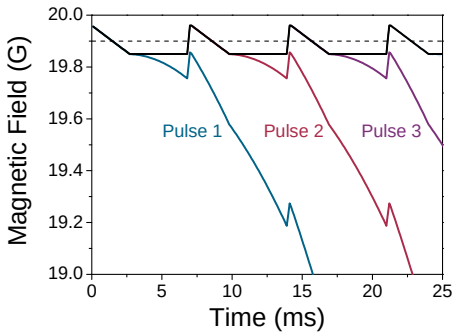

Figure 7.9: Magnetic field the trapped atoms (black) and the out-coupled Cs_2 molecules (coloured) are exposed to. The dashed line marks the position of the Feshbach resonance. The magnetic field in the position of the atoms can cross the Feshbach resonance without dissociating the molecules. Thus multiple samples of molecules can be produced.

molecules. Consequently, the molecules are not dissociated and keep falling. Another molecular sample can then be produced by sweeping across the resonance again. This process can be repeated several times. The magnetic field ramping sequence and the field the atoms and molecules are exposed to are shown in figure 7.9.

The association ramp in this sequence is a magnetic field sweep from 19.96 G to 19.85 G in 2.5 ms. Then the field is kept at 19.85 G for 4.1 ms until the molecular cloud has separated from the atoms. After this, the field at the position of the atoms is ramped back up to 19.96 G in 0.2 ms. After a hold time of 0.1 ms, the field is ramped down to 19.85 G in 2.7 ms again to produce another sample of molecules. This way, a pulse of Cs_2 molecules is produced every 7.1 ms. Molecules were detected after up to 25 of these association ramps (figure 7.12).

The molecule production in this sequence is not as efficient as in the single pulse production sequence, since the ramp across the resonance is faster here to achieve a higher repetition rate. In figure 7.10 the effect of the outcoupling of molecules on the atomic sample is shown. With the molecule production, the atom number decreases more rapidly. This is due to the molecules formed from the atoms and coupled out of the atomic cloud which is shown in figure 7.11. The molecule production also increases the temperature of the residual atoms. This happens since the molecules are formed preferentially

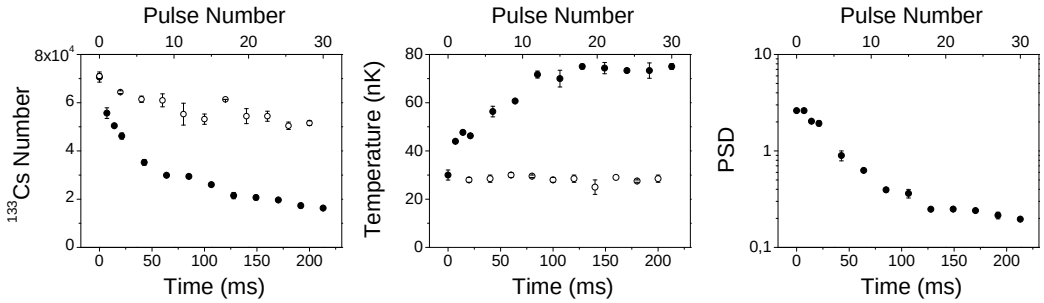

Figure 7.10: Atom number (left), temperature (centre) and PSD (right) with (closed circles) and without (open circles) molecule production versus time. The top axis shows the number of outcoupled molecular pulses. The atomic cloud is heated during the outcoupling, since the molecules are formed preferentially from the coldest atoms. The first two samples are coupled out of a BEC. The PSD data without molecule production is not shown since the BEC lifetime is longer than 230 ms.

from the coldest atoms in the sample and the remaining atoms rethermalise to a higher temperature. The atomic sample is evaporated to BEC before the outcoupling sequence to increase the total number of molecular pulses that can be coupled out of a single atomic sample since the PSD of the atomic cloud decreases during the sequence. The first two molecular samples are coupled out of a Cs BEC.

In figure 7.11, the molecule number in each outcoupled pulse and the total number of molecules coupled out of a single atomic sample are presented. The number of molecules produced during the first association ramp is $3.7(4) \times 10^3$. The total number of molecules produced in 24 association ramps in one sequence is $1.55(6) \times 10^4$. Absorption images of 24 molecular pulses are shown in figure 7.12. Since the first molecular sample is falling out of the imaging area after 6 pulses are produced, only 6 samples are imaged at a time. The top clouds are the Cs atoms in the dipole trap.

7.5 'Collision' of two molecular samples

For this experiment, the two previously presented effects are combined. First, two molecular clouds are coupled out of an atomic sample. After the second outcoupling process, the magnetic bias field is ramped down to transfer the molecules into the $6g(6)$-state and the gradient field is increased to 40 G/cm

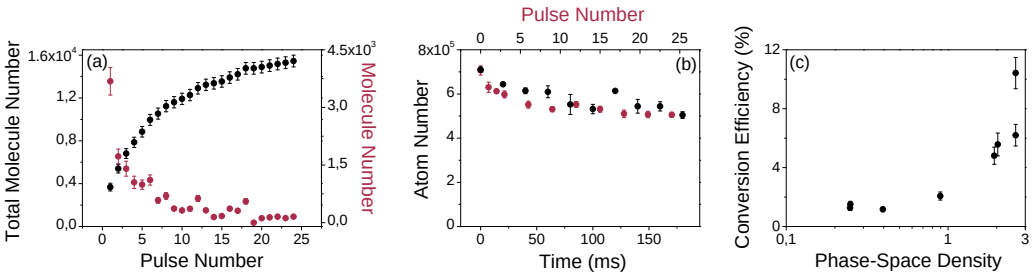

Figure 7.11: (a): Integrated number of molecules produced (black) and the number of molecules associated in each association ramp (black). (b): Atom number in the trap without molecule production (black) and the sum of atoms left in the trap after molecule production and the number of atoms converted into molecules (red). Additional trap losses during the multiple outcoupling sequence only result from the molecule formation, since both numbers agree. (c): Cs atoms to molecules conversion efficiency during the multiple outcoupling sequence. The efficiency decreases faster compared to the single pulse production (see figure 7.4), since the molecules are preferentially formed from the coldest atoms and the atomic sample does not thermalise between the molecule production ramps.

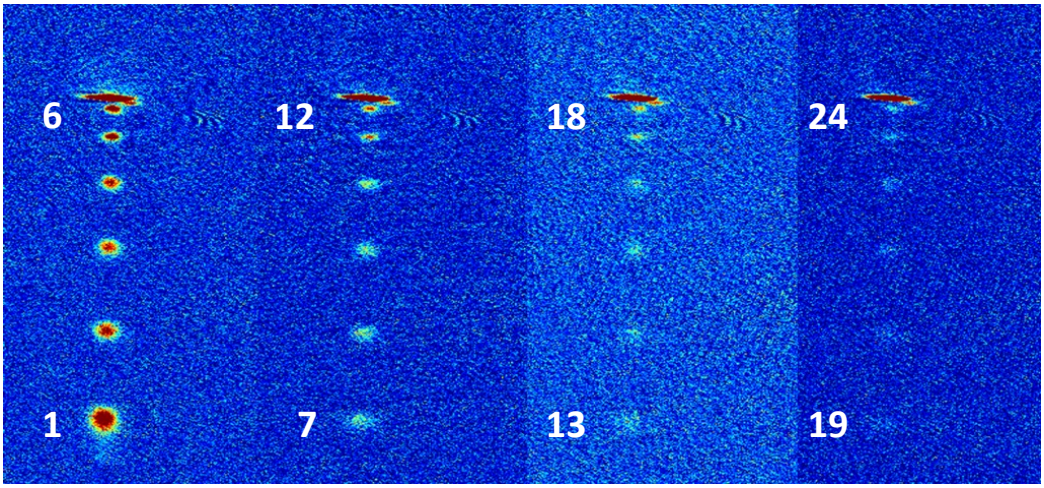

Figure 7.12: Absorption images of the molecular samples. Only 6 pulses can be imaged at a time since the first associated molecules fall out of the imaging area after the corresponding time. The atomic cloud in the dipole trap can be seen on the top of each image. We could not establish the origin of the fragment next to the atomic cloud. The size of each image is $4.35 \times 2.35\,\mathrm{mm}$.

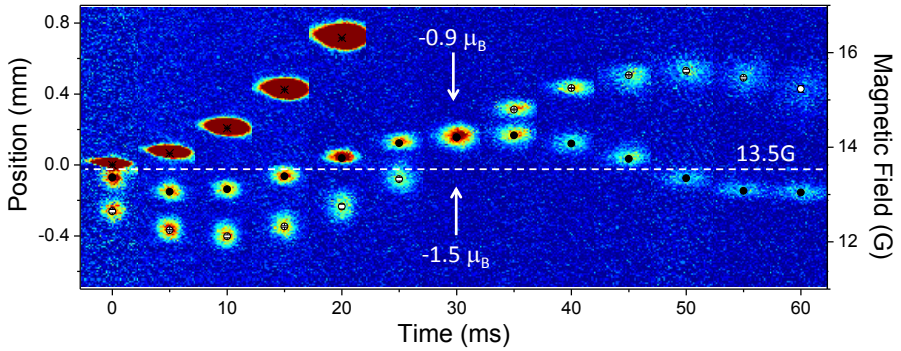

Figure 7.13: Bouncing and 'collision' of two molecular clouds. Two molecular clouds are coupled out of one atomic sample and 'bounce' in a gradient field of 40 G/cm. The outcoupling and bias fields are chosen such that the two molecular clouds 'collide' after 30 ms time of flight.

so that they experience a force pushing them up. The trajectory of the two clouds is shown in figure 7.13.

After the magnetic field ramp, the two clouds are pushed up. The first cloud falls slightly further down, since it has a higher initial velocity. The second cloud does not experience the force pushing it up for long, so it slows down quickly after it is pushed into a region where it is exposed to a bias field below 13.5 G. At this time, the first cloud is still pushed up and the two clouds are at the same position in the imaging axis after 30 ms.

From simulations of the positions and the widths of the molecular clouds similar to the ones presented in figure 7.8, we concluded that no interactions between the two clouds occur. This results from the low molecular density of $\sim 10^8\,\mathrm{cm}^{-3}$.

Since the two molecular clouds are coupled out of the same Cs BEC it could be possible to observe interference between the two molecular clouds in future experiments, similar to the interferences observed between two BECs [209].

7.6 Conclusion

We used a Feshbach resonance at $\sim 19.9\,\mathrm{G}$ to produce $2.1(1) \times 10^4$ molecules out of a sample of $3.28(2) \times 10^5$ Cs atoms with a PSD of 0.20(1). The

molecules were separated from the atoms using the Stern-Gerlach technique. The molecules can be confined in the optical dipole trap where we measured a lifetime of 0.88(8) s.

We demonstrated the control over the internal state of the molecules by 'bouncing' the molecules using an avoided crossing between two states at 13.5 G in a magnetic field gradient of 40 G/cm. This magnetic field gradient was also used to produce multiple molecular clouds from one atomic sample. A combination of both techniques leads to the 'collision' of two molecular samples.

In the next step we use our experience gained from work with homonuclear Cs_2 molecules to produce heteronuclear ^{87}RbCs molecules.

Chapter 8

Towards ground state polar molecules

The following publication resulted out of the work presented in this chapter:

Production of optically trapped $^{87}RbCs$ Feshbach molecules
M.P. Köppinger, D.J. McCarron, D.L. Jenkin, P.K. Molony, H.W. Cho, C.L. Blackley, C.R. Le Sueur, J.M. Hutson and S.L. Cornish
Phys. Rev. A (2014) (to be published)

We report the production of $^{87}RbCs$ Feshbach molecules in a crossed-beam dipole trap. A mixture of ^{87}Rb and ^{133}Cs is cooled close to quantum degeneracy before an interspecies Feshbach resonance at 197 G is used to associate up to $\sim$ 5000 molecules with a temperature of $\sim$ 300 nK. The molecules are confined in the dipole trap with a lifetime of 0.21(1) s, long enough for future experiments exploring optical transfer to the absolute ground state. We have measured the magnetic moment of the Feshbach molecules in a magnetic bias field range between 181 and 185 G to demonstrate the ability to control the character of the molecular state. In addition we have performed Feshbach spectroscopy in a field range from 0 to 1200 G and located three previously unobserved resonances at high magnetic fields.

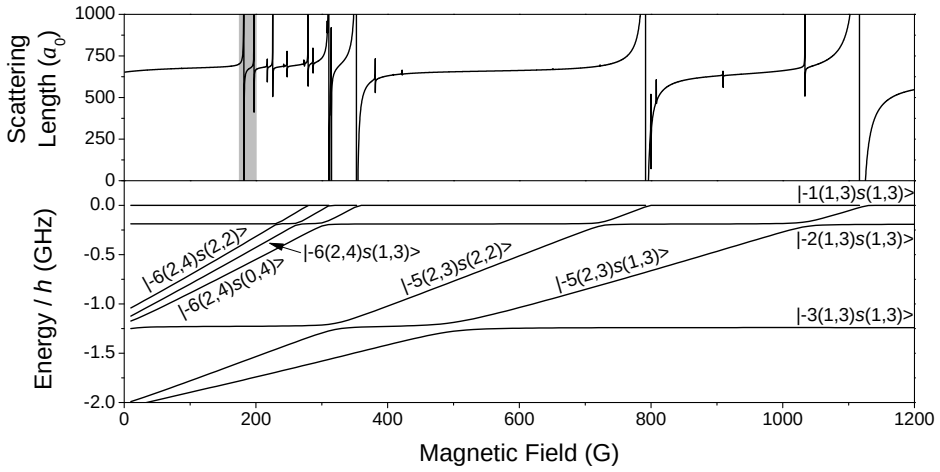

Figure 8.1: Top panel: The interspecies scattering length between ^{87}Rb and ^{133}Cs in the $(f = 1, m_f = +1)$ and $(3, +3)$ states respectively, calculated using the s and d basis functions, versus magnetic field. The grey shaded area marks the range relevant to magnetoassociation. Bottom panel: The calculated weakly bound molecular states arising from $L = 0$ (s-states). The bound-state energies are plotted relative to the energy of the lowest hyperfine state of ^{87}Rb and ^{133}Cs. All the bound states shown are for $M_{tot} = 4$, corresponding to s-wave scattering in the lowest channel [210].

8.1 Overview

In this chapter, the formation of ^{87}RbCs Feshbach molecules and spectroscopy on molecular states is presented. This is done to find appropriate states with good couplings for the STIRAP transfer to the absolute ground state of the molecules. The interspecies s-wave scattering length between ^{87}Rb and ^{133}Cs in their individual lowest spin channel in the experimentally accessible field from 0 to 1200 G is presented in the top panel of figure 8.1. Characteristic for this mixture is the large positive value of the background scattering length of $+651(10)\,a_0$ [83]. The resulting large three-body losses make it difficult to produce a large sample of ultracold atoms at high PSD, which is necessary for magnetoassociation [158–160]. Additionally, the atomic mixture is immiscible if cooled to quantum degeneracy [211]. Fortunately, the s-wave scattering length also shows a rich Feshbach spectrum especially in the relatively low magnetic field range up to 400 G. This makes it possible to tune the interspecies collisions and magnetoassociate molecules.

The Feshbach association and spectroscopy on the molecules presented in this work is performed in the grey shaded magnetic field range in figure 8.1. The bottom panel of the figure shows the bound-state energy of the ^{87}RbCs molecule immediately below threshold up to a binding energy of 2 GHz $\times h$. The bound states are labelled as $|n(f_{\mathrm{Rb}}, f_{\mathrm{Cs}})L(m_{f_{\mathrm{Rb}}}, m_{f_{\mathrm{Cs}}})\rangle$. Here, n is the vibrational level with respect to the associated hyperfine threshold $(f_{\mathrm{Rb}}, f_{\mathrm{Cs}})$, where $n = -1$ represents the least bound state. The sum of the projection of all angular momenta M_{tot} is always 4 and not specified in this expression. In figure 8.2(c), a zoom into grey shaded area in figure 8.1 is presented. This is the region relevant to magnetoassociation of ^{87}RbCs molecules. In figure 8.2(a) and (b), the two Feshbach spectroscopy loss features caused by the interspecies Feshbach resonances at (a) 181.55(5) G and (b) 197.10(3) G are shown.

8.2 Association of RbCs molecules

A sample with high phase-space density is needed to allow magnetoassociation of molecules [185]. The route to an ultracold mixture is described in chapter 3 and in previous publications of our group [159, 160, 207]. After initial cooling in the magnetic trap, the mixture of ^{87}Rb and ^{133}Cs is loaded into the crossed-beam optical dipole trap by decreasing the magnetic gradient field to 29 G/cm. This happens at a temperature of $\sim 40\,\mu$K, where Majorana spin flips prevent further cooling in the magnetic trap [157]. Subsequently, RF adiabatic rapid passage is applied to transfer the atoms into their absolute internal ground state, namely the $(f = 1, m_f = +1)$ and (3,+3) state for ^{87}Rb and ^{133}Cs respectively [207] and the magnetic bias field is ramped up to 22 G in 18 ms. At this point, $2.8(2) \times 10^6$ ^{87}Rb atoms at a temperature of $9.6(1)\,\mu$K are confined in the dipole trap. The number of ^{133}Cs atoms in the MOT is varied to have control over the exact composition of the mixture after evaporation. Due to their different polarisabilities for 1550 nm light, the trap is ~ 1.35 times deeper for ^{133}Cs than for ^{87}Rb [151]. This leads to direct evaporation of ^{87}Rb by decreasing the beam power while ^{133}Cs is cooled sympathetically. The large interspecies scattering length of $+651(10)\,a_0$ supports this cooling and the two species remain in thermal equilibrium. The

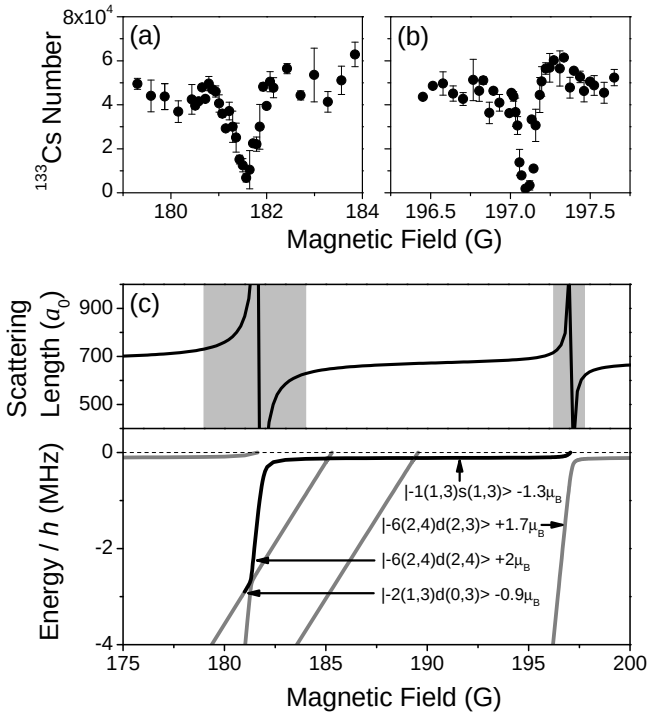

Figure 8.2: The magnetoassociation sequence. The interspecies Feshbach resonances at (a) 181.55(5) G and (b) 197.10(3) G detected through loss in the ^{133}Cs atom number. (c) Top panel: The interspecies scattering length between ^{87}Rb and ^{133}Cs in the relevant magnetic field range. The grey shaded areas mark the field ranges shown in (a) and (b). Bottom panel: The weakly bound molecular states relevant to the magnetoassociation sequence calculated using the s and d basis functions. Also shown are the magnetic moments for each bound state. Molecules are produced at the Feshbach resonance at 197.10(3) G and then transferred into the $|-2(1,3)d(0,3)\rangle$ state at 181 G following the path shown by the solid black line.

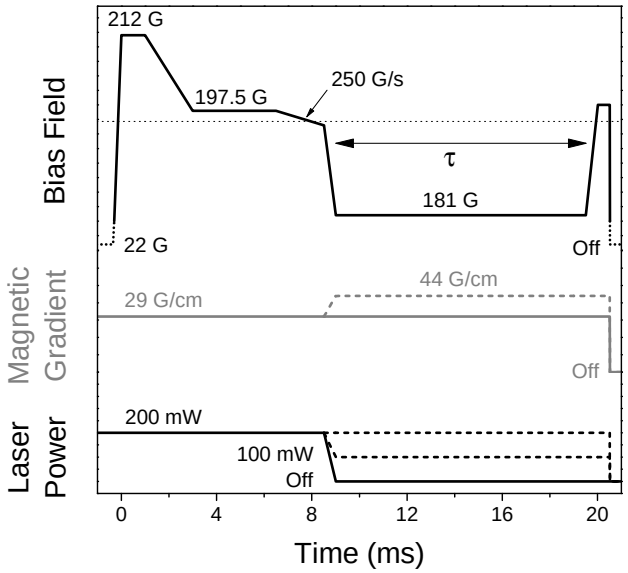

Figure 8.3: The experimental sequence for the creation, Stern-Gerlach separation and detection of Feshbach molecules. An ultracold atomic mixture is initially created by evaporation in the dipole trap at a bias field of 22 G. Subsequently the timing sequences shown for the bias field, magnetic field gradient and laser power in each beam of the crossed dipole trap are applied. The horizontal dotted line indicates the position of the Feshbach resonance at 197.10(3) G used for magnetoassociation. The dashed lines show the changes to the routine implemented to trap the atoms in the dipole trap. The hold time, τ, in the dipole trap is varied to measure the lifetime of the molecules.

trap depth is decreased from 76 μK (103 μK) to 3.1 μK (4.2 μK) for Rb (Cs) over 1.25 s. This leads to a mixture consisting of $\sim 1 \times 10^5$ atoms with a PSD larger than 0.1 for each species, which is high enough for magnetoassociation.

The timing of the following experimental sequence is presented in figure 8.3. The magnetic bias field is increased from 22 G to 212 G in 2 ms. During this ramp, several inter- and intraspecies Feshbach resonances are crossed quickly to avoid three-body losses induced by the large scattering length in their vicinity. When the magnetic field has settled, it is decreased to 197.5 G, a value close to the position of the Feshbach resonance (see figure 8.2(b)). After a 3.5 ms hold time, the Feshbach resonance is crossed by decreasing the field by 0.5 G in 2 ms.

The resonance used for association arises from the $|-6(2,4)d(2,3)\rangle$ molec-

ular state. However, since the least bound state only has a binding energy of 110(20) kHz $\times h$, the molecules are transferred straight into the $|-1(1,3)s(1,3)\rangle$ state [83]. The magnetic moment to mass ratio of molecules in this state is very similar to the individual atoms (see chapter 2.4). This makes Stern-Gerlach separation of the molecules from the atoms impossible. Fortunately, the internal state of the molecules can be manipulated by changing the magnetic bias field. The Landau-Zener tunnelling at avoided crossings between different molecular states can be controlled with the ramp speed of the magnetic field. A magnetic field ramp to 181 G in 0.5 ms is used to transfer the molecules via the weak-field seeking $|-6(2,4)d(2,3)\rangle$ state into the high-field seeking $|-2(1,3)d(0,3)\rangle$ state. Simultaneously, the optical dipole trap is switched off.

Molecules in this state have a magnetic moment of -0.9 μ_B and hence have a significantly different magnetic moment to mass ratio from the atoms. Consequently, the molecules separate in the magnetic field gradient. The molecules are completely separated from the atoms after 7 ms of time-of-flight. The path between the different states the molecules occupy is represented with a black line in figure 8.2(c).

For imaging, the molecules are dissociated after the separation time, τ, by crossing the Feshbach resonance in the opposite direction and the magnetic bias field is switched off. Absorption images of the two species with a delay of 5.01 ms are then taken.

To increase the association efficiency, the time of the 0.5 G ramp across the Feshbach resonance was varied. The results, presented in figure 8.4, show that molecule production is possible for a wide range of ramping times from ~ 1 ms to ~ 20 ms. If the ramp speed is too high, the resonance is crossed diabatically (see equation (2.19)) and the population stays in the initial state. For slow ramps the molecules are not separated from the atoms quickly enough and losses through inelastic collisions decrease the molecule production efficiency. The ramp time was set to 2 ms for the following experiments, which corresponds to a ramp speed of 250 G/s.

An important factor affecting molecule production in our experiment is the mean of the PSD of the ^{87}Rb and ^{133}Cs atoms before the association sequence.

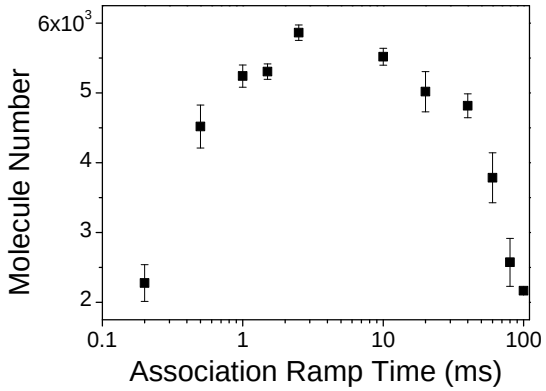

Figure 8.4: Association ramp time versus molecule production. The time for the 0.5 G ramp starting at 197.5 G to a lower field during which the Feshbach resonance is crossed and the molecules are associated is varied and the molecule number detected. The absolute number of associated molecules depends on the ramp speed and a high number can be observed between a ramp time of ~ 1 ms to ~ 20 ms. The value was set to 2 ms which corresponds to a ramp speed of 250 G/s. The error bars indicate the statistical uncertainties gained from three measurements.

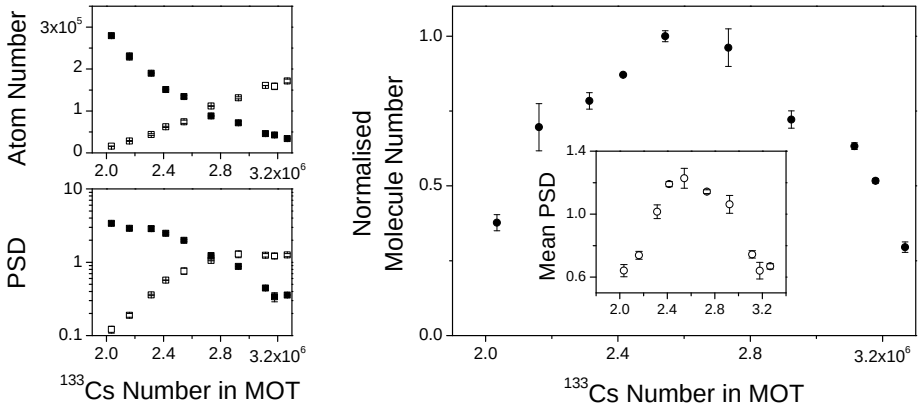

Figure 8.5: Left: ^{87}Rb and ^{133}Cs atom number and PSD after evaporation and before magnetoassociation versus the number of ^{133}Cs atoms loaded into the MOT. Right: The normalised molecule number and geometric mean of the peak PSD (inset) of the two species before association versus ^{133}Cs MOT load. The conversion efficiency is larger when the PSD of both atomic samples is high before the association process.

The Cs atom number in the MOT is controlled by detecting the MOT fluorescence signal and feeding it back to control the repump light intensity. Different Cs atom numbers in the MOT result in different compositions and hence different PSDs of the mixture after the evaporation process.

The atom number and PSD for each species after the evaporation process and before the association sequence for different Cs MOT loads is presented on the left in figure 8.5. The normalised number of associated molecules is presented in figure 8.5 on the right and the geometric mean of the peak intensity of the two species in the inset. The atom numbers after evaporation are very sensitive to the initial MOT load. When the Cs number in the MOT changes by 50%, the final atom numbers and PSDs of Rb and Cs after evaporation change by an order of magnitude. The large impact on both species originates from the reliance on sympathetic cooling of ^{133}Cs by ^{87}Rb during the evaporation.

The molecular conversion efficiency follows the geometric mean of the ^{87}Rb and ^{133}Cs peak phase-space densities. The maximum molecule number produced during this measurement was $\sim$ 3000 from an ultracold mixture of $\sim 1 \times 10^5$ atoms of each species at a temperature of 0.1 μK. To increase the molecule number the evaporation is stopped earlier resulting in a larger number of $\sim 2 \times 10^5$ atoms of each species at a temperature of 0.3 μK. A maximum number of $\sim$ 5000 molecules can be produced under these conditions which represents a conversion efficiency of $\sim$ 2.5%.

8.3 Optical trapping of molecules

For further experiments, it is advantageous to trap the molecular cloud to keep it at the same position in space and at a high density. The differences in the experimental sequence between the Stern-Gerlach separation, where the dipole trap is switched off, is shown with dashed lines in figure 8.3. After the magnetic bias field is ramped to 181 G, the gradient field is increased to 44 G/cm to levitate the molecules and the power in the dipole trap is adjusted to a value between 200 mW and 100 mW. The atoms are no longer trapped in this configuration; the remaining atoms are over-levitated and pushed out

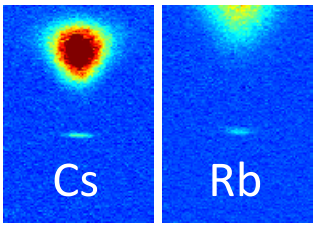

Figure 8.6: Absorption images of Cs and Rb after the dissociation of optically trapped RbCs Feshbach molecules (bottom clouds), after a trapping time of 15 ms. The position of the two atomic clouds are different due to the time delay of imaging of the two species of 5.01 ms. The size of each image is 1.3×0.7 mm.

from the trap, with no atoms left in the trap after 5 ms (see figure 8.6).

We have measured the lifetime of the molecules in the $|-2(1,3)d(0,3)\rangle$ state at a magnetic bias field of 181 G in the trap by detecting the molecule number after different trapping times. For this experiment the molecules are confined in a trapping potential formed by the dipole trap beams with a power of 100 mW per beam and the magnetic field gradient. The results are presented in figure 8.7. An exponential fit to the molecule number yields a lifetime of 0.21(1) ms. This provides enough time for further experiments, such as spectroscopy on electronically excited states of the molecules to detect an intermediate state for the STIRAP transfer and ultimately for the STIRAP transfer itself.

8.4 Magnetic moment of RbCs molecules

The magnetic moment of the molecules in their different states during the magnetic field ramp between 185 G and 181 G is calculated from their change in energy with magnetic bias field. The magnetic moment of the ^{87}RbCs molecules was measured for different magnetic bias fields. The results are presented in figure 8.8. First, the molecules are confined in the optical dipole trap at 181 G for 50 ms until they are in a steady position. Then the optical dipole trap is switched off and the molecules are exposed to different magnetic bias fields and magnetic field gradients. This leads to different displacements of the molecular cloud. The magnetic field gradient to levitate the molecules and thereby the magnetic moment of the molecules can be determined from

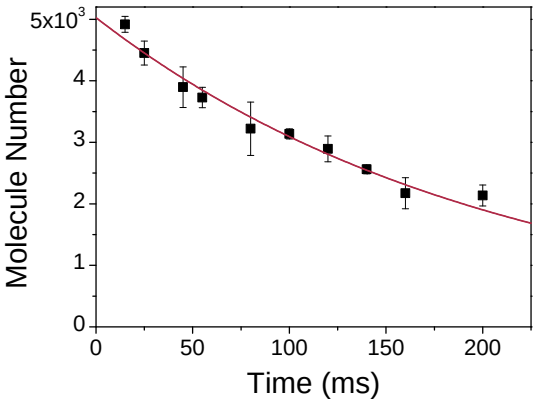

Figure 8.7: Lifetime of ^{87}RbCs molecules in the $|-2(1,3)d(0,3)\rangle$ state at 181 G held in the optical dipole trap. A magnetic field gradient of 44 G/cm is applied to levitate the molecules and the power in each beam of the dipole trap is 100 mW. Under these conditions, there is no trapping potential for the atoms. The solid line shows an exponential fit to the results, which yields a lifetime of 0.21(1) s.

these data. With the current coil configuration, only molecules in a high-field seeking state can be levitated, thus only data for molecules with a negative magnetic moment are taken. The excellent agreement between experiment and theory demonstrates the ability to control the character of the molecules.

From the results presented in figure 8.9, we can derive the low-field seeking character of the ^{87}RbCs molecules between 182.07 G and 184.48 G. Here a sample of molecules was prepared and confined in the dipole trap. Then the molecular cloud was released from the trap and its position detected after 2 ms time-of-flight in different magnetic gradients and bias fields. The molecules in the $|-2(1,3)d(0,3)\rangle$ state are levitated in a magnetic field gradient of $\sim$ 44 G/cm and in the $|-1(1,3)d(1,3)\rangle$ state in a gradient of $\sim$ 30 G/cm. The molecules are pushed down when they are in the high-field seeking intermediate state. The larger the applied magnetic gradient field is, the stronger the molecules are pushed down.

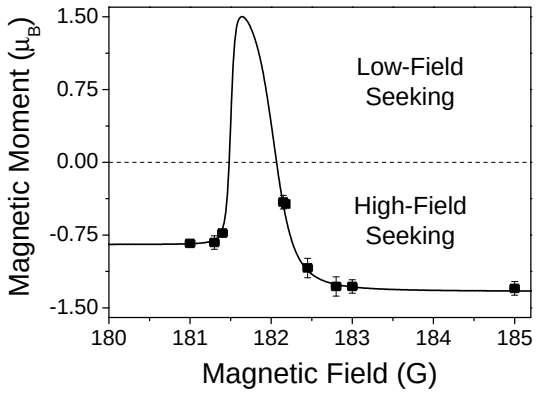

Figure 8.8: Magnetic moment of the ^{87}RbCs molecules as a function of the magnetic bias field. The experimental points are determined by finding the magnetic field gradient at which the molecules are levitated. Note the measurements are restricted to magnetic moments in the high-field-seeking region due to the current coil geometry in the experiment. The solid line is the theoretical prediction for the magnetic moment of the molecular states, obtained from the binding energies of the molecules (see chapter 2.2.4) following the magnetoassociation path shown in figure 8.2.

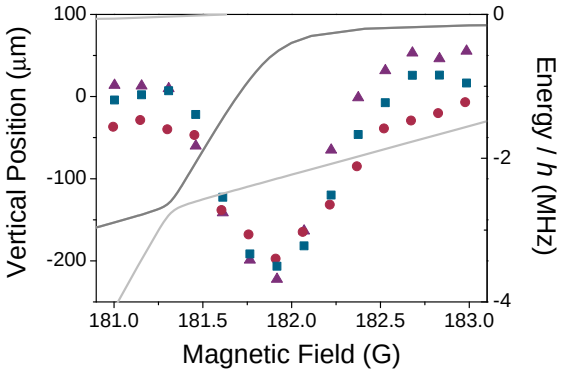

Figure 8.9: Position of the molecular cloud after 2 ms time of flight in a magnetic gradient field of 30 G/cm (circles), 44 G/cm (squares) and 56 G/cm (triangles). The magnetic bias field is given for the initial position of the molecular cloud in the optical dipole trap. The dark grey line represents the evolution of the binding energy of the molecules and the states according to figure 8.2(c). The molecules are pushed down when exposed to a magnetic bias field between 182.07 G and 184.48 G since they are in a low-field seeking state.

8.5 Molecular spectroscopy for STIRAP transfer

In chapter 2.6, we discussed that candidates for intermediate states for STIRAP exist in the range between 6300 cm^{-1} and 6600 cm^{-1} above the $5S_{1/2} + 6S_{1/2}$ threshold, which corresponds to a wavelength between 1515 nm and 1587 nm [89, 94]. The diode laser used in the experiment covers a wide wavelength range from 1490 to 1580 nm (chapter 4.4.3). This makes it possible to reach different vibrational levels of the electronically excited molecular state.

At the beginning of the work for this thesis, the position of the vibrational states was only known to a precision of a few GHz through ab initio calculations and Fourier-transform spectroscopy [103, 133] and transition strengths between the states were not known. However, recent work from the Innsbruck group has resulted in much more precise positions of the electronically excited molecular states down to a few MHz [94, 134]. These results were used to find and identify the different vibrational states.

We performed spectroscopy on the $A^1\Sigma^+$–$b^3\Pi_0$ and on the $b^3\Pi_1$ potentials. The initial molecules are in the $|-2(1,3)d(0,3)\rangle$ state at 181 G. The $A^1\Sigma^+$–$b^3\Pi_0$ potential was proposed to support suitable states for the STIRAP transfer since good Franck-Condon overlaps were predicted for both transitions [132]. However, spectroscopic work in Innsbruck has shown an unresolved excited hyperfine splitting of states of the $A^1\Sigma^+$–$b^3\Pi_0$ potential, which can suppress an efficient STIRAP transfer [66]. It was proposed [212] and measured [94], that the hyperfine splitting is larger for states with $\Omega = 1$. Therefore, spectroscopy was also performed on states of the $b^3\Pi_1$ potential. Here, the $|\Omega = 1, v' = 29\rangle$ state is especially interesting. Usually states of this potential do not couple to the absolute ground state due to their triplet character. However, this state has some singlet character through coupling to the nearby $|0, 38\rangle$ state of the $A^1\Sigma^+$–$b^3\Pi_0$ potential. This makes the $|\Omega = 1, v' = 29, J' = 1\rangle$ state a candidate for the intermediate state of the STIRAP transfer.

For the spectroscopy, the 1550 nm laser of the setup described in chapter 4.4

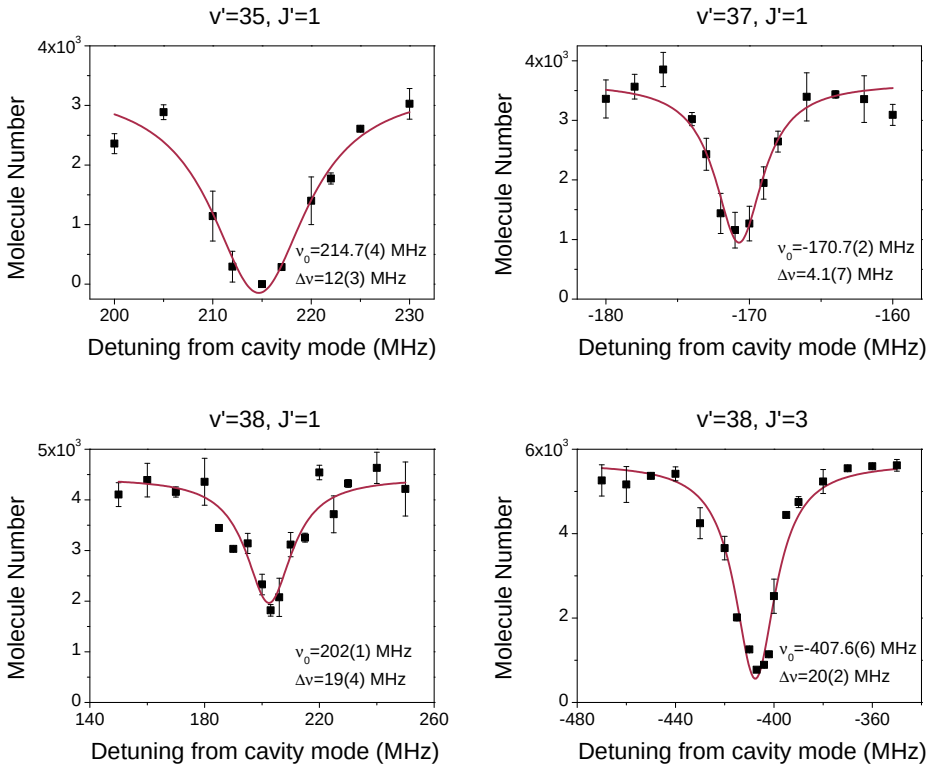

Figure 8.10: Molecular loss spectroscopy on vibrational states of the $A^1\Sigma^+$–$b^3\Pi_0$ potential. The detuning on the x-axis is given with respect to the closest cavity mode which is used as the reference to stabilise the laser frequency. The quoted frequency errors are due to the Lorentzian fit. The absolute frequency of the transitions is given in table 8.1.

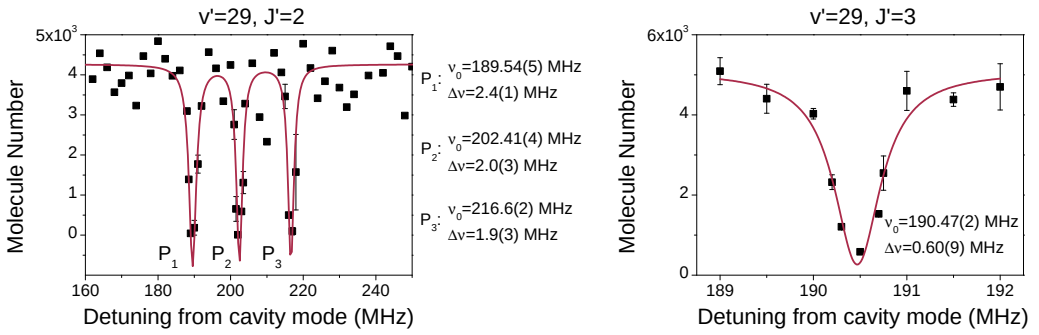

Figure 8.11: Molecular loss spectroscopy on vibrational states of the $b^3\Pi_1$ potential. The detuning on the x-axis is given with respect to the closest cavity mode which is used as the reference to stabilise the laser frequency. The quoted frequency errors are due to the Lorentzian fit. The absolute position of the transitions can be found in table 8.1. The $J' = 2$ transition has a resolved hyperfine structure.

is used. The irradiation time and intensity are varied using an AOM such that the loss features are not saturated or power broadened. For each measurement, a sample of ^{87}RbCs molecules in the $|-2(1,3)d(0,3)\rangle$ state was produced. After the irradiation with the spectroscopy laser, the molecules were dissociated and imaged. The loss spectroscopy features are presented in figure 8.10 and figure 8.11 for spectroscopy on the $A^1\Sigma^+$–$b^3\Pi_0$ potential and the $b^3\Pi_1$ potential, respectively. On the x-axis, the detuning from the closest cavity resonance is given. The spectroscopy laser is locked to this resonance and shifted by a given frequency using a fibre-coupled EOM (see chapter 4.4.3). The errors in frequency given here are only due to the Lorentzian fit. The error on the absolute position of the transitions is determined by the error on the wavemeter reading, which is 20 MHz. The positions of all investigated transitions are given in table 8.1. The widths of the resonances due to states in the $b^3\Pi_1$ potential are narrower than widths of the mixed $A^1\Sigma^+$–$b^3\Pi_0$ potential. This is due to different coupling strengths to the ground state potential. The resonances are wider for states with good coupling since the lifetime is shorter in these states. Resonances associated with the $b^3\Pi_1$ potential are narrower, as expected due to their more dominant triplet character.

Ω	v'	J'	Laser Frequency (GHz)	E_{exp} (cm^{-1})	Previous Work [134] E_{calc}(cm^{-1})	E_{exp}(cm^{-1})
0^+	35	1	190789.15(2)	6364.041(1)	6364.04	6364.031(2)
	37	1	191826.63(2)	6398.658(1)	6398.67	6398.663(2)
	38	1	192556.42(2)	6422.973(1)	6422.97	6422.986(2)
	38	3	192556.81(2)	6423.115(1)		6423.114(2)†
1	29	1	192572.09(2)	6423.501(1)	6423.07	6423.501(2)
	29	2	192576.25(2)	6423.584(1)		6423.583(2)†
	29	3	192579.26(2)	6423.684(1)		6423.682(2)†

Table 8.1: Position of several rotational levels J' of the $A^1\Sigma^+$–$b^3\Pi_0$ and the $b^3\Pi_1$ potential. The laser frequencies to drive the transition from the $|-2(1,3)d(0,3)\rangle$ Feshbach state at 181 G. The following transition energies are corrected for the Zeeman shift and give the value for zero magnetic field. The quoted errors are due to the precision of the wavemeter. Data marked with † are extracted from figure 3 of [134].

From equation (4.1), we know that it is advantageous to drive the STIRAP transitions with large Rabi frequencies to minimise negative influences from laser frequency fluctuations. Thus it is important to know the Rabi frequency that the STIRAP transitions are driven with. To determine the Rabi frequency and optimise the alignment of the STIRAP laser beams, we measured the loss rate of the molecules when exposed to resonant light. The Rabi frequency, Ω_{P}, can be calculated by fitting the function [94]

$$N = N_0 \exp\left(-t_{\mathrm{irr}} \frac{\Omega_{\mathrm{P}}^2}{\gamma}\right), \tag{8.1}$$

to the exponential decay of the molecule number. Here, t_{irr} is the irradiation time of resonant light and γ the linewidth of the transition. We used the $|v' = 35, J' = 1\rangle$ state to align the focus of the laser beam by minimising the lifetime of the molecules in the trap under exposure of 11 mW of resonant light. The final decay curve is presented in figure 8.12. The fit results in a Rabi frequency of $\Omega_{\mathrm{P}} = 116(6)$ kHz.

From a scan across the position of the cloud we deduce a beam size of 53(7) μm in the horizontal, and 60(8) μm in the vertical direction at the position of the molecular cloud. Together with the beam power of 11 mW this results in an intensity of $I = 2P/\pi w_0^2 = 220(40)\,\mathrm{W/cm^2}$ for the spectroscopy

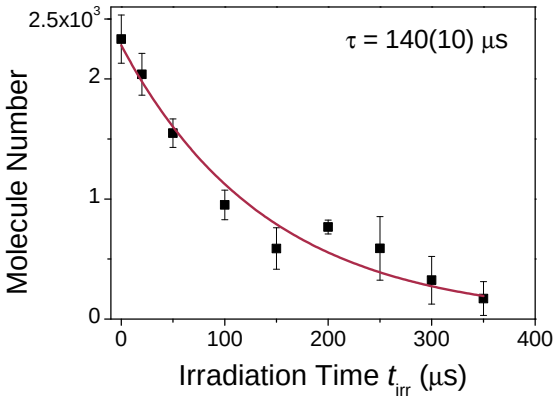

Figure 8.12: Lifetime of the Feshbach molecules in the presence of resonant light. Here, the transition to the $|v' = 35, J' = 1\rangle$ state is driven. The laser power is 11 mW, corresponding to an intensity of 220(40) W/cm^2. A Rabi frequency of $\Omega_P = 116(6)$ kHz can be derived from the fit according to equation (8.1).

beam. From this follows the normalised Rabi frequency for this transition of $0.25(5)\,\mathrm{kHz}/\sqrt{\mathrm{mW/cm^2}}$. This value is close to the previously published normalised Rabi frequency for this transition of $0.32(5)\,\mathrm{kHz}/\sqrt{\mathrm{mW/cm^2}}$ [134].

Next, two-photon spectroscopy [109, 213] is performed to identify the exact laser frequency needed for the second transition of the STIRAP, which allows the electronically excited state to be coupled to the rovibrational ground state of the molecule. The binding energy of the lowest rovibrational level of the $X^1\Sigma^+$ ground state is already known and measured to be $3811.5755(16)\,\mathrm{cm}^{-1}$ [94].

In equations (2.25) and (2.26), we have seen that an eigenstate $\cos\theta|1\rangle - \sin\theta|3\rangle$, where $\tan\theta = \Omega_P(t)/\Omega_S(t)$ exists when the two-photon detuning is zero. When $\Omega_S \gg \Omega_P$, the eigenstate is $|1\rangle$ and thus, no loss can be observed under these conditions [214].

For the spectroscopy, the pump laser is kept on resonance with an electronically excited state, while the Stokes laser is scanned. We use the $|\Omega = 1, v' = 29, J' = 1\rangle$ level as the intermediate state, since previous measurements have shown a good coupling between this state and the rovibrational ground state $|v'' = 0, J'' = 0\rangle$ [94]. For the measurement presented in figure8.13(a), the power of both lasers is 4 mW. The Stokes laser is switched

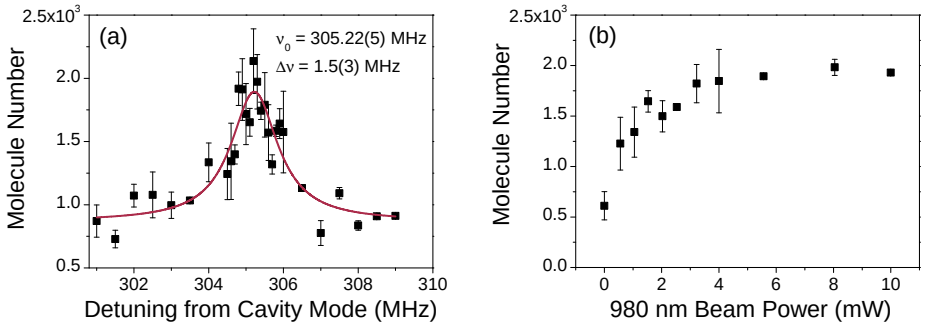

Figure 8.13: (a): ^{87}RbCs two-photon spectroscopy on the rovibrational ground state of ^{87}RbCs. The pump laser frequency is fixed to the transition to the electronically excited $|v' = 29, J' = 1\rangle$ level, while the Stokes laser is scanned. Molecules are detected when the two-photon detuning is zero. The quoted frequency errors are due to the Lorentzian fit. The laser frequency of the Stokes laser on resonance is 306830.43(2) GHz. (b): Both lasers are on transition and the power in the Stokes laser is varied.

on 200 μs before the molecules are exposed to both laser fields simultaneously for 800 μs. After this period of time, the Stokes laser is switched on for an additional 200 μs.

On resonance, the frequencies of the two lasers are $\nu_{\mathrm{P}} = 192572.09(2)$ GHz and $\nu_{\mathrm{S}} = 306830.43(2)$ GHz and their difference is 114258.34(3) GHz. Taking the Zeeman shift at 181 G (0.327 GHz) and the energy spacing of the atomic ground states (9.443 GHz) into account, the binding energy at zero field and with respect to the centre of gravity of the hyperfine manifold is 114268.11(3) GHz or 3811.574(1) cm^{-1}. The quoted error is due to the precision of the wavemeter. This measurement confirms the previously measured binding energy of the rovibrational ground state of 3811.5755(16) cm^{-1} by Debatin *et al.* [94].

8.6 Conclusion

We are able to produce up to $\sim$ 5000 ^{87}RbCs Feshbach molecules using a Feshbach resonance at 197.1 G. The molecules can be transferred into different states by changing the magnetic bias field. This technique was tested by

measuring the magnetic moment of the molecules at different magnetic bias fields (e.g. in different states). We loaded the molecules into an optical dipole trap where a lifetime of 0.21(1) s was measured, long enough to allow STIRAP transfer to the rovibrational ground state. Molecule loss spectroscopy on electronically excited states with mixed singlet and triplet character was performed and candidates for intermediate states for the STIRAP transfer were detected. These loss signals were used to optimise the alignment of the two STIRAP beams onto the molecular cloud. Following this, two-photon spectroscopy on the rovibrational ground state was performed and we measured the binding energy of this state to be 3811.574(1) cm^{-1}.

The molecule association efficiency in this experiment is lower than 10% and thus lower than in the case of Cs_2 presented in the previous chapter. Magnetoassociation from a BEC, which would increase the efficiency, is not possible in a mixture of ^{87}Rb and Cs due to the immiscibility of the quantum degenerate mixture [160]. Additionally, the large interspecies scattering length leads to large three-body losses at a high PSD close to degeneracy. Thus, a slightly higher association efficiency of 10% can be achieved when the molecules are coupled out of a sample close to degeneracy, but the absolute molecule number is smaller due to previous atom losses. To circumvent the problem of high losses and increase the association efficiency, the atoms can be loaded into an optical lattice and the molecules formed from a two-species Mott-insulator state [80, 215].

Chapter 9

Conclusion and outlook

9.1 Summary

In this thesis we have presented the results on our work on single species and two species mixture experiments involving ^{85}Rb, ^{87}Rb and ^{133}Cs. The various interspecies and intraspecies s-wave scattering lengths resulting from this work are presented in figure 9.1.

We have investigated the interactions in a mixture of ^{85}Rb and ^{133}Cs in their individual lowest hyperfine state. In contrast to the large interspecies scattering length between ^{87}Rb and ^{133}Cs, the interspecies scattering length in this mixture is close to zero over a wide magnetic field range. This can lead to efficient cooling of both species without suffering from high interspecies three-body collisions. We detected several narrow interspecies Feshbach resonances in an easily accessible magnetic field range which are possible candidates for magnetoassociation. Two wide resonances at 112.6(4)G and 641.8(3)G can be used to precisely control the interactions of the mixture and open the possibility to study Efimov physics in a heteronuclear system. Unfortunately, the highest achievable PSD of the mixture in our apparatus was 0.059(4) for ^{85}Rb and 0.041(4) for ^{133}Cs and thus not sufficiently high for magnetoassociation. However, since this mixture seems promising for the production of ultracold molecules in the future, this motivated us to establish a good understanding of the scattering properties of the constituent species. While the scattering properties of Cs have been extensively studied already [110],

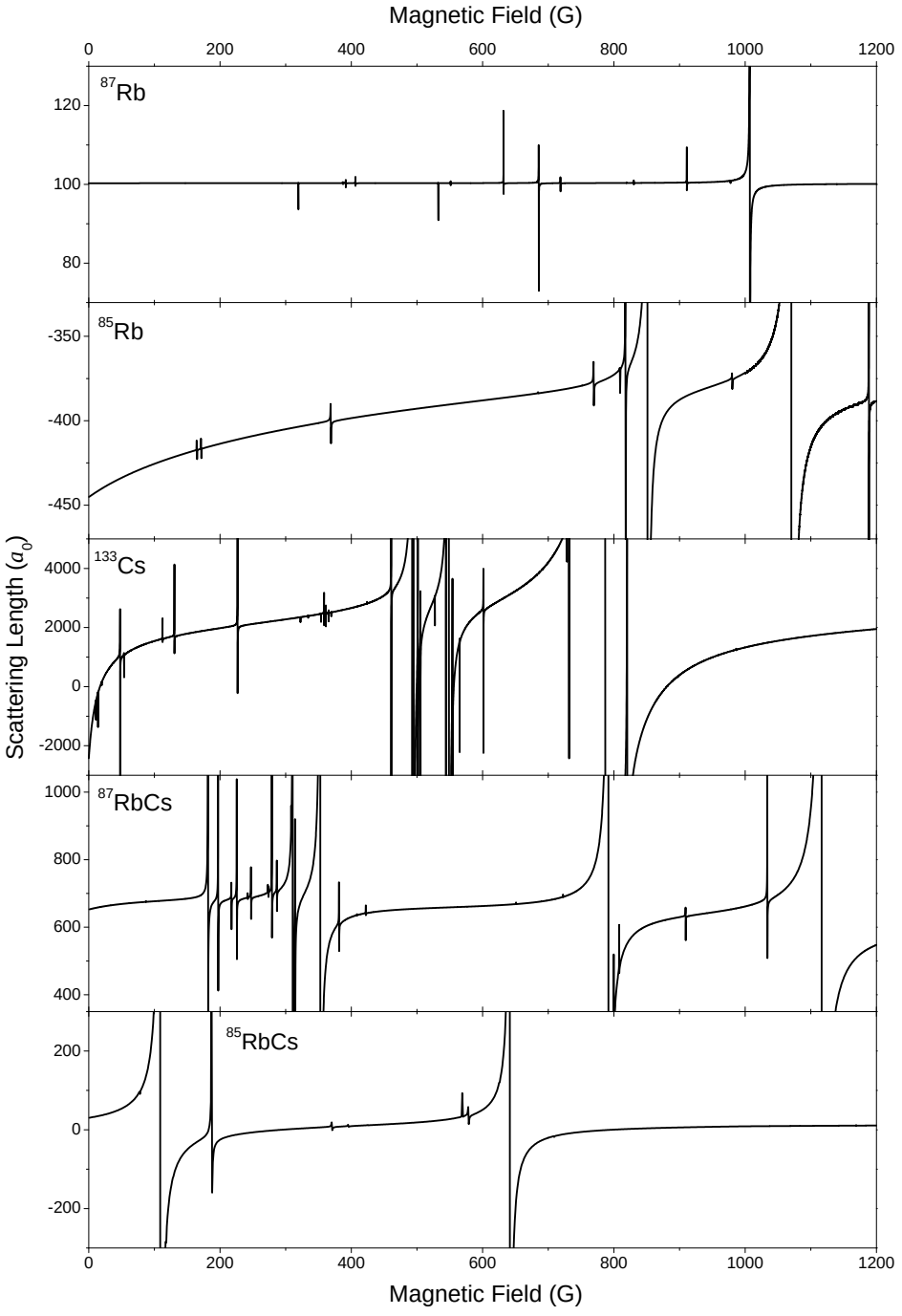

Figure 9.1: All intra- and interspecies scattering lengths relevant for the work presented in this thesis. The *s*-wave scattering lengths are given for collisions between the atoms in their individual absolute ground states.

previous work with ^{85}Rb has only focussed on a broad Feshbach resonance at 155 G in the $(2, -2)$ state.

We explored the scattering properties of ^{85}Rb in the $(2, -2)$ state to a magnetic field range up to 1000 G and expanded the investigation to the $(2, +2)$ absolute ground state in the same field range. Here, we have found numerous narrow and broad Feshbach resonances. A broad resonance in the $(2, +2)$ state offers the possibility to tune the scattering length to a positive value and offers the prospect of BEC formation in the absolute internal ground state. We have also detected one Feshbach resonance in a spin mixture of ^{85}Rb in the (2,+2) and (3,+3) states.

Before the production of dimers from ^{87}Rb and ^{133}Cs, we first tested the magnetoassociation ramp sequence with Cs_2. We used a Feshbach resonance at ~ 19.9 G to produce $2.1(1) \times 10^4$ molecules out of a sample of $3.28(2) \times 10^5$ Cs atoms with a PSD of 0.20(1). The molecules were separated from the atoms using the Stern-Gerlach technique. The molecules can be confined in the optical dipole trap, where we measured a lifetime of 0.88(8) s. Subsequently, we were able to control the molecular state using magnetic field ramps.

Molecules falling out of the trap experienced a decreasing magnetic bias field due to the magnetic field gradient. This led to 'bouncing' of the molecules around a bias field of 13.5 G at a gradient of 40 G/cm. Furthermore, the production of multiple molecular samples was possible due to the magnetic field gradient. A combination of both techniques led to the 'collision' of two molecular samples.

Following this, we used our experience gained from work on the Cs_2 dimers to produce up to ~ 5000 heteronuclear ^{87}RbCs molecules using a Feshbach resonance at 197.1 G and confined them in the optical dipole trap with a lifetime of 0.21(1) s. We measured the magnetic moment of the molecules in different states between 181 G and 185 G.

We built the experimental setup required for the STIRAP transfer. This is based on two diode lasers locked to an ultra-low-expansion cavity using the PDH technique. The wavelengths of the two STIRAP transitions is ~ 980 nm and ~ 1556 nm. Using this setup molecule loss spectroscopy on electronically excited states with mixed singlet and triplet character was performed and

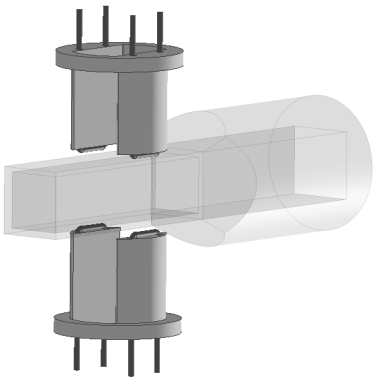

Figure 9.2: Electrodes to induce an electric dipole moment in the ^{87}RbCs molecules. The mounts are designed so they can be mounted into the existing magnetic coil mounts and no laser beams are blocked.

candidates for intermediate states for the STIRAP transfer were detected. The detection of the same transition several times over 5 months resulted in a drift relative to the closest cavity resonance of 800 kHz. This promises a good long-term stability for future STIRAP experiments. Two-photon spectroscopy on the rovibrational ground state was performed and resulted in a binding energy of this state of 3811.574(1) cm^{-1}.

9.2 Outlook

9.2.1 The ^{87}RbCs ground state

The electric dipole moment of the rovibrational ground state of the ^{87}RbCs molecule can be measured by detecting a shift in its energy due to the Stark effect. To induce a dipole moment, electrodes presented in figure 9.2 were designed. They are made from wire with a 2 mm diameter and run 22 mm parallel to the UHV glass cell. The mounts are designed so that existing beams are not blocked and such that they can be fixed in the magnetic coil mounts. The electrodes are driven with two SRS PS350 high voltage power supplies which can provide up to ±5 kV.

By applying ±4 kV to the electrodes, an electric field of 1 kV/cm at the position of the molecules can be produced. From the left panel of figure 9.3 we can read out that the induced dipole moment at this field is ~ 0.45 D.

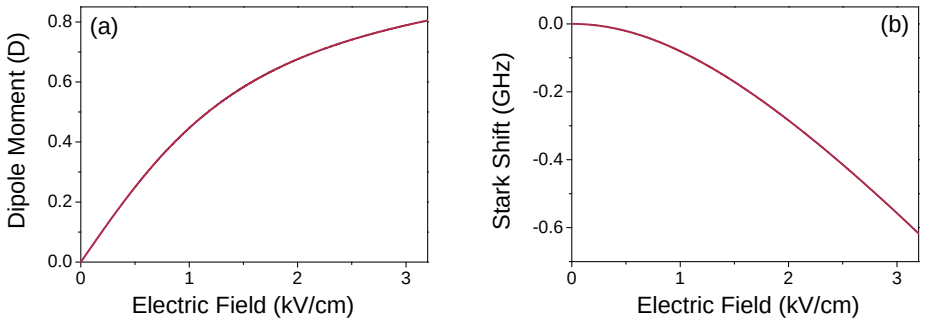

Figure 9.3: Electric dipole moment (a) and Stark shift (b) of the rovibrational ground state of ^{87}RbCs versus external electric field [216].

To determine the electric dipole moment experimentally, the Stark shift of the ground state will be measured [214]. The expected shift is presented in the right panel of figure 9.3. For an electric field of 1 kV/cm, a shift of 80 MHz is predicted. Subsequently, the molecules will be transferred into their rovibrational ground state using STIRAP.

9.2.2 ^{85}Rb BEC

Degeneracy of ^{85}Rb atoms has not been reached in this experiment due to a drop in evaporation efficiency at high PSD. At this stage, high background two-body and inelastic three-body collisions lead to trap loss. This effect has been observed previously in this system [188]. In another experiment within our group, a ^{85}Rb BEC has been created [186]. The main difference in this experiment is a larger trapping volume formed by dipole trap beams with a waist of 136 μm, leading to trapping frequencies by a factor of two lower than in our experiment. Additionally, the initial number is a factor of two larger in the other experiment.

To produce a ^{85}Rb BEC in our setup, a new optical dipole trap will be implemented. To create a trap with larger depth, a bow-tie design is chosen where the power is re-used. A 50 W IPG Photonics YLR-50-LP fibre laser with a wavelength of 1070 nm will be used. This laser provides more power compared to the one currently used and the polarisability of the atoms is

larger at 1070 nm than the 1550 nm of the current laser [151] . The polarisability at 1070 nm compared to 1550 nm is larger by a factor of two for Cs and a factor of 1.6 for Rb. Thus the trap will be 1.7 times deeper for Cs than for Rb. With this setup beam waists of $\sim 160\,\mu$m can be realised, capable of producing the same maximum trap depth as in the current setup. This should make the production of a ^{85}Rb BEC possible in the future.

So far, degeneracy in ^{85}Rb was only achieved in the $(2, -2)$ state. Our work has shown that a broad Feshbach resonance exists in the $(2, +2)$ state at 851 G, which offers the possibility to tune the scattering length to a positive value. This makes evaporative cooling without two-body loss possible and offers the prospect of BEC formation in the absolute internal ground state.

9.2.3 ^{85}RbCs molecules

During the course of this work, we studied the interactions between ^{85}Rb and Cs. Their small interspecies scattering length is promising for further experiments including the production of ultracold ^{85}RbCs molecules. However, the maximum PSD reached in the current setup is not high enough to perform magnetoassociation. We hope that a higher PSD mixture can be produced with the new optical dipole trap described in the previous section.

The ^{87}RbCs molecule production suffers from a small efficiency of $\sim 3\%$. The small interactions between ^{85}Rb and ^{133}Cs can make it possible to load both species into an optical lattice simultaneously. The efficiency of the magnetoassociation can be significantly increased by association from a Mott-insulator phase [217, 218], where one atom of each species occupies each lattice site [215]. We hope that using this technique, a larger sample of molecules can be produced than in the case of ^{87}RbCs.

9.2.4 Concluding Remarks

This work represents our part of the pursuit to find a good way to produce an ultracold sample of polar molecules. Many groups around the world are working on different techniques and molecules to achieve this goal. The combination of magnetoassociation and STIRAP transfer proved to be successful

in a mixture of K and Rb. But since different molecular samples can show very different behaviours when, for example, exposed to an electric field, it is important to investigate the properties of as many different molecules as possible. This project was planned as a ^{87}RbCs experiment and we are close to success with the production of a polar sample. However, it was also important that we did not just followed the initial plan but started working on the ^{85}Rb–Cs mixture as well. Interestingly, the interactions changed completely by changing the Rb isotope. This makes it possible to work on two different mixtures in this experiment with completely different behaviour, and maybe one of these mixtures will open the door to all the exciting experiments proposed for ultracold polar molecules.

Part I

Appendices

Appendix A

Molecular quantum numbers

The assignment of angular momenta for diatomic molecules consisting of the atoms a and b following [219] is

L Electronic orbital angular momentum; $\vec{L} = \vec{l_a} + \vec{l_b}$.

S Electronic spin angular momentum; $\vec{S} = \vec{s_a} + \vec{s_b}$.

J Total angular momentum; $\vec{J} = \vec{L} + \vec{S} + \vec{R}$.

N Total angular momentum excluding electron spin; $\vec{N} = \vec{J} - \vec{S}$.

R Rotational angular momentum of the nuclei; $\vec{R} = \vec{N} - \vec{L}$.

I Nuclear spin angular momentum.

The molecular states are described by the term symbol

$$^{2S+1}\Lambda^{(+/-)}_{\Omega,(g/u)}, \tag{A.1}$$

where Λ is the projection of $\vec{L}$ to the internuclear axis and $\Omega = \Lambda + \Sigma$ as Σ is the projection of $\vec{S}$ to the internuclear axis. The parity, described by g/u, takes the inversion symmetry of the wave function relative to the centre of charge of homonuclear molecules into account. The symmetry of the wave function along the internuclear axis is represented by $\pm$.

Due to the cylindrical symmetry along the internuclear axis, different couplings between the angular moments in a diatomic atom can arise which are

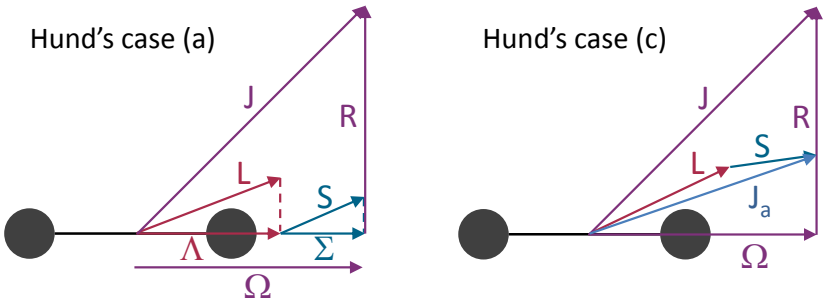

Figure A.1: Coupling of the angular momenta in diatomic molecules according to Hund's cases (a) and (c), relevant to describe the RbCs molecule.

described by Hund's coupling cases [220]. A total of five coupling cases exist. However, in real molecules, a superposition of the cases always emerges. Here, only the cases (a) and (c), relevant for the description of the RbCs molecule are described and visualised in figure A.1.

Hund's coupling case (a)

The orbital angular momentum $\vec{L}$ strongly couples to the internuclear axis by electrostatic forces. The electron spin angular momentum $\vec{S}$ is strongly coupled to $\vec{L}$ through spin-orbit coupling. The projections of $\vec{L}$ and $\vec{S}$ to the internuclear axis are Λ and Σ respectively and their sum is $\Omega = \Lambda + \Sigma$. The rotational angular momentum of the nuclei $\vec{R}$ is coupled to Ω and together they form the total angular momentum $\vec{J}$. The projections of $\vec{L}$ and $\vec{S}$ onto the internuclear axis can have the magnitudes $\pm\Lambda$ and $\pm\Sigma$ since the precession about the internuclear axis has two equal and opposite senses. This leads to two senses, $\pm\Omega$, of the projection of the electronic angular momentum. This leads to the Λ- and Ω-doubling. Good quantum numbers are $\Lambda, S, \Sigma, J, \Omega$.

Hund's coupling case (c)

In this case, the coupling between $\vec{L}$ and $\vec{S}$ is stronger than the interaction with the internuclear axis. Here, the projections Λ and Σ are not defined but $\vec{L}$ and $\vec{S}$ are coupled and form J_a. The projection of J_a to the internuclear axis is Ω which couples to the rotational momentum $\vec{R}$ and forms the total momentum $\vec{J}$. For $\Omega \neq 0$ degenerate states exist for a non-rotating molecule. This degeneracy, removed by rotation, is called Ω-doubling. Good quantum numbers are (J_a, Ω, J).

Bibliography

[1] A. L. Schawlow and C. H. Townes, *Infrared and Optical Masers*, Phys. Rev. **112**, 1940 (1958).

[2] T. H. Maiman, *Stimulated Optical Radiation in Ruby*, Nature **187**, 493 (1960).

[3] S. Andreev, V. I. Balykin, V. S. Letokhov, and V. G. Minogin, *Radiative slowing and reduction of the energy spread of a beam of sodium atoms to 1.5 K in an oppositely directed laser beam*, JETP Lett. **34**, 442 (1981).

[4] W. D. Phillips and H. Metcalf, *Laser Deceleration of an Atomic Beam*, Phys. Rev. Lett. **48**, 596 (1982).

[5] A. L. Migdall, J. V. Prodan, W. D. Phillips, T. H. Bergeman, and H. J. Metcalf, *First Observation of Magnetically Trapped Neutral Atoms*, Phys. Rev. Lett. **54**, 2596 (1985).

[6] C. Cohen-Tannoudji, *Atomic Motion in Laser Light, in Fundamental Systems in Quantum Optics* (Elsevier Science Publisher B.V., 1992).

[7] C. Cohen-Tannoudji and D. Guéry-Odelin, *Advances In Atomic Physics: An Overview* (World Scientific, 2011).

[8] H. J. Metcalf and P. van der Straten, *Laser Cooling and Trapping* (Springer, 2002).

[9] C. J. Foot, *Atomic Physics (Oxford Master Series in Atomic, Optical and Laser Physics)*, 1 ed. (Oxford University Press, USA, 2005).

[10] S. Chu, *Nobel Lecture: The manipulation of neutral particles*, Rev. Mod. Phys. **70**, 685 (1998).

[11] C. N. Cohen-Tannoudji, *Nobel Lecture: Manipulating atoms with photons*, Rev. Mod. Phys. **70**, 707 (1998).

[12] W. D. Phillips, *Nobel Lecture: Laser cooling and trapping of neutral atoms*, Rev. Mod. Phys. **70**, 721 (1998).

[13] N. Masuhara *et al.*, *Evaporative Cooling of Spin-Polarized Atomic Hydrogen*, Phys. Rev. Lett. **61**, 935 (1988).

[14] M. H. Anderson, J. R. Ensher, M. R. Matthews, C. E. Wieman, and E. A. Cornell, *Observation of Bose-Einstein Condensation in a Dilute Atomic Vapor*, Science **269**, 198 (1995).

[15] C. C. Bradley, C. A. Sackett, J. J. Tollett, and R. G. Hulet, *Evidence of Bose-Einstein Condensation in an Atomic Gas with Attractive Interactions*, Phys. Rev. Lett. **75**, 1687 (1995).

[16] K. B. Davis *et al.*, *Bose-Einstein Condensation in a Gas of Sodium Atoms*, Phys. Rev. Lett. **75**, 3969 (1995).

[17] F. Dalfovo, S. Giorgini, L. P. Pitaevskii, and S. Stringari, *Theory of Bose-Einstein condensation in trapped gases*, Rev. Mod. Phys. **71**, 463 (1999).

[18] E. A. Cornell and C. E. Wieman, *Nobel Lecture: Bose-Einstein condensation in a dilute gas, the first 70 years and some recent experiments*, Rev. Mod. Phys. **74**, 875 (2002).

[19] W. Ketterle, *Nobel lecture: When atoms behave as waves: Bose-Einstein condensation and the atom laser*, Rev. Mod. Phys. **74**, 1131 (2002).

[20] Bose, *Plancks Gesetz und Lichtquantenhypothese*, Zeitschrift für Physik **26**, 178 (1924).

[21] A. Einstein, *Quantentheorie des einatomigen idealen Gases. Zweite Abhandlung*, Sitzungber. Preuss. Akad. Wiss. **3**, 3 (1925).

[22] O. Morsch and M. Oberthaler, *Dynamics of Bose-Einstein condensates in optical lattices*, Rev. Mod. Phys. **78**, 179 (2006).

[23] I. Bloch, *Ultracold quantum gases in optical lattices*, Nat. Phys. **1**, 23 (2005).

[24] A. Micheli, G. K. Brennen, and P. Zoller, *A toolbox for lattice-spin models with polar molecules*, Nat. Phys. **2**, 341 (2006).

[25] R. Barnett, D. Petrov, M. Lukin, and E. Demler, *Quantum Magnetism with Multicomponent Dipolar Molecules in an Optical Lattice*, Phys. Rev. Lett. **96**, 190401 (2006).

[26] L. Pollet, J. D. Picon, H. P. Büchler, and M. Troyer, *Supersolid Phase with Cold Polar Molecules on a Triangular Lattice*, Phys. Rev. Lett. **104**, 125302 (2010).

[27] M. A. Baranov, M. Dalmonte, G. Pupillo, and P. Zoller, *Condensed Matter Theory of Dipolar Quantum Gases*, Chem. Rev. **112**, 5012 (2012).

[28] D. DeMille, *Quantum Computation with Trapped Polar Molecules*, Phys. Rev. Lett. **88**, 067901 (2002).

[29] A. André *et al.*, *A coherent all-electrical interface between polar molecules and mesoscopic superconducting resonators*, Nat. Phys. **2**, 636 (2006).

[30] V. V. Flambaum and M. G. Kozlov, *Enhanced Sensitivity to the Time Variation of the Fine-Structure Constant and m_p/m_e in Diatomic Molecules*, Phys. Rev. Lett. **99**, 150801 (2007).

[31] T. A. Isaev, S. Hoekstra, and R. Berger, *Laser-cooled RaF as a promising candidate to measure molecular parity violation*, Phys. Rev. A **82**, 052521 (2010).

[32] J. J. Hudson *et al.*, *Improved measurement of the shape of the electron*, Nature **473**, 493 (2011).

[33] E. R. Hudson *et al.*, *Production of cold formaldehyde molecules for study and control of chemical reaction dynamics with hydroxyl radicals*, Phys. Rev. A **73**, 063404 (2006).

[34] R. V. Krems, *Cold controlled chemistry*, Phys. Chem. Chem. Phys. **10**, 4079 (2008).

[35] T. F. Gallagher, *Rydberg Atoms (Cambridge Monographs on Atomic, Molecular and Chemical Physics)* (Cambridge University Press, 1994).

[36] T. Lahaye, C. Menotti, L. Santos, M. Lewenstein, and T. Pfau, *The physics of dipolar bosonic quantum gases*, Rep. Prog. Phys. **72**, 126401 (2009).

[37] E. S. Shuman, J. F. Barry, and D. DeMille, *Laser cooling of a diatomic molecule*, Nature **467**, 820 (2010).

[38] M. T. Hummon *et al.*, *2D Magneto-Optical Trapping of Diatomic Molecules*, Phys. Rev. Lett. **110**, 143001 (2013).

[39] V. Zhelyazkova *et al.*, *Laser cooling and slowing of CaF molecules*, arXiv:1308.0421 [physics.atom-ph], 2013.

[40] L. D. Carr, D. DeMille, R. V. Krems, and J. Ye, *Cold and ultracold molecules: science, technology and applications*, New J. Phys. **11**, 055049 (2009).

[41] J. D. Weinstein, R. deCarvalho, T. Guillet, B. Friedrich, and J. M. Doyle, *Magnetic trapping of calcium monohydride molecules at millikelvin temperatures*, Nature **395**, 148 (1998).

[42] N. R. Hutzler, H.-I. Lu, and J. M. Doyle, *The Buffer Gas Beam: An Intense, Cold, and Slow Source for Atoms and Molecules*, Chem. Rev. **112**, 4803 (2012).

[43] N. E. Bulleid *et al.*, *Characterization of a cryogenic beam source for atoms and molecules*, Phys. Chem. Chem. Phys. **15**, 12299 (2013).

[44] W. H. Wing, *Electrostatic Trapping of Neutral Atomic Particles*, Phys. Rev. Lett. **45**, 631 (1980).

[45] S. Tokunaga *et al.*, *Prospects for sympathetic cooling of molecules in electrostatic, ac and microwave traps*, Eur. Phys. J. D **65**, 141 (2011).

[46] M. Zeppenfeld *et al.*, *Sisyphus cooling of electrically trapped polyatomic molecules*, Nature **491**, 570 (2012).

[47] H. L. Bethlem, G. Berden, and G. Meijer, *Decelerating Neutral Dipolar Molecules*, Phys. Rev. Lett. **83**, 1558 (1999).

[48] J. R. Bochinski, E. R. Hudson, H. J. Lewandowski, G. Meijer, and J. Ye, *Phase Space Manipulation of Cold Free Radical OH Molecules*, Phys. Rev. Lett. **91**, 243001 (2003).

[49] S. Y. T. van de Meerakker, H. L. Bethlem, N. Vanhaecke, and G. Meijer, *Manipulation and Control of Molecular Beams*, Chem. Rev. **112**, 4828 (2012).

[50] E. Narevicius *et al.*, *Stopping Supersonic Beams with a Series of Pulsed Electromagnetic Coils: An Atomic Coilgun*, Phys. Rev. Lett. **100**, 093003 (2008).

[51] E. Lavert-Ofir *et al.*, *A moving magnetic trap decelerator: a new source of cold atoms and molecules*, New Journal of Physics **13**, 103030 (2011).

[52] A. Wiederkehr, H. Schmutz, M. Motsch, and F. Merkt, *Velocity-tunable slow beams of cold O_2 in a single spin-rovibronic state with full angular-momentum orientation by multistage Zeeman deceleration*, Molecular Physics **110**, 1807 (2012).

[53] E. Narevicius and M. G. Raizen, *Toward Cold Chemistry with Magnetically Decelerated Supersonic Beams*, Chem. Rev. **112**, 4879 (2012).

[54] R. Fulton, A. I. Bishop, M. N. Shneider, and P. F. Barker, *Controlling the motion of cold molecules with deep periodic optical potentials*, Nat. Phys. **2**, 465 (2006).

[55] M. Gupta and D. Herschbach, *Slowing and Speeding Molecular Beams by Means of a Rapidly Rotating Source*, J. Phys. Chem. A **105**, 1626 (2001).

[56] S. Chervenkov *et al.*, *Continuous Centrifuge Decelerator for Polar Molecules*, Phys. Rev. Lett. **112**, 013001 (2014).

[57] W. G. Doherty *et al.*, *Production of cold bromine atoms at zero mean velocity by photodissociation*, Phys. Chem. Chem. Phys. **13**, 8441 (2011).

[58] K. M. Jones, E. Tiesinga, P. D. Lett, and P. S. Julienne, *Ultracold photoassociation spectroscopy: Long-range molecules and atomic scattering*, Rev. Mod. Phys. **78**, 483 (2006).

[59] C. Chin, R. Grimm, P. Julienne, and E. Tiesinga, *Feshbach resonances in ultracold gases*, Rev. Mod. Phys. **82**, 1225 (2010).

[60] E. Tiemann, *Cold Molecules, in Cold Atoms and Molecules* (Wiley-VCH Verlag GmbH & Co. KGaA, Weinheim, 2009).

[61] A. Fioretti *et al.*, *Formation of Cold Cs_2 Molecules through Photoassociation*, Phys. Rev. Lett. **80**, 4402 (1998).

[62] A. J. Kerman, J. M. Sage, S. Sainis, T. Bergeman, and D. DeMille, *Production and State-Selective Detection of Ultracold RbCs Molecules*, Phys. Rev. Lett. **92**, 153001 (2004).

[63] J. M. Sage, S. Sainis, T. Bergeman, and D. DeMille, *Optical Production of Ultracold Polar Molecules*, Phys. Rev. Lett. **94**, 203001 (2005).

[64] J. Deiglmayr *et al.*, *Formation of Ultracold Polar Molecules in the Rovibrational Ground State*, Phys. Rev. Lett. **101**, 133004 (2008).

[65] K. Aikawa *et al.*, *Toward the production of quantum degenerate bosonic polar molecules, $^{41}K^{87}Rb$*, New Journal of Physics **11**, 055035 (2009).

[66] K. Bergmann, H. Theuer, and B. W. Shore, *Coherent population transfer among quantum states of atoms and molecules*, Rev. Mod. Phys. **70**, 1003 (1998).

[67] K. Aikawa *et al.*, *Coherent Transfer of Photoassociated Molecules into the Rovibrational Ground State*, Phys. Rev. Lett. **105**, 203001 (2010).

[68] P. Courteille, R. S. Freeland, D. J. Heinzen, F. A. van Abeelen, and B. J. Verhaar, *Observation of a Feshbach Resonance in Cold Atom Scattering*, Phys. Rev. Lett. **81**, 69 (1998).

[69] S. Inouye *et al.*, *Observation of Feshbach resonances in a Bose-Einstein condensate*, Nature **392**, 151 (1998).

[70] S. Inouye *et al.*, *Observation of Heteronuclear Feshbach Resonances in a Mixture of Bosons and Fermions*, Phys. Rev. Lett. **93**, 183201 (2004).

[71] C. A. Stan, M. W. Zwierlein, C. H. Schunck, S. M. F. Raupach, and W. Ketterle, *Observation of Feshbach Resonances between Two Different Atomic Species*, Phys. Rev. Lett. **93**, 143001 (2004).

[72] G. Quéméner and P. S. Julienne, *Ultracold Molecules under Control!*, Chem. Rev. **112**, 4949 (2012).

[73] J. Herbig *et al.*, *Preparation of a Pure Molecular Quantum Gas*, Science **301**, 1510 (2003).

[74] S. Dürr, T. Volz, A. Marte, and G. Rempe, *Observation of Molecules Produced from a Bose-Einstein Condensate*, Phys. Rev. Lett. **92**, 020406 (2004).

[75] K. Xu *et al.*, *Formation of Quantum-Degenerate Sodium Molecules*, Phys. Rev. Lett. **91**, 210402 (2003).

[76] C. A. Regal, C. Ticknor, J. L. Bohn, and D. S. Jin, *Creation of ultracold molecules from a Fermi gas of atoms*, Nature **424**, 47 (2003).

[77] K. E. Strecker, G. B. Partridge, and R. G. Hulet, *Conversion of an Atomic Fermi Gas to a Long-Lived Molecular Bose Gas*, Phys. Rev. Lett. **91**, 080406 (2003).

[78] J. Cubizolles, T. Bourdel, S. J. J. M. F. Kokkelmans, G. V. Shlyapnikov, and C. Salomon, *Production of Long-Lived Ultracold Li_2 Molecules from a Fermi Gas*, Phys. Rev. Lett. **91**, 240401 (2003).

[79] S. Jochim *et al.*, *Pure Gas of Optically Trapped Molecules Created from Fermionic Atoms*, Phys. Rev. Lett. **91**, 240402 (2003).

[80] C. Ospelkaus *et al.*, *Ultracold Heteronuclear Molecules in a 3D Optical Lattice*, Phys. Rev. Lett. **97**, 120402 (2006).

[81] A.-C. Voigt *et al.*, *Ultracold Heteronuclear Fermi-Fermi Molecules*, Phys. Rev. Lett. **102**, 020405 (2009).

[82] F. M. Spiegelhalder *et al.*, *All-optical production of a degenerate mixture of* ^{6}*Li and* ^{40}*K and creation of heteronuclear molecules*, Phys. Rev. A **81**, 043637 (2010).

[83] T. Takekoshi *et al.*, *Towards the production of ultracold ground-state RbCs molecules: Feshbach resonances, weakly bound states, and the coupled-channel model*, Phys. Rev. A **85**, 032506 (2012).

[84] C.-H. Wu, J. W. Park, P. Ahmadi, S. Will, and M. W. Zwierlein, *Ultracold Fermionic Feshbach Molecules of* ^{23}Na^{40}K, Phys. Rev. Lett. **109**, 085301 (2012).

[85] M.-S. Heo *et al.*, *Formation of ultracold fermionic NaLi Feshbach molecules*, Phys. Rev. A **86**, 021602 (2012).

[86] S. Jochim *et al.*, *Bose-Einstein Condensation of Molecules*, Science **302**, 2101 (2003).

[87] M. Greiner, C. A. Regal, and D. S. Jin, *Emergence of a molecular Bose-Einstein condensate from a Fermi gas*, Nature **426**, 537 (2003).

[88] M. W. Zwierlein *et al.*, *Observation of Bose-Einstein Condensation of Molecules*, Phys. Rev. Lett. **91**, 250401 (2003).

[89] S. Kotochigova and E. Tiesinga, *Ab initio relativistic calculation of the RbCs molecule*, J. Chem. Phys. **123**, (2005).

[90] F. Lang, K. Winkler, C. Strauss, R. Grimm, and J. H. Denschlag, *Ultracold Triplet Molecules in the Rovibrational Ground State*, Phys. Rev. Lett. **101**, 133005 (2008).

[91] J. G. Danzl *et al.*, *Quantum Gas of Deeply Bound Ground State Molecules*, Science **321**, 1062 (2008).

[92] K.-K. Ni *et al.*, *A High Phase-Space-Density Gas of Polar Molecules*, Science **322**, 231 (2008).

[93] B. Yan *et al.*, *Observation of dipolar spin-exchange interactions with lattice-confined polar molecules*, Nature **501**, 521 (2013).

[94] M. Debatin *et al.*, *Molecular spectroscopy for ground-state transfer of ultracold RbCs molecules*, Phys. Chem. Chem. Phys. **13**, 18926 (2011).

[95] J. W. Park *et al.*, *Quantum degenerate Bose-Fermi mixture of chemically different atomic species with widely tunable interactions*, Phys. Rev. A **85**, 051602 (2012).

[96] B. Deh *et al.*, *Giant Feshbach resonances in* ^{6}Li-^{85}Rb *mixtures*, Phys. Rev. A **82**, 020701 (2010).

[97] H. Hara, Y. Takasu, Y. Yamaoka, J. M. Doyle, and Y. Takahashi, *Quantum Degenerate Mixtures of Alkali and Alkaline-Earth-Like Atoms*, Phys. Rev. Lett. **106**, 205304 (2011).

[98] V. V. Ivanov *et al.*, *Sympathetic Cooling in an Optically Trapped Mixture of Alkali and Spin-Singlet Atoms*, Phys. Rev. Lett. **106**, 153201 (2011).

[99] F. Münchow, C. Bruni, M. Madalinski, and A. Görlitz, *Two-photon photoassociation spectroscopy of heteronuclear YbRb*, Phys. Chem. Chem. Phys. **13**, 18734 (2011).

[100] M. Baranov, *Theoretical progress in many-body physics with ultracold dipolar gases*, Physics Reports **464**, 71 (2008).

[101] S. Kotochigova, P. S. Julienne, and E. Tiesinga, *Ab initio calculation of the KRb dipole moments*, Phys. Rev. A **68**, 022501 (2003).

[102] P. S. Żuchowski and J. M. Hutson, *Reactions of ultracold alkali-metal dimers*, Phys. Rev. A **81**, 060703 (2010).

[103] C. Fellows, R. Gutterres, A. Campos, J. Vergès, and C. Amiot, *The RbCs $X^1\Sigma^+$ Ground Electronic State :New Spectroscopic Study*, J. Mol. Spect. **197**, 19 (1999).

[104] A. Griesmaier, J. Werner, S. Hensler, J. Stuhler, and T. Pfau, *Bose-Einstein Condensation of Chromium*, Phys. Rev. Lett. **94**, 160401 (2005).

[105] M. Lu, N. Q. Burdick, S. H. Youn, and B. L. Lev, *Strongly Dipolar Bose-Einstein Condensate of Dysprosium*, Phys. Rev. Lett. **107**, 190401 (2011).

[106] K. Aikawa *et al.*, *Bose-Einstein Condensation of Erbium*, Phys. Rev. Lett. **108**, 210401 (2012).

[107] J. Deiglmayr, M. Aymar, R. Wester, M. Weidemüller, and O. Dulieu, *Calculations of static dipole polarizabilities of alkali dimers: Prospects for alignment of ultracold molecules*, J. Chem. Phys. **129**, 064309 (2008).

[108] C. J. Joachain, *Quantum Collision Theory* (North-Holland, The Netherlands, 1983).

[109] C. Strauss *et al.*, *Hyperfine, rotational, and vibrational structure of the* $a^3\Sigma_u^+$ state of $^{87}Rb_2$, Phys. Rev. A **82**, 052514 (2010).

[110] M. Berninger *et al.*, *Feshbach resonances, weakly bound molecular states, and coupled-channel potentials for cesium at high magnetic fields*, Phys. Rev. A **87**, 032517 (2013).

[111] J. Dalibard, *Collisional dynamics of ultra-cold atomic gases*, Proceedings of the International School of Physics - Enrico Fermi, Varenna, Course CXL , 1 (1999).

[112] D. A. Brue and J. M. Hutson, *Prospects of forming ultracold molecules in* $^2\Sigma$ *states by magnetoassociation of alkali-metal atoms with Yb*, Phys. Rev. A **87**, 052709 (2013).

[113] A. J. Moerdijk, B. J. Verhaar, and A. Axelsson, *Resonances in ultracold collisions of* ^6Li, ^7Li, *and* ^{23}Na, Phys. Rev. A **51**, 4852 (1995).

[114] E. A. Donley *et al.*, *Dynamics of collapsing and exploding Bose-Einstein condensates*, Nature **412**, 295 (2001).

[115] E. Timmermans, P. Tommasini, M. Hussein, and A. Kerman, *Feshbach resonances in atomic Bose-Einstein condensates*, Physics Reports **315**, 199 (1999).

[116] M. Mark *et al.*, *Spectroscopy of ultracold trapped cesium Feshbach molecules*, Phys. Rev. A **76**, 042514 (2007).

[117] B. Gao, *Binding energy and scattering length for diatomic systems*, J. Phys. B **37**, 4273 (2004).

[118] H. T. C. Stoof, J. M. V. A. Koelman, and B. J. Verhaar, *Spin-exchange and dipole relaxation rates in atomic hydrogen: Rigorous and simplified calculations*, Phys. Rev. B **38**, 4688 (1988).

[119] J. M. Hutson and S. S. Greene, MOLSCAT computer program, version 14 , distributed by Collaborative Computational Project No. 6 of the EPSRC (1994).

[120] M. L. González-Martínez and J. M. Hutson, *Ultracold atom-molecule collisions and bound states in magnetic fields: Tuning zero-energy Feshbach resonances in He-NH* ($^3\Sigma^-$), Phys. Rev. A **75**, 022702 (2007).

[121] J. M. Hutson, BOUND computer program, version 5 , distributed by Collaborative Computational Project No. 6 of the EPSRC (1993).

[122] J. M. Hutson, *FIELD computer program, version 1*, 2011.

[123] C. L. Blackley *et al.*, *Feshbach resonances in ultracold* ^{85}Rb, Phys. Rev. A **87**, 033611 (2013).

[124] O. Docenko, M. Tamanis, R. Ferber, H. Knöckel, and E. Tiemann, *Singlet and triplet potentials of the ground-state atom pair Rb + Cs studied by Fourier-transform spectroscopy*, Phys. Rev. A **83**, 052519 (2011).

[125] C. Chin *et al.*, *Precision Feshbach spectroscopy of ultracold* Cs_2, Phys. Rev. A **70**, 032701 (2004).

[126] K. Pilch *et al.*, *Observation of interspecies Feshbach resonances in an ultracold Rb-Cs mixture*, Phys. Rev. A **79**, 042718 (2009).

[127] H.-W. Cho *et al.*, *Feshbach spectroscopy of an ultracold mixture of* ^{85}*Rb and* ^{133}*Cs*, Phys. Rev. A **87**, 010703 (2013).

[128] J. R. Kuklinski, U. Gaubatz, F. T. Hioe, and K. Bergmann, *Adiabatic population transfer in a three-level system driven by delayed laser pulses*, Phys. Rev. A **40**, 6741 (1989).

[129] M. P. Fewell, B. W. Shore, and K. Bergmann, *Coherent Population Transfer among Three States: Full Algebraic Solutions and the Relevance of Non Adiabatic Processes to Transfer by Delayed Pulses*, Aust. J. Phys. **50**, 281 (1997).

[130] L. P. Yatsenko, V. I. Romanenko, B. W. Shore, and K. Bergmann, *Stimulated Raman adiabatic passage with partially coherent laser fields*, Phys. Rev. A **65**, 043409 (2002).

[131] T. Bergeman, C. E. Fellows, R. F. Gutterres, and C. Amiot, *Analysis of strongly coupled electronic states in diatomic molecules: Low-lying excited states of RbCs*, Phys. Rev. A **67**, 050501 (2003).

[132] W. Stwalley, *Efficient conversion of ultracold Feshbach-resonance-related polar molecules into ultracold ground state* ($X^1\Sigma^+ \mathsf{v} = 0, \mathsf{J} = 0$) *molecules*, Eur. Phys. J. D **31**, 221 (2004).

[133] O. Docenko *et al.*, *Spectroscopic data, spin-orbit functions, and revised analysis of strong perturbative interactions for the* $A\,^1\Sigma^+$ *and* $b\,^3\Pi$ *states of RbCs*, Phys. Rev. A **81**, 042511 (2010).

[134] M. Debatin, *Creation of Ultracold RbCs Ground-State Molecules*, PhD thesis, University of Innsbruck, 2013.

[135] D. J. McCarron, *A Quantum Degenerate Mixture of* ^{87}*Rb and* ^{133}*Cs*, PhD thesis, Durham University, UK, 2011.

[136] D. L. Jenkin, *Feshbach spectroscopy of an ultracold Rb-Cs mixture*, PhD thesis, Durham University, UK, 2012.

[137] C. Adams and E. Riis, *Laser cooling and trapping of neutral atoms*, Prog. Quant. Electr. **21**, 1 (1997).

[138] J. Arlt, O. Maragò, S. Webster, S. Hopkins, and C. Foot, *A pyramidal magneto-optical trap as a source of slow atoms*, Opt. Commun. **157**, 303 (1998).

[139] N. Lundblad *et al.*, *Two-species cold atomic beam*, J. Opt. Soc. Am. B **21**, 3 (2004).

[140] W. Petrich, M. H. Anderson, J. R. Ensher, and E. A. Cornell, *Behavior of atoms in a compressed magneto-optical trap*, J. Opt. Soc. Am. B **11**, 1332 (1994).

[141] S. Chu, L. Hollberg, J. E. Bjorkholm, A. Cable, and A. Ashkin, *Three-dimensional viscous confinement and cooling of atoms by resonance radiation pressure*, Phys. Rev. Lett. **55**, 48 (1985).

[142] E. Majorana, *Atomi orientati in campo magnetico variabile*, Il Nuovo Cimento **9**, 43 (1932).

[143] M. D. Barrett, J. A. Sauer, and M. S. Chapman, *All-Optical Formation of an Atomic Bose-Einstein Condensate*, Phys. Rev. Lett. **87**, 010404 (2001).

[144] R. K. Raj, D. Bloch, J. J. Snyder, G. Camy, and M. Ducloy, *High-Frequency Optically Heterodyned Saturation Spectroscopy Via Resonant Degenerate Four-Wave Mixing*, Phys. Rev. Lett. **44**, 1251 (1980).

[145] J. H. Shirley, *Modulation transfer processes in optical heterodyne saturation spectroscopy*, Opt. Lett. **7**, 537 (1982).

[146] D. J. McCarron, S. A. King, and S. L. Cornish, *Modulation transfer spectroscopy in atomic rubidium*, Meas. Sci. Technol. **19**, 105601 (2008).

[147] G. C. Bjorklund, *Frequency-modulation spectroscopy: a new method for measuring weak absorptions and dispersions*, Opt. Lett. **5**, 15 (1980).

[148] M. Gehrtz, G. C. Bjorklund, and E. A. Whittaker, *Quantum-limited laser frequency-modulation spectroscopy*, J. Opt. Soc. Am. B **2**, 1510 (1985).

[149] B. Chéron, H. Gilles, J. Hamel, O. Moreau, and H. Sorel, *Laser frequency stabilization using Zeeman effect*, J. Phys. III France **4**, 401 (1994).

[150] K. L. Corwin, Z.-T. Lu, C. F. Hand, R. J. Epstein, and C. E. Wieman, *Frequency-Stabilized Diode Laser with the Zeeman Shift in an Atomic Vapor*, Appl. Opt. **37**, 3295 (1998).

[151] M. S. Safronova, B. Arora, and C. W. Clark, *Frequency-dependent polarizabilities of alkali-metal atoms from ultraviolet through infrared spectral regions*, Phys. Rev. A **73**, 022505 (2006).

[152] D. M. Stamper-Kurn *et al.*, *Optical Confinement of a Bose-Einstein Condensate*, Phys. Rev. Lett. **80**, 2027 (1998).

[153] D. Guéry-Odelin, J. Söding, P. Desbiolles, and J. Dalibard, *Is Bose-Einstein condensation of atomic cesium possible?*, Europhys. Lett. **44**, 25 (1998).

[154] A. M. Thomas, S. Hopkins, S. L. Cornish, and C. J. Foot, *Strong evaporative cooling towards Bose-Einstein condensation of a magnetically trapped caesium gas*, J. Opt. B: Quantum Semiclass. Opt. **5**, S107 (2003).

[155] C. S. Adams, H. J. Lee, N. Davidson, M. Kasevich, and S. Chu, *Evaporative Cooling in a Crossed Dipole Trap*, Phys. Rev. Lett. **74**, 3577 (1995).

[156] T. Kraemer *et al.*, *Optimized production of a cesium Bose-Einstein condensate*, Appl. Phys. B **79**, 1013 (2004).

[157] Y.-J. Lin, A. R. Perry, R. L. Compton, I. B. Spielman, and J. V. Porto, *Rapid production of ^{87}Rb Bose-Einstein condensates in a combined magnetic and optical potential*, Phys. Rev. A **79**, 063631 (2009).

[158] A. Lercher *et al.*, *Production of a dual-species Bose-Einstein condensate of Rb and Cs atoms*, Eur. Phys. J. D **65**, 3 (2011).

[159] H. Cho, D. McCarron, D. Jenkin, M. Köppinger, and S. Cornish, *A high phase-space density mixture of ^{87}Rb and ^{133}Cs: towards ultracold heteronuclear molecules*, Eur. Phys. J. D **65**, 125 (2011).

[160] D. J. McCarron, H. W. Cho, D. L. Jenkin, M. P. Köppinger, and S. L. Cornish, *Dual-species Bose-Einstein condensate of ^{87}Rb and ^{133}Cs*, Phys. Rev. A **84**, 011603 (2011).

[161] G. Breit and I. I. Rabi, *Measurement of Nuclear Spin*, Phys. Rev. **38**, 2082 (1931).

[162] K. Aikawa *et al.*, *Predicting and verifying transition strengths from weakly bound molecules*, Phys. Rev. A **83**, 042706 (2011).

[163] G. Brooker, *Modern Classical Optics (Oxford Master Series in Atomic, Optical and Laser Physics)* (Oxford University Press, USA, 2003).

[164] E. Hecht, *Optics* (Addison-Wesley, 2002).

[165] W. T. Silfvast, *Laser Fundamentals* (Cambridge University Press, USA, 2004).

[166] G. Machavariani, N. Davidson, A. Ishaaya, and A. Friesem, *Improving the stability of longitudinal and transverse laser modes*, Opt. Commun. **239**, 147 (2004).

[167] M. J. Lawrence, B. Willke, M. E. Husman, E. K. Gustafson, and R. L. Byer, *Dynamic response of a Fabry–Perot interferometer*, J. Opt. Soc. Am. B **16**, 523 (1999).

[168] R. W. Fox, *Temperature analysis of low-expansion Fabry-Perot cavities*, Opt. Express **17**, 15023 (2009).

[169] T. Legero, T. Kessler, and U. Sterr, *Tuning the thermal expansion properties of optical reference cavities with fused silica mirrors*, J. Opt. Soc. Am. B **27**, 914 (2010).

[170] H. S. Moon, W. K. Lee, L. Lee, and J. B. Kim, *Double resonance optical pumping spectrum and its application for frequency stabilization of a laser diode*, Appl. Phys. Lett. **85**, 3965 (2004).

[171] R. Drever *et al.*, *Laser phase and frequency stabilization using an optical resonator*, Appl. Phys. B **31**, 97 (1983).

[172] E. D. Black, *An introduction to Pound-Drever-Hall laser frequency stabilization*, Am. J. Phys. **69**, 79 (2001).

[173] F. Bondu, P. Fritschel, C. N. Man, and A. Brillet, *Ultrahigh-spectral-purity laser for the VIRGO experiment*, Opt. Lett. **21**, 582 (1996).

[174] J. Ye and J. L. Hall, *Optical phase locking in the microradian domain: potential applications to NASA spaceborne optical measurements*, Opt. Lett. **24**, 1838 (1999).

[175] J. I. Thorpe, K. Numata, and J. Livas, *Laser frequency stabilization and control through offset sidebandlocking to optical cavities*, Opt. Express **16**, 15980 (2008).

[176] K. Aikawa, *All-optical selective formation of ultracold molecules in the rovibrational ground state*, PhD thesis, University of Tokyo, 2011.

[177] T. Okoshi, K. Kikuchi, and A. Nakayama, *Novel method for high resolution measurement of laser output spectrum*, Electron. Lett. **16**, 630 (1980).

[178] H. Tsuchida, *Simple technique for improving the resolution of the delayed self-heterodyne method*, Opt. Lett. **15**, 640 (1990).

[179] R. W. Fox, C. W. Oates, and L. W. Hollberg, *1. Stabilizing diode lasers to high-finesse cavities*, in *Cavity-Enhanced Spectroscopies*, edited by R. D. van Zee and J. P. Looney, volume 40 of *Experimental Methods in the Physical Sciences*, pp. 1 – 46, Academic Press, 2003.

[180] C. L. Blackley, (private communication) .

[181] E. Wille *et al.*, *Exploring an Ultracold Fermi-Fermi Mixture: Interspecies Feshbach Resonances and Scattering Properties of* ^{6}Li *and* ^{40}K, Phys. Rev. Lett. **100**, 053201 (2008).

[182] J. L. Roberts, N. R. Claussen, S. L. Cornish, and C. E. Wieman, *Magnetic Field Dependence of Ultracold Inelastic Collisions near a Feshbach Resonance*, Phys. Rev. Lett. **85**, 728 (2000).

[183] A. Marte *et al.*, *Feshbach Resonances in Rubidium 87: Precision Measurement and Analysis*, Phys. Rev. Lett. **89**, 283202 (2002).

[184] S.-K. Tung, K. Jimenez-Garcia, J. Johansen, C. V. Parker, and C. Chin, *Observation of geometric scaling of Efmov states in a Fermi-Bose Li-Cs mixture*, arXiv , 1402.5943 (2014).

[185] E. Hodby *et al.*, *Production Efficiency of Ultracold Feshbach Molecules in Bosonic and Fermionic Systems*, Phys. Rev. Lett. **94**, 120402 (2005).

[186] A. L. Marchant, S. Händel, S. A. Hopkins, T. P. Wiles, and S. L. Cornish, *Bose-Einstein condensation of ^{85}Rb by direct evaporation in an optical dipole trap*, Phys. Rev. A **85**, 053647 (2012).

[187] J. M. Vogels *et al.*, *Prediction of Feshbach resonances in collisions of ultracold rubidium atoms*, Phys. Rev. A **56**, R1067 (1997).

[188] S. L. Cornish, N. R. Claussen, J. L. Roberts, E. A. Cornell, and C. E. Wieman, *Stable ^{85}Rb Bose-Einstein Condensates with Widely Tunable Interactions*, Phys. Rev. Lett. **85**, 1795 (2000).

[189] P. A. Altin *et al.*, *^{85}Rb tunable-interaction Bose-Einstein condensate machine*, Rev. Sci. Instrum. **81**, (2010).

[190] J. L. Roberts *et al.*, *Controlled Collapse of a Bose-Einstein Condensate*, Phys. Rev. Lett. **86**, 4211 (2001).

[191] P. A. Altin *et al.*, *Collapse and three-body loss in a ^{85}Rb Bose-Einstein condensate*, Phys. Rev. A **84**, 033632 (2011).

[192] S. L. Cornish, S. T. Thompson, and C. E. Wieman, *Formation of Bright Matter-Wave Solitons during the Collapse of Attractive Bose-Einstein Condensates*, Phys. Rev. Lett. **96**, 170401 (2006).

[193] R. J. Wild, P. Makotyn, J. M. Pino, E. A. Cornell, and D. S. Jin, *Measurements of Tan's Contact in an Atomic Bose-Einstein Condensate*, Phys. Rev. Lett. **108**, 145305 (2012).

[194] J. M. Hutson, *Feshbach resonances in ultracold atomic and molecular collisions: threshold behaviour and suppression of poles in scattering lengths*, New J. Phys. **9**, 152 (2007).

[195] Y. Wang and P. S. Julienne, (private communication) .

[196] N. R. Claussen *et al.*, *Very-high-precision bound-state spectroscopy near a ^{85}Rb Feshbach resonance*, Phys. Rev. A **67**, 060701 (2003).

[197] P. A. Altin *et al.*, *Measurement of inelastic losses in a sample of ultracold ^{85}Rb*, Phys. Rev. A **81**, 012713 (2010).

[198] M. Mark *et al.*, *Efficient creation of molecules from a cesium Bose-Einstein condensate*, Europhys. Lett. **69**, 706 (2005).

[199] M. Mark *et al.*, *"Stückelberg Interferometry" with Ultracold Molecules*, Phys. Rev. Lett. **99**, 113201 (2007).

[200] A. D. Lange *et al.*, *Determination of atomic scattering lengths from measurements of molecular binding energies near Feshbach resonances*, Phys. Rev. A **79**, 013622 (2009).

[201] S. Knoop *et al.*, *Metastable Feshbach Molecules in High Rotational States*, Phys. Rev. Lett. **100**, 083002 (2008).

[202] C. Chin *et al.*, *Observation of Feshbach-Like Resonances in Collisions between Ultracold Molecules*, Phys. Rev. Lett. **94**, 123201 (2005).

[203] F. Ferlaino *et al.*, *Collisions between Tunable Halo Dimers: Exploring an Elementary Four-Body Process with Identical Bosons*, Phys. Rev. Lett. **101**, 023201 (2008).

[204] F. Ferlaino *et al.*, *Collisions of ultracold trapped cesium Feshbach molecules*, Laser Physics **20**, 23 (2010).

[205] S. Knoop *et al.*, *Magnetically Controlled Exchange Process in an Ultracold Atom-Dimer Mixture*, Phys. Rev. Lett. **104**, 053201 (2010).

[206] J. M. Hutson, (private communication) .

[207] D. Jenkin *et al.*, *Bose-Einstein condensation of ^{87}Rb in a levitated crossed dipole trap*, Eur. Phys. J. D **65**, 11 (2011).

[208] C.-L. Hung, X. Zhang, N. Gemelke, and C. Chin, *Accelerating evaporative cooling of atoms into Bose-Einstein condensation in optical traps*, Phys. Rev. A **78**, 011604 (2008).

[209] M. R. Andrews *et al.*, *Observation of Interference Between Two Bose Condensates*, Science **275**, 637 (1997).

[210] M. P. Köppinger *et al.*, *Production of optically trapped $^{87}RbCs$ Feshbach molecules*, Phys. Rev. A **89**, 033604 (2014).

[211] R. W. Pattinson *et al.*, *Equilibrium solutions for immiscible two-species Bose-Einstein condensates in perturbed harmonic traps*, Phys. Rev. A **87**, 013625 (2013).

[212] C. H. Townes and A. L. Schawlow, *Microwave Spectroscopy* (McGraw-Hill, New York, 1955).

[213] M. Mark *et al.*, *Dark resonances for ground-state transfer of molecular quantum gases*, Appl. Phys. B **95**, 219 (2009).

[214] K.-K. Ni, S. Ospelkaus, D. J. Nesbitt, J. Ye, and D. S. Jin, *A dipolar gas of ultracold molecules*, Phys. Chem. Chem. Phys. **11**, 9626 (2009).

[215] J. G. Danzl *et al.*, *An ultracold high-density sample of rovibronic ground-state molecules in an optical lattice*, Nat. Phys. **6**, 265 (2010).

[216] K.-K. Ni, *A Quantum Gas Of Polar Molecules*, PhD thesis, University of Colorado, USA, 2009.

[217] B. Damski *et al.*, *Creation of a Dipolar Superfluid in Optical Lattices*, Phys. Rev. Lett. **90**, 110401 (2003).

[218] T. Volz *et al.*, *Preparation of a quantum state with one molecule at each site of an optical lattice*, Nat. Phys. **2**, 692 (2006).

[219] J. Brown and A. Carrington, *Rotational Spectroscopy of Diatomic Molecules* (Cambridge University Press, 2003).

[220] F. Hund, *Allgemeine Quantenmechanik des Atom- und Molekelbaues*, in *Quantentheorie*, edited by H. Bethe *et al.*, Handbuch der Physik, pp. 561–694, Springer Berlin Heidelberg, 1933.